

Time Resolved Vibrational Spectroscopies as a Tool for Exploring Dynamics of
Confined Systems

A THESIS

SUBMITTED TO THE FACULTY OF THE
UNIVERSITY OF MINNESOTA

BY

Cynthia G. Pyles

IN PARTIAL FULFILLMENT OF THE REQUIREMENTS
FOR THE DEGREE OF
DOCTOR OF PHILOSOPHY

Aaron M. Massari, Adviser

January, 2022

© Cynthia G. Pyles 2022

ALL RIGHTS RESERVED

Acknowledgements

Aaron, I will be forever grateful that you let me volunteer in your lab during my gap year between undergraduate and graduate school. I came to lab with limited confidence in my scientific abilities. My experiences with you and Courtney during my gap year, and then graduate school, slowly built my resolution to succeed. During recruiting weekends, I often told prospective students “I would go to bat for my adviser. I want to make him famous someday.” To this very day it feels like I won the PI lottery and it brings me overwhelming joy to know future students will get to experience having you as an adviser as well. When I meet future Massari-graduates, I’ll be sure reminisce with them over how knowledgeable you are as a scientist, and what an amazing, significant impact you had on all of us.

Courtney, you’re the best mentor I could’ve asked for. Thank you for always responding to my mistakes with patience and care. I have looked up to you since the day we first met, and you inspire me with your intellect, passion, and kindness. Not only are you a gifted educator, but you have also been an incredible friend to me throughout all these years. You always have the best advice and make time to listen even in the midst of your own obstacles. I don’t know if I’ll ever be able to adequately express my gratitude, but I’m so grateful graduate school allowed us to forge this lifelong friendship.

Ivan, I wasn’t expecting to meet another Christian in graduate school so I praise God and thank Him for placing you in my life. Watching you balance your time between marriage, parenting, graduate school/work, and your faith humbles me and reminds me how much I have left to learn. I have so much appreciation for you and Betsy and our

times of fellowship together. I feel like a member of your family when I hang out with you two and the kids. Thank you for gifting me with such special experiences.

Patrick and Zahra, you two were a welcoming presence from the very beginning and my time in the Massari lab was undoubtedly shaped by both of you. Isaac, though our time together in the Massari lab was brief, I'm thankful for all the late nights and weekends we spent together working on opposite sides of the laser while listening to Passion Pit. Grace, thank you for being an integral part of our lab family during your undergraduate career. We were so lucky to have such a talented, passionate person like yourself. Thorn, you've always been a source of joy and laughter in the Massari lab. Thank you for being such a good friend and labmate. Our times together on the oscillator and regen were always a treat, despite the pain of having to realign our respective setups afterward.

Joel, you taught all of us in the Massari lab many lessons during your time as a postdoc. Listening to RHCP with you in the wet lab and hearing stories about Ollie always made my day so much better. Connor, you constantly challenge me to be a better scientist. Thanks for all the good times turning knobs together, your insightful questions, and your love of lasers. Your enthusiasm is contagious and it helped me more times than I can count. Zhihao, thank you for always providing a calming aura in the lab. Our many conversations about cats always brought a smile to my face.

Rachel, I'm so happy we had various opportunities to grow closer through classwork, softball, volleyball, and CCGS. Thanks for remaining calm when I got concussed by a softball. I'm so proud of you for getting a teaching job at St. Olaf and accomplishing exactly what you wanted, I cannot think of someone more deserving.

Meghan, I'm so glad to call you my friend. Taking quantum mechanics during my gap year was the best decision ever because I got to meet people like you. Your students at UNC Asheville are incredibly lucky to have you. I'm looking forward to hanging out with you more when we're both on the east coast!

Professor Binyomin Abrams, Professor John Straub, Professor Lawrence Ziegler, Dr. Lynetta Mier, and Dr. Jen Fore- Thank you for everything you taught me at BU.

To Professor Renee Frontiera, Professor Ken Leopold, and Professor Lee Penn, thank you for your kindness and mentorship during my time at UMN. Our department is a very special place thanks to people like you.

To my best friends Brenden and Rohini, thank you both for reaching out and continuing to spend time with me even when graduate school stress made me a grumpy person. Your company is always a refreshing connection to the real world. I never did a great job explaining what I do in lab all day, yet you two always cheered me on and told me you were proud of me. May we continue to be friends forever.

Mom, Dad, thank you for your endless love and support the last 28 years. I couldn't have done any of this without you. You both inspire me to work harder and do better every day. I'm incredibly lucky to have parents like you two that love relentlessly.

Abstract

This thesis examines a variety of vibrational probe-containing molecules such as triphenyl hydrides, CO₂, and metal carbonyls with the goal of better understanding the dynamics for each system. Particular emphasis is placed on understanding how the behavior of a restricted probe, such as one dissolved in a rigid polymer or confined to a nanopore, may differ from the same probe placed in bulk solvent or a more rubbery polymer.

The first study described herein scrutinized the vibrational heavy atom effect and its impact on ultrafast vibrational dynamics. A series of three triphenyl hydride compounds was investigated in a range of solvents by Fourier transform infrared (FTIR), infrared (IR) pump-probe, and two-dimensional infrared (2D-IR) spectroscopies. The mass of the central atom in the three compounds was varied systematically down the group 14 elements of silicon, germanium, and tin while keeping the rest of the molecule unaltered. Interestingly, frequency-frequency correlation functions obtained from 2D-IR spectra indicated that an increasingly large central atom produces small, but measurable changes in the dynamics of the solvation shell surrounding each compound.

Next, CO₂ (g) was examined via 2D-IR spectroscopy as a precursory study to understanding its behavior inside polymers. Processes which lead to dephasing of the vibrational echo such as collisions were largely circumvented by using CO₂ diluted in N₂ under ambient pressure and temperature. Off diagonal features in the 2D-IR spectra were observed which correspond to population and coherence exchange between rovibrational transitions.

Then, CO₂ (g) was dissolved inside polymers such as poly(methyl methacrylate), poly(methyl acrylate), and poly(dimethylsiloxane). These polymers with differing properties were chosen to study the impact of the glass transition on the dynamics of the dissolved CO₂ probe. Interactions between the polymeric backbone and probe also impacted the dynamics. The parameters obtained from 2D-IR studies directly correlated with the diffusivity of CO₂ through the polymer matrices.

Next, I inspected CO₂ (g) adsorbed to microporous systems such as MIL-53(Al) and ZIF-8. Preliminary FTIR studies suggest that these samples could possess a wealth of dynamic information despite narrow FTIR peaks, much like CO₂ dissolved in polymers. Experimental limitations regarding these novel systems are briefly discussed.

Lastly, I compared the dynamics of three ruthenium-bound carbonyl complexes: Ru₃CO₁₂ in bulk THF, [HRu₃(CO)₁₁]⁻ entrapped in an aluminum sol-gel, and [NEt₄][HRu₃(CO)₁₁] in bulk THF. Ru₃CO₁₂ is catalytically inactive but becomes active upon incorporation into an alumina sol-gel matrix. Pump probe and 2D-IR studies indicated that the changed dynamics are primarily due to an altered solvent shell which most likely exhibits long-range ordering. Though it is uncertain whether the increased catalytic activity of [HRu₃(CO)₁₁]⁻ is due to the presence of the hydride or this newly ordered solvent shell, the results nonetheless showcase 2D-IR's efficacy in sensing dynamics of confined environments.

Table of Contents

<i>Abstract</i>	<i>iv</i>
<i>List of Tables</i>	<i>x</i>
<i>List of Figures</i>	<i>xi</i>
<i>List of Abbreviations</i>	<i>xvi</i>
1. Introduction – Solvation and Diffusion within Confined Spaces	1
1.1 Motivation	2
1.2 Basic Properties of Solvation	5
1.2.1 Definition of Solvation	5
1.2.2 Vibrational Stark Effect	6
1.3 Diffusion	7
1.3.1 Diffusion in a Continuum – Fick’s Laws	7
1.3.2 The Polymeric Free Volume Model.....	8
1.3.3 Free Volume Diffusion Mechanisms	10
1.3.4 Wobbling in a Cone Analysis	11
2. Linear versus Nonlinear Infrared Spectroscopy	18
2.1 Limitations of Linear Spectroscopy	19
2.2 Linear Spectroscopy	22
2.3 The Extension to Third Order Techniques, Including 2D-IR	29
2.4 Two Sided Feynman Diagrams: A Tool for Understanding Pulse Sequences	30

2.5 Rephasing and Non-Rephasing Pulse Sequences	33
2.6 Femtosecond Pulsed Laser Instrumentation	36
2.7 2D-IR Instrumentation.....	37
2.8 2D-IR Processing & Analysis.....	38
3. <i>The Vibrational Heavy Atom Effect and its Impact on Relaxation and Spectral Diffusion in Triphenyl Hydride Complexes</i>.....	42
3.1 Chapter Summary	43
3.2 Introduction.....	43
3.3 Materials & Methods.....	46
3.4 Results and Discussion.....	48
3.5 Conclusions.....	61
3.6 Full Set of 2D-IR Data	62
4. <i>Ultrafast Studies of CO₂ (g) as a Precursor to Dissolved Gases</i>.....	65
4.1 Chapter Summary	66
4.2 Introduction.....	66
4.3 Materials & Methods.....	68
4.4 Results and Discussion.....	69
4.5 Conclusions.....	79
4.6 Full Set of 2D-IR Data	80

5. <i>CO₂ Diffusion in Polymeric Matrices</i>	81
5.1 Chapter Summary	82
5.2 Introduction	82
5.3 Materials & Methods	85
5.3.1 Polymeric Sample Preparation.....	85
5.3.2 Ultrafast Data Collection (2D-IR, pump probe anisotropy).....	87
5.4 Results and Discussion	89
5.5 Conclusion	105
5.6 Full Set of 2D-IR Data	108
6. <i>Carbon Dioxide in Microporous Structures</i>	111
6.1 Chapter Summary	112
6.2 Introduction	112
6.3 Materials & Methods	114
6.3.1 MIL-53(Al) KBr Pellet Preparation.....	114
6.3.2 ZIF-8 KBr Pellet Preparation.....	114
6.3.3 MIL-53(Al) Sample Activation	115
6.3.4 ZIF-8 Sample Activation	115
6.3.5 FTIR Spectra Collection	116
6.3.6 Ultrafast Data Collection	116
6.4 Results and Discussion	117
6.5 Conclusion	122

7. Ruthenium Hydride Formation in Sol-Gel Glasses Results in Different Ultrafast Vibrational Dynamics	123
7.1 Chapter Summary	124
7.2 Introduction.....	124
7.3 Experimental	126
7.3.1 Materials	126
7.3.2 Sol-Gel Formation	126
7.3.3 Synthesis of [NEt ₄][HRu ₃ (CO) ₁₁].....	127
7.3.4 FTIR Measurements	127
7.3.5 2D-IR Measurements	128
7.4 Results and Discussion.....	128
7.5 Conclusion	138
7.6 Full Set of 2D-IR Data	140
<i>Bibliography</i>.....	143

List of Tables

Table 3.1. Hydride vibrational lifetimes. Errors represent the standard error of the fit... 52	52
Table 3.2. FFCF parameters obtained for the three triphenyl hydride compounds in chloroform.....60	60
Table 5.1. Chemical structure of polymers studied with glass transition temperatures (T_g) and mutual diffusion coefficients (D). The top row of T_g values are obtained from DSC measurements, and the bottom from the literature.84	84
Table 5.2 Values extracted from a pseudo-Voigt fit to the FTIR spectra in Figure 5.1. .. 90	90
Table 5.3. Population and orientational decay time constants for CO_2 in PMA, PMMA, and PDMS.92	92
Table 5.4. Full results of biexponential fits for pump probe anisotropy of CO_2 dissolved in the three polymer systems.94	94
Table 5.5. Parameters obtained from wobbling-in-a-cone analysis of CO_2 in the three polymers.95	95
Table 5.6. Amplitudes (A_1) and time constants (τ_1) for single exponential decay plus constant (A_0) fit to CLS values as a function of T_w 101	101
Table 5.7. Parameters obtained from the FFCF fit of the CO_2 ν_3 mode when dissolved in PDMS, PMMA, and PMA. 104	104
Table 6.1. Pseudo-Voigt parameters extracted from FTIR spectra of CO_2 loaded on ZIF-8 and MIL-53(Al) KBr pellets 118	118
Table 7.1. FFCF Fit Parameters of the Ruthenium Compounds.136	136

List of Figures

Figure 1.1. Pictorial representation of a polymeric sample at two temperatures, above T_g (a) and below T_g (b). White represents void space between polymer chains. Blue shaded areas represent polymer chains. Grey shaded areas represent regions in which thermally activated segmental mobility will occupy additional volume..... 10

Figure 1.2. A diagram depicting a simplified wobbling in a cone model. The red vector μ is the unique symmetry axis of the probe. θ is the instantaneous angle between μ and z , where z is assumed to be normal to the sample surface. θ_c represents the range of angles the probe explores within the cone. 13

Figure 2.1. Panels a-c show an FTIR peak (black line) with a Gaussian profile. Panel (a) shows a single subensemble of oscillators and their homogeneous linewidth with a Lorentzian profile. In (b) additional subensembles are drawn in red, each with their own homogeneous linewidth which contribute to static inhomogeneity. Panel (c) portrays the process of spectral diffusion in which a probe may move among subensembles..... 20

Figure 2.2. A Feynman diagram depicting the time evolution of the two state system in according to the R_1 energetic pathway. Light interacting with the sample is indicated by solid arrows, whereas a dotted arrow indicates signal emitted by the sample..... 31

Figure 2.3. Feynman diagrams showing four different energetic pathways that lead to separate terms in the third order molecular response function. R_1 and R_2 are rephasing pathways, whereas R_4 and R_5 are non-rephasing pathways. Details regarding their interpretation can be found in the text. 33

Figure 2.4 Two example 2D-IR spectra of TriPS in chloroform at an early T_w (0.5 ps) on the left and a later T_w (5 ps) on the right. White arrows are drawn to emphasize the pronounced diagonal elongation at early T_w s. 39

Figure 3.1. Solvent-subtracted, baselined, and normalized FTIR spectra of the M-H vibrational mode for TriPS, TriPG, and TriPT in pentane (black), chloroform (red), and isopropanol (blue). 48

Figure 3.2. Center frequencies for the ν_{Si-H} (circles), ν_{Ge-H} (triangles), and ν_{Sn-H} (squares) in various solvents. Black, red and blue symbols indicate samples in pentane, chloroform, and isopropanol, respectively, that were further studied via pump-probe spectroscopy..... 49

Figure 3.3. FWHM values for the M-H stretch of TriPS (circles), TriPG (triangles), and TriPT (squares) in various solvents. 50

Figure 3.4. IR pump probe decays for the hydride stretch on (a) TriPS near 2132 cm^{-1} , (b) TriPG near 2045 cm^{-1} , and (c) TriPT near 1855 cm^{-1} . Black, red, and blue colors

correspond to pentane, chloroform, and isopropanol, respectively, in all three frames. Overlaid solid lines of the same color show single exponential curves that fit the data. Error is reflected in the fit to single exponential parameters mentioned in Table 3.1..... 51

Figure 3.5. Rate coefficients for energy relaxation as a function of the inverse mass of the central atom (Si = circles, Ge = squares, Sn = triangles) in pentane (black), chloroform (red), and isopropanol (blue). The solid line is a linear regression fit to the pentane data points only..... 53

Figure 3.6. DFT calculated vibrational frequencies and intensities for TriPS (black), TriPG (red), TriPT (blue), and TriPS- d_1 (green) in the gas phase using the LANL2DZ functional and B3LYP basis set. Figure 3.7. IR pump-probe decay for the $\nu=0-1$ transition of the deuteride stretch ($\nu_{\text{Si-D}}$) on TriPS- d_1 at 1550 cm^{-1} 55

Figure 3.8. Representative 2D-IR spectra of (top to bottom) TriPS, TriPG, and TriPT in chloroform. Spectra in the left column were recorded at $T_w = 0.5 \text{ ps}$; spectra on the right column were recorded at $T_w = 5 \text{ ps}$ 57

Figure 3.9. CLS values as a function of T_w for TriPS (black circles), TriPG (red squares), and TriPT (blue triangles). All three CLS decays were plotted to a single exponential and decay to approximately zero at long T_w s. Error bars represent the standard deviation of CLS values for a given T_w across three scans..... 59

Figure 3.10. CLS values as a function of T_w at shorter T_w s and with a logarithmic y-axis to highlight subtle differences on this time scale. Error bars represent the standard deviation of CLS values for a given T_w across three scans..... 59

Figure 3.11. Trends in FFCF parameters τ (black circles) and Γ (red squares) as a function of atomic radius for TriPS, TriPG, and TriPT in CHCl_3 60

Figure 3.12: Complete set of averaged 2D-IR spectra for the $\nu_{\text{Si-H}}$ stretch of TriPS in CHCl_3 at a range of T_w s. 62

Figure 3.13. Complete set of averaged 2D-IR spectra for the $\nu_{\text{Ge-H}}$ stretch of TriPG in CHCl_3 at a range of T_w s. 63

Figure 4.1. 2D-IR spectra of gaseous CO_2 at $6 \times 10^{-4} \text{ atm}$ diluted in N_2 to 1 atm at a) $T_w = 1 \text{ ps}$ and b) $T_w = 100 \text{ ps}$. The FTIR spectrum of CO_2 is plotted above each 2D-IR spectrum for reference. 70

Figure 4.2. Six density matrix pathways which lead to 2D-IR signals for (a and b) ground state bleach, (c and d) population exchange, and (e and f) coherence exchange. Straight arrows represent the system interacting with an IR pulse on either the bra or ket side of the density matrix (solid and dashed arrows respectively); wavy lines indicate emission of

vibrational echo signal.....	71
Figure 4.3. Off-diagonal intensity for the $\nu=0-1$ transition normalized by the on-diagonal intensity as a function of T_w	73
Figure 4.4. Schematic of a typical rotational-vibrational spectrum in which the transition spacing decreases in both P- and R-branches toward higher frequencies. The lower frame shows the resulting off-diagonal peaks that occur with downward curvature, as seen in experimentally in Figure 1.....	74
Figure 4.5. Off-diagonal peak positions extracted from the 2D-IR spectrum at $T_w = 1$ ps overlaid with Equation 3 (solid black line) using best fit parameters: $\nu_0 = 2351$ cm^{-1} , $Be = 0.39$ cm^{-1} , $\alpha e = 0.0029$ cm^{-1}	76
Figure 4.6. Absolute value 2D-IR spectrum at $T_w = 1$ ps for CO_2 gas measured with a higher resolution diffraction grating to identify peak twinning in the off-diagonal quadrants.....	77
Figure 4.7. 2D-IR spectra at $T_w = 0.5$ ps for a) CO_2 gas dissolved inside PMMA, b) CO_2 gas by itself, and c) the resultant spectrum upon subtracting b from a.....	78
Figure 4.8. Full set of 2D-IR spectra probing the asymmetric stretch of gaseous CO_2 at a range of waiting time T_{ws} , as indicated in the upper left hand corner of each plot.....	80
Figure 5.1. Normalized FTIR spectra of the CO_2 0-1 asymmetric stretch in PMMA (black), PMA (red), and PDMS (blue).....	89
Figure 5.2. Normalized population decays measured for the 0-1 ν_3 for CO_2 in PMMA (black), PMA (red), and PDMS (blue). Markers show experimental data, solid lines show best biexponential fit.....	92
Figure 5.3. Polarization anisotropy decays for PMMA (black), PMA (red), and PDMS (blue). Overlaid solid lines are biexponential fits.....	93
Figure 5.4. DSC measurements indicate the PDMS sample (blue) encounters the glass transition at -124°C , whereas this transition occurs at -18°C for PMA (red) and 93°C for PMMA (black). Literature values for transitions are shown in Table 5.1 in parentheses. 96	
Figure 5.5. 2D-IR spectra of the CO_2 ν_3 mode, dissolved in PMMA (a, b), PMA (c, d), and PDMS (e, f) at $T_w = 0.5$ ps (left column) and $T_w = 10$ ps (right column).....	99
Figure 5.6. Off-diagonal intensity normalized by the on-diagonal intensity at the emission frequency for PMMA (black circles), PMA (red squares), and PDMS (blue triangles).	

The data demonstrate that the off-diagonal intensity does not grow in as T_w is increased for any of the polymeric systems.	100
Figure 5.7. CLS as a function of T_w for PMMA (black circles), PMA (red squares), and PDMS (blue triangles) measured at 25 °C. Each set of data were fit to a single exponential with an offset. Open green triangle markers show CLS values measured in PMMA sample heated to 150 °C.	101
Figure 5.8. 2D-IR spectra of PMMA heated above its T_g mimic those of PMA which is well beyond its T_g at room temperature. Shown is $T_w = 0.5$ ps (upper left) and $T_w = 20$ ps (upper right). The 1-2 transition was chosen for analysis due to on-diagonal scatter and partial gas phase contribution.	103
Figure 5.9. CLS plotted as a function of T_w for the 0-1 (black) and 1-2 (green) peak associated with the asymmetric stretch of CO_2 in PMMA, collected at room temperature. Though the 1-2 has more noise, the data points follow a similar trend at long T_w s. These values were tabulated to confirm the validity of comparing the CLS values of the 1-2 in heated PMMA to those of the 0-1 in room temperature PMA.	103
Figure 5.10. The CO_2 cone diffusion times and spectral dephasing times as a function of the relative viscosity parameter (the inverse of the mutual diffusion coefficients for CO_2 in each of the three polymers studied).	107
Figure 5.11. 2D-IR spectra of the CO_2 ν_3 mode, dissolved in PDMS at a range of waiting time T_w values.	108
Figure 5.12. 2D-IR spectra of the CO_2 ν_3 mode, dissolved in PMMA at a range of waiting time T_w values.	109
Figure 5.13. 2D-IR spectra of the CO_2 ν_3 mode, dissolved in PMA at a range of waiting time T_w values.	110
Figure 6.1. FTIR spectra of CO_2 ν_3 stretch when adsorbed to ZIF-8 (a) and MIL-53(b) KBr pellets. Black lines in both spectra correspond to the respective samples before activation and CO_2 loading.	118
Figure 6.2. Sample 2D-IR spectrum at $T_w = 3$ ps for CO_2 in MIL-53(AI). The black circled region is a possible 1-2 peak but obfuscated by both scatter and gaseous CO_2 . ..	120
Figure 7.1. Normalized FTIR spectra of $Ru_3(CO)_{12}$ In THF (black) and entrapped in the alumina sol-gel (red). Upon sol-gel formation, the modes in $Ru_3(CO)_{12}$ undergo a dramatic red shift. The spectrum of the synthesized $[NEt_4][HRu_3(CO)_{11}]$ dissolved in THF is also shown (blue).	129

Figure 7.2. Pump-probe spectra of a) $\text{Ru}_3(\text{CO})_{12}$ in THF, b) $[\text{HRu}_3(\text{CO})_{11}]^-$ entrapped in the alumina sol-gel, and c) $[\text{NEt}_4][\text{HRu}_3(\text{CO})_{11}]$ in THF.	130
Figure 7.3. Pump probe population decay for the carbonyl stretch of $\text{Ru}_3(\text{CO})_{12}$ in THF (black), $[\text{HRu}_3(\text{CO})_{11}]^-$ in the alumina sol-gel (red), and $[\text{NEt}_4][\text{HRu}_3(\text{CO})_{11}]$ in THF (blue). Markers represent experimental data, solid lines show best biexponential fit....	131
Figure 7.4. CLS decays for $\text{Ru}_3(\text{CO})_{12}$ in THF (black), $[\text{HRu}_3(\text{CO})_{11}]^-$ in the alumina sol-gel (red), and $[\text{NEt}_4][\text{HRu}_3(\text{CO})_{11}]$ in THF (blue).	133
Figure 7.5. 2D-IR of the carbonyl stretches of $\text{Ru}_3\text{CO}_{12}$ in THF at a range of T_{ws}	140
Figure 7.6. 2D-IR spectra of the carbonyl stretches of sol-gel encapsulated $[\text{HRu}_3(\text{CO})_{11}]^-$ at a range of T_{ws}	141
Figure 7.7. 2D-IR spectra of the carbonyl stretches of $[\text{NEt}_4][\text{HRu}_3(\text{CO})_{11}]$ in THF at a range of T_{ws}	142

List of Abbreviations

2D-IR	Two-dimensional infrared
B3LYP	Becke, 3-parameter, Lee-Yang-Parr exchange correlation functional
CDR	Carbon dioxide removal
CHCl₃	Chloroform
CLS	Center line slope
CW	Continuous wave
DFT	Density Functional Theory
DMF	Dimethylformamide
FTIR	Fourier transform infrared
FWHM	Full width half max
IR	Infrared
IVR	Intramolecular vibrational redistribution
LANL2DZ	Los Alamos national laboratory 2 double ζ
LO	Local Oscillator
MCT	Mercury cadmium telluride (HgCdTe) detector
MD	Molecular dynamics
MIL	Materials of Institute Lavoisier

MOF	Metal organic framework
NMR	Nuclear Magnetic Resonance
OPA	Optical parametric amplifier
PDMS	poly(dimethylsiloxane)
PMA	poly(methyl acrylate)
PMMA	poly(methyl methacrylate)
THF	Tetrahydrofuran
TriPG	Triphenyl germanium hydride
TriPS	Triphenyl silane
TriPT	Triphenyl tin hydride
VER	Vibrational energy relaxation
VHAE	Vibrational heavy atom effect
VSE	Vibrational stark effect
ZIF	Zeolitic imidazolate framework

1. Introduction – Solvation and Diffusion within Confined Spaces

1.1 Motivation

Many processes of scientific and societal interest rely on dynamics occurring in the femtosecond or picosecond time domain. As an example, imagine a β -amyloid fibril forming in an individual's brain that might eventually give rise to Alzheimer's disease. Water molecules incorporated within the tertiary structure have dipoles which constantly interact with those of the protein. However, rotational hindrance of water molecules near certain sites of the amyloid produce structural fluctuations in the protein over the span of mere picoseconds. The induced fluctuations are thought to exacerbate protein misfolding events.¹ This leads to further accumulation of the protein aggregates postulated to produce disease.

Depending on the material, picosecond structural fluctuations may also affect electron mobility for thin-film semiconductors. Prior work by Eigner et al. showed that specific dopants in polyaniline thin films improved charge mobility but also eliminated sub-picosecond motions.² An improved understanding of the relationship between structure, ultrafast observables, and time-averaged observables (e.g mobility) could allow for the design and optimization of semiconductor materials.

Herein dynamics will refer to structural vibrations, nuclear displacements, and energetic fluctuations that occur on picosecond and femtosecond time scales. These motions hold relevance in scenarios as different as amyloid formation and electron mobility, yet they proceed so quickly that they must be studied via nonlinear spectroscopies with ultrashort pulses.³ So long as a molecule contains a vibrational mode with a sufficiently large transition dipole, it can act as a probe for pump probe and two-

dimensional infrared (2D-IR) spectroscopy. Pump probe spectroscopy provides information regarding the population decay of an excited vibrational probe. Changes in vibrational lifetime inform whether the vibrational probe undergoes additional coupling to intramolecular modes or the surroundings, which can expedite vibrational energy relaxation (VER). However, the exact mechanisms of VER are difficult to discern without the use of a multi-dimensional method such as 2D-IR. The first 2D-IR measurement published in 1998⁴ guided subsequent studies on a variety of systems such as ionic liquids,⁵ sol-gel pores,⁶ and nanoparticle surfaces.⁷

With 2D-IR, dynamics can be separated into homogeneous and inhomogeneous contributions and the time constants for these contributions are also acquired. We define these terms and describe their contribution to the vibrational line shape in Chapter 2. The multi-dimensional nature of 2D-IR also allows for monitoring coherence or population exchange between vibrational probes by observing the behavior of off-diagonal peaks in a 2D-IR spectrum. Though 2D-IR cannot ascertain the exact origin of a dynamic motion, the results can inform and improve computational studies such as MD simulations.

The work herein focuses on understanding the dynamics of vibrational probes in confined environments. Microporous structures of interest such as metal-organic frameworks often contain heavy atoms within the matrix. The impact of heavy atoms on the ultrafast dynamics, especially those of the surrounding solvation shell, were first interrogated by collecting pump probe and 2D-IR spectra for a series of compounds that follow formula Ph_3MH where M is the central atom. With a better understanding of how heavy constituents like those in a microporous structure could affect ultrafast dynamics,

the overarching goals of this research shifted toward explaining the ultrafast behavior of CO₂ inside solid-state systems.

My investigations of CO₂ that built upon a prior labmate's measurements focused on monitoring the dynamics of the asymmetric stretch. These studies were informed by preliminary measurements of CO₂ (g) diluted in N₂ (g) under ambient temperature and pressure. The experiments identified the origin of off diagonal peaks that occur for CO₂ when it is not dissolved in a polymeric matrix.

The next series of experiments measured the ultrafast dynamics of CO₂ when dissolved inside a series of polymers with varying glass transition temperatures and affinity for the CO₂ probe. The parameters and time coefficients obtained from FFCF fitting can determine the extent to which rigid surroundings such as a crosslinked polymer or a slowly moving solvent bath affect the dynamics of the asymmetric stretch.

The methods of sample preparation and gas loading are then extended toward FTIR studies of CO₂ adsorbed on various microporous structures including MIL-53(Al) and ZIF-8. The limitations of these samples and future ultrafast measurements of interest are briefly discussed.

The final chapter describes ultrafast behavior of ruthenium-bound carbonyls with comparisons made between the dynamics imparted by bulk solvent versus solvent confined inside a silica nanopore. My measurements showed that the CO stretches in both hydrides are highly sensitive to both local and long-range surroundings, as evidenced by inhomogeneous offsets that had a small yet genuine difference in their magnitude upon introduction of the alumina matrix. Though more information is needed to ascertain the

origins of catalytic activity for this system, 2D-IR nonetheless revealed new information about the nature of the THF solvent shell in these samples.

The spectroscopic studies described herein ultimately aim to establish a connection between ultrafast motions and time-averaged properties of molecular systems. An improved understanding of the femtosecond and picosecond motions in confined systems provides insight on how individual, discrete motions of the vibrational probe and the surroundings average over time to contribute toward properties such as gas diffusion constants.

1.2 Basic Properties of Solvation

1.2.1 Definition of Solvation

Solvation refers to interactions between a solute and a solvent which lower the overall potential energy, resulting in a stabilizing effect.⁸ Intermolecular attraction must overcome intermolecular repulsion for solvation to occur. A variety of forces contribute to this interplay between attraction and repulsion such as hydrogen bonding, dipole-dipole, and Van der Waals forces.⁹ These forces are worth understanding and considering in the context of 2D-IR experiments because the vibrational probes being studied are not isolated in space or time. Throughout the course of an ultrafast experiment, the probes constantly rotate and translate. The solvent surroundings themselves also constantly move. Despite some of the processes occurring on different time scales,¹⁰ vibrational modes of the solvent and solute are nonetheless sensitive to one another via the Vibrational Stark Effect (VSE).

1.2.2 Vibrational Stark Effect

Johannes Stark first discovered the Stark effect in 1913 when noting that an external electric field applied to hydrogen gas results in spectral feature splitting.¹¹ The theory has since been applied toward studying vibrational modes: An external electric field can alter both the frequency of vibrational transitions and their respective transition dipoles;^{12, 13} the solute and surroundings can therefore both sense one another. The VSE is what allows us to learn about our probe and its surroundings during a 2D-IR experiment by monitoring changes in frequency of an oscillating mode as a function of time. The shift in vibrational frequency ($\Delta\bar{\nu}$, cm^{-1}) is quantified as follows:

$$hc\Delta\bar{\nu} = -\Delta\vec{\mu} \cdot \vec{F}_{\text{ext}} \quad 1.1$$

Where h is Planck's constant and c is the speed of light. $\Delta\vec{\mu}$ is the difference dipole moment referring to changes between the ground and excited state, and \vec{F}_{ext} is the electrostatic field applied by the surroundings. The difference dipole $\Delta\vec{\mu}$ has units $\text{cm}^{-1}/(\text{MV}/\text{cm})$ and is computed by accounting for the change in bond length that occurs for anharmonic molecules upon excitation.¹⁴ Vibrational modes that exhibit a larger change in bond length (d) will possess a larger $\Delta\vec{\mu}$ and exhibit larger shifts in response to external fields. Therefore the difference dipole is analogously referred to as the Stark tuning rate.

A typical vibrational probe will have a Stark tuning rate ranging from 0.5-2 $\text{cm}^{-1}/(\text{MV}/\text{cm})$.¹⁴ A $\Delta\vec{\mu}$ value of 1 would therefore refer to a vibrational mode that shifts 1 cm^{-1} in response to an electric field of 1 MV/cm applied along the vibrational axis. The VSE makes a few assumptions about the behavior of the vibrational probe: An external field applied by the surroundings causes a linear shift in the vibrational frequency, the

oscillating mode is decoupled from other vibrations, and that the shift is solely due to non-covalent interactions.^{13, 15} Understanding the VSE plays an integral role in the upcoming discussions of vibrational probes in confined environments, with particular emphasis on gas dissolved in polymers.

1.3 Diffusion

1.3.1 Diffusion in a Continuum – Fick’s Laws

Diffusion in a single dimension is most commonly modeled by Fick’s laws, which are as follows:

$$J = -D_m \frac{dc}{dx} \quad 1.2$$

$$\frac{dc}{dt} = D_m \frac{d^2c}{dx^2} \quad 1.3$$

Herein J represents the flux of the particle flow with units of $\text{mol} \cdot \text{m}^{-2} \text{s}^{-1}$, D_m is the mutual diffusion constant with units $\text{m}^2 \text{s}^{-1}$, and c represents the concentration of the diffusing solute. The minus sign conveys the fact that flow would occur in the direction of decreasing concentration in order to equilibrate a concentration gradient. In equation 1.3, $\frac{dc}{dt}$ represents the change in concentration over time and relates to the same D_m constant.

Alternatively, diffusion may be considered in the context of a single solute molecule:

$$\lim_{t \rightarrow \infty} \frac{\langle r^2 \rangle}{t} = \frac{Nb^2}{t} \equiv 6D_t \quad 1.4$$

In this scenario, for some elapsed amount of time t the molecule is assumed to take N random steps with an average length b . The mean square displacement $\langle r^2 \rangle$ can be related

to D_t which is the tracer diffusion constant. Other texts describe D_t as the self-diffusion coefficient. To reiterate, D_t relates to a single molecule whereas D_m would refer to a collection of molecules. By continuing to focus on diffusion from the perspective of a single molecule, we can invoke the Stokes-Einstein relation which is as follows:

$$D_t = \frac{k_b T}{6\pi\eta_s R} \quad 1.5$$

Here η_s represents the viscosity of the solvent surroundings and R is the radius of the diffusing molecule. For sufficiently low concentrations of solute we can utilize the approximation $D_t \approx D_m$. The literature contains examples of analytical solutions to relate D_t and D_m when dealing with concentrated solute, but they are not necessary for the systems described in this thesis. Following this approximation will allow for relating ultrafast motions of vibrational probes to macroscopic properties of a system such as diffusion constants.

1.3.2 The Polymeric Free Volume Model

Fick's laws described above refer to diffusion of a solute molecule traversing a continuum of solvent, in which the solvent is represented as hard spheres. These equations do not necessarily describe the behavior of the surroundings, i.e. the polymer. An alternative description of diffusion is attained by considering the free volume of the solute-polymer sample. The simplest expression for free volume can be written as the following¹⁶:

$$V_{free} = V_{total} - V_{occ} \quad 1.6$$

Where V_{total} refers to the total space occupied by the sample, V_{free} is the void between polymeric chains, and V_{occ} is the space occupied by polymeric chains. This expression for V_{free} works for characterizing polymers below the glass transition T_g . However, the samples discussed in this thesis exhibit a range of thermal properties. This necessitates a brief description of T_g to more explicitly define V_{free} .

The glass transition T_g represents the temperature at which the amorphous regions of a polymer change from a glassy state to a rubbery state.¹⁶ Factors such as intermolecular forces, the number of cross-links in a sample, and the flexibility of both the main chain and side chains influence T_g .¹⁷ The onset of the rubbery state is due to segmental mobility, i.e thermal activation of additional polymeric motions. The glass transition is typically associated with an increased rate of α -relaxation processes, in which cooperative motion allows multiple monomers in the polymer backbone to concurrently rotate.^{18, 19} For polymers above T_g it is more accurate to express the polymer free volume as the following:^{16, 20}

$$V_{free}(T) = V_{total} - V_{occ}(T) \quad 1.7$$

The temperature dependence of $V_{occ}(T)$ and $V_{free}(T)$ account for the fact that the polymeric chains will inevitably undergo additional translations, rotations, and vibrations as the sample acquires kinetic energy above the glass transition. The sample itself could also have a thermal expansion coefficient that no longer scales linearly with temperature. A diagram portraying the difference in free volume above and below T_g is presented in Figure 1.1.

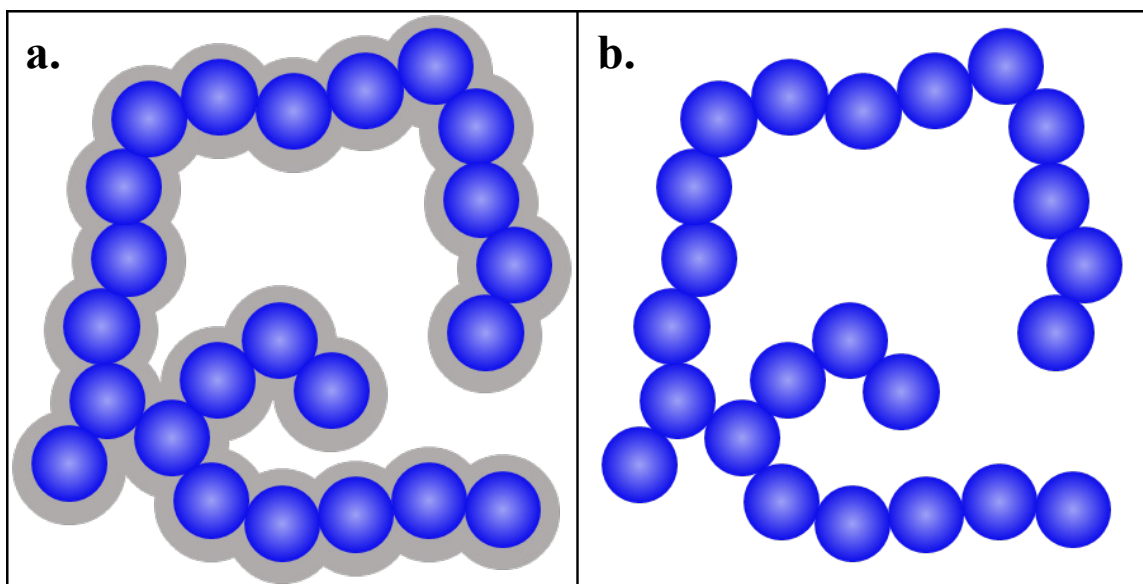


Figure 1.1. Pictorial representation of a polymeric sample at two temperatures, above T_g (a) and below T_g (b). White represents void space between polymer chains. Blue shaded areas represent polymer chains. Grey shaded areas represent regions in which thermally activated segmental mobility will occupy additional volume.

1.3.3 Free Volume Diffusion Mechanisms

The first free volume diffusive model published by Cohen and Turnbull in 1959 characterized the diffusion constant for a solute diffusing through a liquid of hard spheres²¹ and expressed it as being dependent on both penetrant size and the likelihood of the surroundings to create a sufficiently large opening. In the context of these models, the diffusion constant of a penetrant in a polymer depends on the constantly-evolving framework which undergoes random fluctuations that open and close pockets of free space. When the sample is at or above T_g , the opening of cavities is driven by α -relaxation in which a large section of the backbone collectively rotates. For samples below T_g , β -relaxation is the primary source of cavity migration via motions of side chains and single monomers.^{22, 23}

The appearance of a sufficiently large free volume allows the penetrant molecule an

opportunity to hop from one free volume cavity to another. Molecular dynamics (MD) simulations have demonstrated the stochastic hopping mechanism in glassy and rubbery polymers alike.^{24, 25} Calculations also indicate the solute oscillates in a cavity when not experiencing a hop.^{24, 26} In contrast to free volume diffusion mechanisms, molecular models such as those from DiBenedetto and Paul suggest that the polymer matrix must acquire a certain activation energy before a cavity appears that allows the penetrant to undergo a diffusive hop.²⁷ The various theories at our disposal have each demonstrated success replicating properties such as the pressure and temperature dependence of diffusion constants.²² Therefore it is worth considering the solute's own degrees of freedom and to what extent they may factor into diffusion.

1.3.4 Wobbling in a Cone Analysis

The infrared spectroscopic techniques employed in this thesis aim to describe the behavior of a vibrational probe in complex environments such as the free space of a polymer matrix or the inner surface of a sol-gel pore. Infrared pump probe anisotropy can recover interesting parameters of a probe such as the amount of time it takes for the vibrational dipole to reorient after excitation.²⁸ These findings are especially relevant for considering gaseous probes dissolved inside polymer matrices to understand mechanisms of diffusion from the perspective of the penetrant. The experimental setup for a pump probe anisotropy experiment will be discussed in Chapter 5. This section focuses on the underlying theory necessary to apply the wobbling in a cone model.

Dielectric relaxation experiments of supercooled liquids conducted by Shears and Williams in 1973 were some of the first to propose that orientation relaxation of a dipole

occurs in a restricted solid angle instead of a sphere of possible angles extending from the axis of the molecule.²⁹ The mathematical formalism to explain this phenomenon was developed by Warchol and Vaughan, who successfully modeled the dielectric correlation function by describing the molecule as a linear structure diffusing in a cylindrical cavity. When the molecule's length exceeds the diameter of the cylinder, the diffusion is restricted to a range of polar angles.³⁰ Work by Wang and Pecora as well as Kinoshita further extended the theory to processes of light scattering and fluorescence depolarization for probes that are trapped in immobile matrices or adhered to the surface of a bilayer.^{31, 32} Subsequent refinements by Lipari and Szabo account for situations in which the probe may somehow be restricted, yet the surrounding matrix is still mobile.³³ The Szabo interpretation of the wobbling in a cone model has successfully described rotational dynamics for a variety of systems such as water confined in reverse micelles²⁸ and CO₂ dissolved in ionic liquids^{5, 34, 35} making its application here a straightforward extension of the existing literature.

Figure 1.2 depicts the motions associated with a simplified wobbling in a cone model. It is assumed that the emission or absorption dipole associated with the mode of interest is collinear with the unique symmetry axis of the molecule (C_∞), indicated by the vector $\hat{\mu}$. Henceforth in this discussion we assume the mode of interest along C_∞ is a vibrational transition.

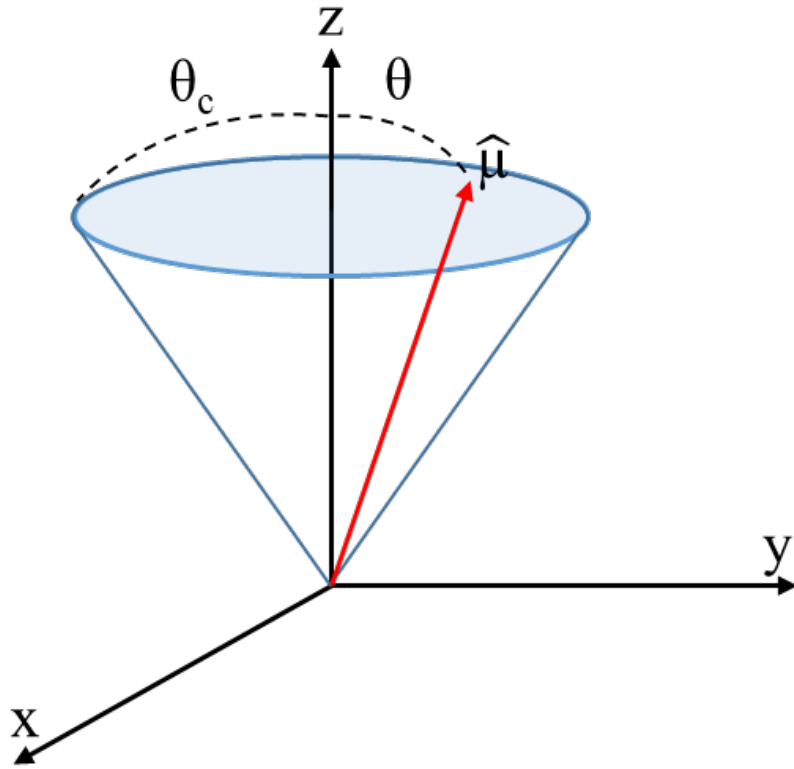


Figure 1.2. A diagram depicting a simplified wobbling in a cone model. The red vector $\hat{\mu}$ is the unique symmetry axis of the probe. θ is the instantaneous angle between $\hat{\mu}$ and z , where z is assumed to be normal to the sample surface. θ_c represents the range of angles the probe explores within the cone.

After exciting the mode lying along $\hat{\mu}$ with some arbitrary polarization of light, the excited state population $P(t)$ will decay according to sample parameters such as the vibrational lifetime. Ordinarily vibrational population relaxation is obfuscated by rotational contributions, which can be omitted by using a polarizer set to the magic angle.³⁶

For pump probe anisotropy experiments, an analyzer polarizer that is set -45° or $+45^\circ$ relative to the 45° pump will resolve parallel and perpendicular contributions to population decay. The parallel ($S_{\parallel}(t)$) and perpendicular ($S_{\perp}(t)$) signals give rise to the normalized pure population decay through the following relation, free of any rotational contribution:⁵

$$P(t) = \frac{[S_{\parallel}(t) + 2S_{\perp}(t)]}{3} \quad 1.8$$

The second order Legendre polynomial correlation function describes the orientational behavior of the transition dipole as a function of time, and is expressed as the following:³³

$$C_2(t) = \langle P_2(\hat{\mu}(t) \cdot \hat{\mu}(0)) \rangle \quad 1.9$$

Where $P_2(x) = (3x^2 - 1)/2$, and the $\hat{\mu}(t)$ term represents the orientation of the probe at time t . The measured parallel and perpendicular signal measured can be related to the polarization anisotropy $r(t)$ via the following:^{33, 37}

$$r(t) = \frac{S_{\parallel}(t) - S_{\perp}(t)}{S_{\parallel}(t) + 2S_{\perp}(t)} = 0.4 \cdot C_2(t) \quad 1.10$$

In this formalism at time $t = 0$, $r(t)$ and $C_2(t)$ have theoretical maxima of 0.4 and 1, respectively. A $r(t)$ value of 0.4 indicates the dipoles retained orientational correlation following interaction with the polarized pump pulse, whereas an $r(t)$ value of 0 indicates complete reorientation. The anisotropic decay for bulk solutions like water can be fit to a single exponential. This is not the case for restricted vibrational probes,²⁸ especially the systems explored in this thesis. Wobbling in a cone analysis applies well to systems in which $r(t)$ can be fit to a biexponential function such as:^{28, 31, 33, 38}

$$r(t) = A_1 e^{-\frac{t}{\tau_1}} + A_2 e^{-\frac{t}{\tau_2}} \quad 1.11$$

Where A_1 and A_2 represent the amplitudes of exponentials with time constants τ_1 and τ_2 respectively. The amount of time it takes the wobbling probe to explore the entire cone is given by τ_c and is obtained by solving the following:²⁸

$$\tau_c = (\tau_1^{-1} - \tau_2^{-1})^{-1} \quad 1.12$$

The τ_1 and τ_2 values are the same numbers obtained from performing a biexponential fit on $r(t)$ as mentioned in equation 1.11. Time constant τ_m refers to how long it would take the probes to undergo complete orientational relaxation which would result in a $r(t)$ value of 0. During this step the entire cone moves to explore a greater range of environments. τ_m is equivalent to τ_2 and is obtained from equation 1.11. The order parameter Q^2 ranges from 0 to 1 and describes the extent to which orientational diffusion is restricted. It is calculated as:²⁸

$$Q^2 = (2.5 * A_2) \quad 1.13$$

Where A_2 is the slow decaying component of the fit mentioned in equation 1.11. When $Q^2 = 0$, the system is able to undergo complete reorientation whereas $Q^2 = 1$ implies the probe is too restricted to wobble in the cone.²⁸

It is worth noting that although the systems explored in this thesis fit well to biexponential functions with the aforementioned τ_c and τ_m time constants, the data inherently possess a third time constant which belongs to the inertial component of the wobbling behavior. The inertial cone refers to the range of prepared starting positions for the probe when light first interacts with the sample, that then undergo a fast relaxation step within ~ 100 fs.^{28, 39} This fast decay has been observed in multiple types of rotationally constricted systems adhering to the aforementioned Szabo model such as water confined in reverse micelles²⁸ and CO₂ dissolved in ionic liquids^{5, 34, 35} The presence of the inertial component is indicated by a fast drop in $r(t)$ signal at time $t = 0$. Experimental limitations can make it difficult to apply a triexponential fit to $r(t)$ to recover the inertial time constant. Tan et al. recover the inertial component by calculating a corrected order parameter T^2 :

$$T^2 = [2.5 * (A_1 + A_2)] \quad 1.14$$

An additional order parameter T^2S^2 is obtained as follows:

$$T^2S^2 = [2.5 * A_2] \quad 1.15$$

T^2S^2 is equivalent to the previously mentioned Q^2 . The maximum angle sampled by the inertial motions of the wobbling probe is then calculated by taking:

$$T^2 = \left[\frac{1}{2} (\cos \theta_{in})(1 + \cos \theta_{in}) \right]^2 \quad 1.16$$

Equation 1.16 yields θ_{in} and a similar process can be used to obtain the total range of angles explored by both the wobbling probe and the slowly diffusing cone:

$$T^2S^2 = \left[\frac{1}{2} (\cos \theta_{tot})(1 + \cos \theta_{tot}) \right]^2 \quad 1.17$$

This angle we refer to as θ_{tot} and the effective cone angle is computed from performing the same calculations with S^2 . We compute S^2 via the following:

$$S^2 = \frac{A_2}{(A_1 + A_2)} \quad 1.18$$

Then, θ_{eff} is solved by computing:

$$S^2 = \left[\frac{1}{2} (\cos \theta_{eff})(1 + \cos \theta_{eff}) \right]^2 \quad 1.19$$

θ_{eff} captures the faster, localized reorientational relaxation motions experienced by the probe. It is used in conjunction with τ_c to compute the cone diffusion constant D_c .³³

$$D_c = \frac{x_c^2 * (1 + x_c)^2 \{ \ln[(1 + x_c)/2] + (1 - x_c)/2 \}}{\tau_c(1 - Q^2)[2(x_c - 1)]} + \frac{(1 - x_c)(6 + 8x_c - x_c^2 - 12x_c^3 - 7x_c^4)}{24\tau_c(1 - Q^2)} \quad 1.20$$

Where x_c equals $\cos \theta_{eff}$ and Q^2 equals the same aforementioned ($2.5 * A_2$) value. Taking the reciprocal of equation yields D_c^{-1} , the inverse wobbling-in-a-cone diffusion constant. D_c^{-1} describes how long it takes the dipole to explore the range of configurations for the localized cone. D_m^{-1} , the inverse overall orientational diffusion constant, is calculated by taking:

$$D_m^{-1} = 6\tau_m \quad 1.21$$

In which τ_m is the slow time constant extracted from the biexponential fit of $r(t)$. D_m^{-1} describes the time it takes the probe to explore the entire possible range of orientations in the cone, while the cone itself simultaneously diffuses due to motions of the surroundings.

To summarize, after performing the wobbling in a cone analysis we obtain time constants describing how long it takes the probe to explore the cone of angles, the time required for cone itself to diffuse, and the angular ranges associated with these motions. In conjunction with 2D-IR, this analysis provides a molecular-scale view of the dynamics experienced by the vibrational probes and the surroundings.

2. Linear versus Nonlinear Infrared Spectroscopy

2.1 Limitations of Linear Spectroscopy

Linear spectroscopic methods such as FTIR readily determine the frequency of vibrational modes in a sample as well as FWHM (full width half max) values for their respective peaks. However, a substantial amount of rich dynamic information resides underneath the time and ensemble-averaged peaks obtained by methods such as FTIR.

In the presence of a single subensemble, the line shape takes on a Lorentzian profile (Figure 2.1a) whose FWHM is due to homogeneous processes. Inhomogeneities in the sample may give rise to subensembles with varying vibrational frequencies due to the VSE (Figure 2.1b), though each subensemble still its own distinct homogeneous linewidth. The width ascribed to the FTIR peak due to these different subensembles is called static inhomogeneity. However, molecular systems are rarely static in time.³ For some oscillating vibrational mode within an ensemble of molecules, the frequency of that vibration is sensitive to changes imposed by the environment. Motions of solute and solvent alike could also force the vibrational probes to sample different subensembles, a process called spectral diffusion (Figure 2.1 c). Fitting the FTIR line shape to a pseudo-Voigt can approximate the extent of homogeneous versus inhomogeneous dynamics for a sample⁴⁰⁻⁴² but such methods cannot determine the rate of spectral diffusion. 2D-IR is able to recover such information from a system. The details of how this occurs will be discussed at the end of

this chapter, after a discussion on the differences between homogeneous and inhomogeneous dynamics as well as the origin of 2D-IR signal.

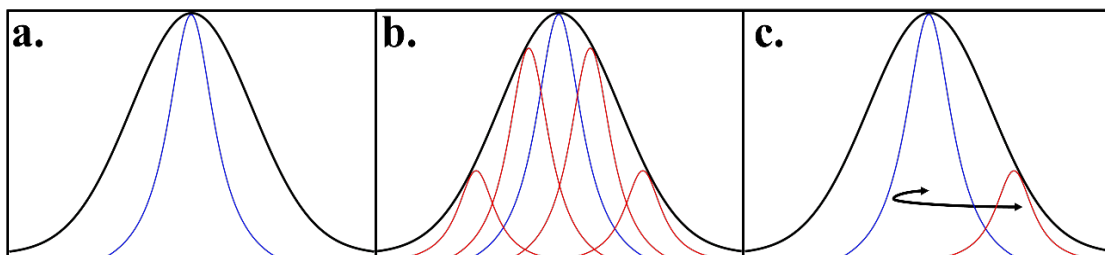


Figure 2.1. Panels a-c show an FTIR peak (black line) with a Gaussian profile. Panel (a) shows a single subensemble of oscillators and their homogeneous linewidth with a Lorentzian profile. In (b) additional subensembles are drawn in red, each with their own homogeneous linewidth which contribute to static inhomogeneity. Panel (c) portrays the process of spectral diffusion in which a probe may move among subensembles over time.

Homogeneous broadening arises from motions intrinsic to the vibrational probe, though the surroundings can affect the time scales on which homogeneous processes occur. This includes vibrational relaxation, molecular reorientation, and dephasing.⁴³ The full expression for the homogeneous contribution to the linewidth (Γ) is as follows:

$$\Gamma = \frac{1}{\pi T_2} = \frac{1}{\pi T_2^*} + \frac{1}{2\pi T_1} + \frac{1}{3\pi T_{or}} \quad 2.1$$

Herein T_2 refers to the total dephasing time. Pure phase relaxation (T_2^*), population relaxation (T_1), and orientational relaxation (T_{or}) combine to yield the total dephasing time. T_2^* represents pure dephasing, caused solely by fluctuations of either the probe or the surroundings that then perturb the frequency of the oscillator. If enough of these fluctuations are combined, they contribute to a decay in the macroscopic polarization. T_1 population decay refers to the amount of time it takes an oscillator to relax after vibrational excitation. T_1 can take on a wide range of values depending on the system of study, especially if the surroundings have a large number of vibrational modes that can accept

energy. Alternatively, bonds adjacent to the excited mode may also accept vibrational excitation.⁴⁴ T_l values are typically obtained by running a pump probe experiment. The details will not be discussed within but are addressed by Wynne et al.⁴⁵ Orientational relaxation (T_{or}) refers to how long it takes the dipole to randomize its orientation in space, and is often a small contribution to the homogeneous linewidth when considering a bulky molecule.³⁸

In contrast to homogeneous broadening, inhomogeneous broadening captures the distribution of environments in a sample, each of which may experience fluctuations differently. One example of this behavior is Doppler broadening. For a set of ideal gaseous molecules that follow a Boltzmann distribution, their Maxwell velocity distribution is given by the following:

$$f(v_x, v_y, v_z) = \frac{M^{3/2}}{2\pi k_b T} \exp\left(-\frac{M}{2k_b T}(v_x^2, v_y^2, v_z^2)\right) \quad 2.2$$

where M is the atomic mass of the atom, k_b is the Boltzmann constant, and $f(v_x, v_y, v_z)$ represents the fraction of the sample that has velocities within some range $v_x, v_x + dv_x$ along each coordinate axis in Cartesian space.⁴³ The amount of Doppler shift exhibited by each molecule follows a distribution as a direct result of the Maxwell velocity distribution. Inhomogeneous broadening may also arise from localized defects in a crystal structure, or the range of frequencies an oscillator could experience depending on the arrangement of molecules in the solvation shell. In other words, a non-uniform sample contains non-uniform electric fields that interact with subsets of the sample and cause changes in vibrational energy levels.¹⁴

By understanding the interplay between homogeneous and inhomogeneous dynamics, the behavior of a vibrational probe can be better quantified and compared to other systems via 2D-IR. While 2D-IR by itself cannot explicitly describe the molecular motions that give rise to spectral diffusion, 2D-IR can better inform MD simulations of what types of processes occur on the femtosecond and picosecond time scales.⁴⁶ The underlying theory that describes the origin of FTIR and 2D-IR signal will now be discussed.

2.2 Linear Spectroscopy

When light interacts with a sample, a macroscopic polarization is prepared. After the light source is turned off, the macroscopic polarization evolves over time in accordance with the response function of the sample. If the incident light pulses are infinitely short in time with envelopes resembling delta functions, the macroscopic polarization equals the molecular response at all times.³ Such conditions do not hold true in a laboratory setting due to the finite width of the applied external field. Therefore, the macroscopic polarization $P^{(1)}(t)$ for a sample is the convolution of the electric field with the response function:

$$P^{(1)}(t) = \int_0^{\infty} dt_1 E'(t - t_1)R^{(1)}(t_1) \quad 2.3$$

where $R^{(1)}(t_1)$ is the first order response at a specific time t_1 after light interacts with the sample. The electric field of the single pulse is indicated by $E'(t - t_1)$, where E' indicates the electric field. E' can be expanded to yield a term that has both positive and negative frequencies in the form of $E(t) \propto e^{-i\omega_{01}t}$ and $E^*(t) \propto e^{+i\omega_{01}t}$. The equation given above for the first order macroscopic polarization is only valid for single pulse experiments. When the theory outlined within is extended to methods using three incident pulses like

2D-IR spectroscopy, the convolution integral must instead account for three pulses and must be integrated over three distinct times to obtain a third order macroscopic polarization. To better understand what molecular processes constitute the response functions and collectively form the macroscopic polarization, it is helpful to take a small detour into quantum mechanics.

In the absence of a laser pulse, the eigenstates of some molecular system are obtained by solving the time independent Schrödinger equation:

$$\hat{H}_0|n\rangle = E_0|n\rangle \quad 2.4$$

Where \hat{H}_0 is the time independent Hamiltonian and E_0 is the energy associated with some eigenstate $|n\rangle$. When a laser pulse interacts with the sample, the perturbation can be accounted for by re-writing the total Hamiltonian as:

$$\hat{H} = \hat{H}_0 + \hat{W}(t) \quad 2.5$$

in which $\hat{W}(t)$ represents the interaction energy between the sample and the incident radiation. The unperturbed Hamiltonian \hat{H}_0 lacks time dependence. The interaction energy of the pulse with a molecule, $\hat{W}(t)$, is related to both the strength of the incident field and the transition dipole $\hat{\mu}$. The transition dipole operator will be discussed in more detail shortly. Because the incident field inevitably oscillates with time, the interaction energy is expressed as:

$$\hat{W}(t) = -\hat{\mu}E(t) \quad 2.6$$

In matrix form, the dipole operator may also be expressed as:

$$\mu = \begin{pmatrix} 0 & \mu_{01} \\ \mu_{01} & 0 \end{pmatrix} \quad 2.7$$

The transition dipole moment is then defined as the following:

$$\langle n|\hat{\mu}|m\rangle = \frac{d\mu}{dx} \langle n|\hat{x}|m\rangle \quad 2.8$$

Over the course of vibrational excitation, x describes displacement of the bond's nuclear coordinates relative to the equilibrium position. The $d\mu/dx$ term reflects the change in the bond's static dipole as a function of displacement. In a more classical sense, $d\mu/dx$ reflects change in the bond's dipole as the bond is contorted in the form of stretching or compressing. The $d\mu/dx$ coefficient is what gives rise to the intensity of a vibrational mode, whereas the $\langle n|\hat{x}|m\rangle$ term gives rise to selection rules of $\Delta v = \pm 1$.

To reiterate, the dipole operator (equation 2.7) describes how strongly light interacts with a sample. The equations thus far fail to explain how the molecules will evolve over time once the light source is shut off. Oftentimes, it is helpful to describe light interacting with an ensemble of molecules by utilizing a density matrix representation. For a system where only the ground and first vibrational states are accessible, the density matrix will include four terms:

$$\rho = \begin{pmatrix} \rho_{00} & \rho_{01} \\ \rho_{10} & \rho_{11} \end{pmatrix} = \begin{pmatrix} \langle c_0(-\infty)c_0^*(-\infty) \rangle & -i\langle c_0(-\infty)c_1^*(-\infty) \rangle \\ i\langle c_1(-\infty)c_0^*(-\infty) \rangle & \langle c_1(-\infty)c_1^*(-\infty) \rangle \end{pmatrix} \quad 2.9$$

The weighting coefficients c_0 and c_1 describe the likelihood that a molecule is in a given state, where c_0^2 would give the probability the vibration is in the ground state, and c_1^2 describes the probability it is in the excited vibrational state. The complex conjugate of some coefficient c_n is given by c_n^* . The time dependence of the coefficients will be solved

for shortly, but right now the matrix is written with respect to $t = -\infty$ to indicate the molecules have not yet interacted with light. If explicit values were written in each of the indices, all entries would equal zero except ρ_{00} , which would equal 1. More generally, the ensemble density matrix normalized with terms p_s can be algebraically expressed as:

$$\rho_{nm} = \sum_s p_s c_m^{s*} c_n^s = \langle c_m^{s*} c_n^s \rangle \quad 2.10$$

Both representations of the matrix above describe a sample that has not been perturbed. Describing how the terms of either 2.9 or 2.10 change over time requires use of time dependent perturbation theory. The time dependent Schrödinger equation relates the time-varying behavior of the wave function to the total Hamiltonian:

$$i\hbar \frac{\partial}{\partial t} |\Psi\rangle = \hat{H} |\Psi\rangle \quad 2.11$$

The wavefunction $|\Psi\rangle$ can be expanded into an eigenket basis by writing the following:

$$i\hbar \frac{\partial}{\partial t} \sum_n c_n e^{-\frac{iE_n t}{\hbar}} |n\rangle = \hat{H} \sum_n c_n e^{-\frac{iE_n t}{\hbar}} |n\rangle \quad 2.12$$

c_n is the aforementioned weighting constant associated with eigenket $|n\rangle$, and E_n is the energy associated with that eigenket.

In the presence of a time-varying perturbative force like incident radiation, the weighting coefficients themselves become time dependent. For some two-level system with weighting coefficient c_0 for the ground state $|0\rangle$ and c_1 for the excited state $|1\rangle$, the

following coupled equations result after solving for the time dependence of the weighting coefficients:

$$\frac{\partial}{\partial t} c_1(t) = +\frac{i}{\hbar} c_0(t) e^{-i\omega_{01}t} \langle 1 | \hat{\mu} | 0 \rangle E(t) \quad 2.13$$

$$\frac{\partial}{\partial t} c_0(t) = +\frac{i}{\hbar} c_1(t) e^{+i\omega_{01}t} \langle 0 | \hat{\mu} | 1 \rangle E(t) \quad 2.14$$

To solve for the time dependence of the density matrix terms where $\rho_{nm} = c_m^* c_n$ and $\rho = \sum_{n,m} c_n c_m^* |n\rangle \langle m|$, a bit of substitution and algebra reveals the Liouville-von Neumann equation:

$$\frac{d\rho}{dt} = -\frac{i}{\hbar} [\hat{H}, \rho] \quad 2.15$$

The time dependence of the density matrix is equivalent to the commutator of the total Hamiltonian with the density matrix, $[\hat{H}, \rho]$, multiplied by a coefficient. A similar result can be calculated for each antidiagonal index of the ensemble density matrix:

$$\frac{d\rho_{nm}}{dt} = \sum_s \frac{dp_s}{dt} c_n^{s*} c_m^s - \frac{i}{\hbar} [\hat{H}, \rho_{nm}] \quad 2.16$$

The $\frac{dp_s}{dt}$ term accounts for the fact that the normalization constants of an ensemble must change if population relaxation causes molecules in the first excited vibrational state to decay to the ground state, or if homogeneous dephasing occurs. It is essentially a correction factor added on to the Liouville-von Neumann equation. In its current form, equation 2.16 does not explicitly connect experimentally measured values to the time dependence of the density matrix. However, expressing the matrix indices in terms of dephasing and

population decay time constants will make the connection between experiment and theory much clearer.

To reiterate, the total Hamiltonian of an ensemble undergoing perturbation in the form of a laser pulse is expressed as $\hat{H} = \hat{H}_0 + \hat{W}(t)$. By expanding the total Hamiltonian into the system Hamiltonian and the interaction energy, equation 2.16 can be re-written as:

$$\frac{d\rho_{nm}}{dt} = -\frac{i}{\hbar} [\hat{H}_0, \rho]_{nm} - i \frac{i}{\hbar} [\hat{W}, \rho]_{nm} - \frac{\rho_{nm}}{T_2} \quad 2.17$$

The equation above will describe how a single element of the ensemble density matrix changes over time in response to an incident field. T_2 is the same homogeneous dephasing time mentioned previously. However, the goal of these mathematics is to ultimately use the molecular response functions to obtain the first order macroscopic polarization. To work toward that result, it is helpful to calculate the first order change in indices of the ensemble density matrix through perturbation theory:

$$\begin{aligned} \rho_{nm}^{(1)}(t) = \frac{i}{\hbar} (\rho_{mm}^{(0)} - \rho_{nn}^{(0)}) \mu_{nm} \left\{ e^{-i\omega t} \int_0^\infty E'(t-t_1) e^{-\frac{t_1}{T_2}} e^{-2i\omega t_1} dt_1 \dots \right. \\ \left. + e^{+i\omega t} \int_0^\infty E'(t-t_1) e^{-\frac{t_1}{T_2}} dt_1 \right\} \quad 2.18 \end{aligned}$$

where $\rho_{nm}^{(1)}(t)$ is the first order response of one of the off diagonal terms for the ensemble density matrix. The details of performing the calculation will not be discussed, but an identical process is used for calculating the third order changes in the density matrix indices.³ The third order changes will be needed later to obtain the third order macroscopic polarization. Assuming the ensemble density matrix is Hermitian, $\rho_{mn}^{(1)}(t)$ can be found by

taking the complex conjugate of $\rho_{nm}^{(1)}(t)$.

The first order response of the on diagonal terms associated with eigenstate probabilities in equation (19) have been ignored for good reason. The emitted signal is equal to the phase-shifted macroscopic polarization, and the emitted signal at some time t is calculated by taking the expectation value of the transition dipole:

$$E_{sig}^{(1)}(t) = \langle \mu(t) \rangle = Tr(\rho^{(1)}(t)\mu) \quad 2.19$$

As shown above, the expectation value of the transition dipole is equivalent to the trace of $\rho^{(1)}(t)\mu$, where the trace of some matrix C is defined as: $Tr(C) = \sum_n C_{nn}$. The transition dipole is an antidiagonal operator. After taking the product of the transition dipole with $\rho^{(1)}(t)$, the previously off diagonal terms will now lay on the diagonal. They are then summed up to give the emitted signal. The emitted signal is related to the macroscopic polarization and the first order molecular response function via the following equation which has been previously shown:

$$E_{sig}^{(1)}(t) = iP^{(1)}(t) = i \int_0^\infty dt_1 E'(t - t_1)R^{(1)}(t_1) \quad 2.20$$

Where $R^{(1)}$ is the first order molecular response function and E' is the complete electric field. The first order molecular response function included in the math above can be more directly expressed as the following:

$$R^1(t_1) \propto i \langle \mu(t_1)[\mu(0), \rho(-\infty)] \rangle \quad 2.21$$

We will now describe how to extend this formalism to multi-pulse experiments, such as 2D-IR.

2.3 The Extension to Third Order Techniques, Including 2D-IR

By using iterative substitutions with time dependent perturbation theory as briefly mentioned previously, the third-order nonlinear macroscopic polarization can be expressed as:

$$P^{(3)} \propto \int_0^\infty dt_3 \int_0^\infty dt_2 \int_0^\infty dt_1 E_3(t-t_3) E_2(t-t_2) E_1(t-t_3-t_2 - t_1) R^{(3)}(t_3, t_2, t_1) \quad 2.22$$

The third order nonlinear response function is then written as the following:

$$R^{(3)}(t_3, t_2, t_1) \propto -i \langle \mu(t_3 + t_2 + t_1) [\mu(t_2 + t_1) [\mu(t_1) [\mu(0), \rho(-\infty)]]] \rangle \quad 2.23$$

The third order response function features three nested commutators, representing the three pulses of light that will interact with the sample. The final $\mu(t_3 + t_2 + t_1)$ term represents the final process measured which is light leaving the sample in the form of an emitted signal at time $t_3 + t_2 + t_1$. The details of deriving this equation have been excluded for brevity but can be found in many texts.^{3,47} By expanding the nested commutator in equation (22), twelve terms result which represent different energetic pathways the sample could undergo in response to the three pulses of light.

In the expansion below, $R^{(3)}$ is the third order response function and index R_n represents a distinct energy pathway. R_n^* represents the complex conjugate of R_n . The incident electric field that will interact with the sample, $E'(t)$, can be expanded into its two terms $E'(t) = E(t) + E^*(t)$. In this expanded form $E(t) \propto e^{-i\omega t}$ and $E^*(t) \propto e^{+i\omega t}$, and these two terms of the electric field can act upon either the bra or the ket of a state. Therefore, each pulse can induce four different interactions. The three incident pulses will

cause the response function to have a total of twelve different terms. Summing together the twelve R_n terms yields the third order molecular response function. In the expansion below, pathways R_3 and R_6 along with their complex conjugate analogues have been omitted. Their energetic pathways access the second excited vibrational state $|2\rangle$, and are not the focus of this discussion because the 1-2 dynamics sometimes differ from the 0-1 dynamics. The 1-2 transition is readily observed via 2D-IR spectroscopy nonetheless. The expansion excluding terms accessing $|2\rangle$ that yields a total of eight terms is as follows:

$$\begin{aligned}
R^{(3)}(t_3, t_2, t_1) \propto & -i \langle \hat{\mu}(t_3 + t_2 + t_1) [\hat{\mu}(t_2 + t_1) [\hat{\mu}(t_1) [\hat{\mu}(0), \rho(-\infty)]]] \rangle = \dots \\
& i \langle \mu_3 \mu_1 \rho(-\infty) \mu_0 \mu_2 \rangle - i \langle \mu_2 \mu_0 \rho(-\infty) \mu_1 \mu_3 \rangle \quad (R_1 + R_1^*) \\
& i \langle \mu_3 \mu_2 \rho(-\infty) \mu_0 \mu_1 \rangle - i \langle \mu_1 \mu_0 \rho(-\infty) \mu_2 \mu_3 \rangle \quad (R_2 + R_2^*) \\
& i \langle \mu_3 \mu_0 \rho(-\infty) \mu_1 \mu_2 \rangle - i \langle \mu_2 \mu_1 \rho(-\infty) \mu_0 \mu_3 \rangle \quad (R_4 + R_4^*) \\
& i \langle \mu_3 \mu_2 \mu_1 \mu_0 \rho(-\infty) \rangle - i \langle \rho(-\infty) \mu_0 \mu_1 \mu_2 \mu_3 \rangle \quad (R_5 + R_5^*) \quad 2.24
\end{aligned}$$

Visualizing the differences between the energetic pathways above and the difference between the R_1, R_1^* terms becomes much easier by making use of two sided Feynman diagrams.

2.4 Two Sided Feynman Diagrams: A Tool for Understanding Pulse Sequences

Feynman diagrams are meant to serve as a pictorial way of describing the different interactions an incident light field will have with a system. An example is shown in Figure 3. The solid line with an arrow on the far left represents the time axis, and the upward

direction represents increased time elapsed. The labeled tick marks indicate the most important times at which evolution of the molecular system occurs.

Two solid vertical lines lacking arrowheads are drawn to represent the system boundary, and the system evolves over time as the lines proceed upward. At all times, the sample's ket is drawn on the left and the bra is drawn on the right. Keeping in mind that for some eigenstate $|0\rangle$ the complex conjugate is given by $\langle 0|$, the Feynman diagram for some energetic pathway R_n will be the mirror image of R_n^* and vice versa. To be succinct, only the R_n pathways will be shown.

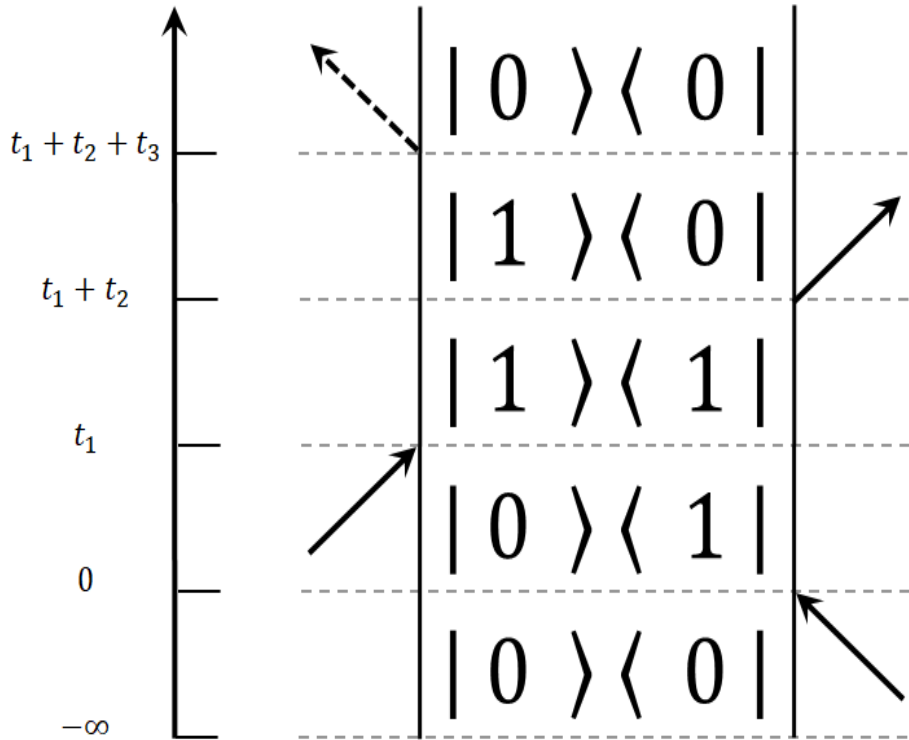


Figure 2.2. A Feynman diagram depicting the time evolution of the two state system in according to the R_1 energetic pathway. Light interacting with the sample is indicated by solid arrows, whereas a dotted arrow indicates signal emitted by the sample.

A solid arrow represents an incident light pulse that interacted with the system, whereas a dotted arrow represents signal emitted by the system. Light that interacts with a ket is represented by a solid arrow facing the right and has frequency $E(t) \propto e^{-i\omega_{01}t}$, where ω_{01}

is the energy gap between the ground and first vibrational excited state. Conversely, light that interacts with a bra is expressed with an arrow pointing to the left and has frequency $E^*(t) \propto e^{+i\omega_{01}t}$.

Regardless of the energetic pathway being described by the Feynman diagram, at time $t = -\infty$ the sample is assumed to be almost exclusively in the ground state as predicted by the Boltzmann distribution. The sample has not yet interacted with light. In the case of Figure 3, an electric field with frequency $e^{+i\omega_{01}t}$ has interacted with the bra and at $t = 0$ the interaction is complete. Between 0 and t_1 another pulse but now with frequency $e^{-i\omega_{01}t}$ arrives and excites the ket. At time $t = t_1$, this interaction is complete. Both the bra and ket are now in the excited vibrational state.

Between t_1 and $t_1 + t_2$, a third pulse arrives at the sample with frequency $e^{+i\omega_{01}t}$ and interacts with the bra. The bra is still in an excited state, therefore the incident radiation forces the bra to undergo stimulated emission and the bra ends in the $\langle 0|$ state at $t = t_1 + t_2$. At time $t = t_1 + t_2 + t_3$, the same emits vibrational echo signal. One distinct advantage of Feynman diagrams is that the systems in population and coherence states at some time t can be quickly distinguished from each other. Where the ket on the left hand side could be described by some eigenstate $|n\rangle$ and the bra on the right hand side by $\langle m|$, so long as $n = m$ the system is in a population state, and if $n \neq m$ the system is in a coherence state.^{3,}

⁴⁸ The distinction of whether the system is in a population state or a coherence will determine which line broadening phenomena occur at that point in time.

2.5 Rephasing and Non-Rephasing Pulse Sequences

Shown below are the Feynman diagrams for pathways R_1, R_2, R_4 and R_5 (Figure 2.3). Although there are dotted lines drawn in all four diagrams indicative of emitted signal, only two of the diagrams produce photon echo through a rephasing pulse sequence: This includes pathways R_1 and R_2 . R_4 and R_5 are associated with a non-rephasing pulse sequence.

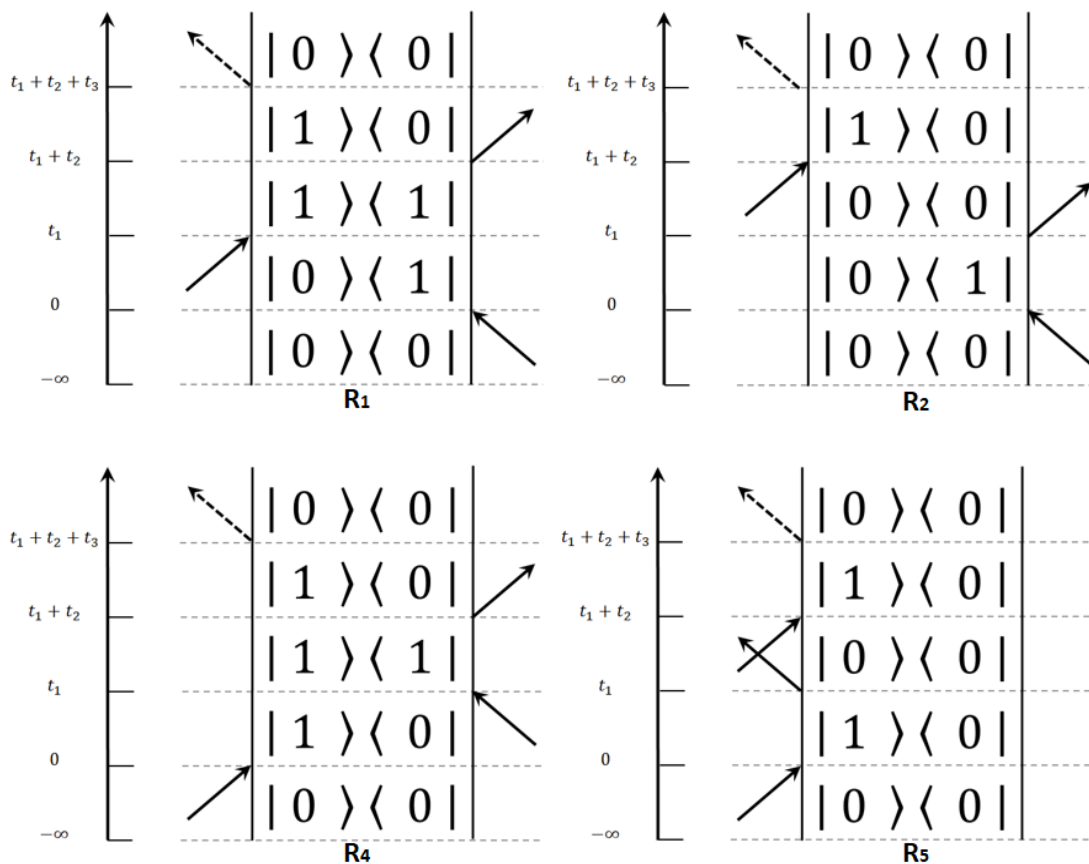


Figure 2.3. Feynman diagrams showing four different energetic pathways that lead to separate terms in the third order molecular response function. R_1 and R_2 are rephasing pathways, whereas R_4 and R_5 are non-rephasing pathways. Details regarding their interpretation can be found in the text.

To more clearly specify the differences between rephasing and non-rephasing pulse sequences, the system can be analogously described as a 2x2 density matrix as follows:

$$\rho = \begin{pmatrix} \rho_{00} & \rho_{01} \\ \rho_{10} & \rho_{11} \end{pmatrix} \quad 2.25$$

For the density matrix shown above, the diagonal terms ρ_{00} and ρ_{11} represent populations of the ground and excited states respectively. After the first interaction with light, which is mathematically equivalent to multiplying the density matrix with the dipole operator matrix, an off-diagonal term results for the ρ_{01} index. This is identical to the R₁ Feynman diagram pictured above possessing a non-zero term for the bra at $t = 0$. The non-zero oscillatory term for ρ_{01} is called a (01) coherence. If the nonzero off diagonal term were to occur for ρ_{10} instead, the term would be called a (10) coherence. The coherence established in either ρ_{01} or ρ_{10} then oscillates with frequency ω_{01} corresponding to the energy gap between the $|0\rangle$ and $|1\rangle$ vibrational states. Quantum mechanically speaking, the system is in a linear superposition of the $|0\rangle$ and $|1\rangle$ eigenkets which causes this oscillation to occur. As the coherence oscillates, the individual oscillators' frequencies will slightly change due to varying amounts of VSE in the sample. In other words, dephasing due to both homogeneous and inhomogeneous processes occurs.^{3, 48}

At $t = t_1$ when the sample has interacted with another laser pulse of light, the antidiagonal terms are reset to zero and the non-zero entries of the density matrix now persist along the diagonal. In terms of the Feynman description, at $t = t_1$ the bra and the ket have identical values. Both of these results indicate the system is now in a population state. In contrast to the $\pi/2$ pulses used in nuclear magnetic resonance, infrared pulses are not strong enough to create sufficient excited state population.³ Therefore, even in a

population state, c_0 will be approximately 1. In the population state, homogeneous dephasing still occurs because oscillators can relax from the excited vibrational state to the ground vibrational state. The population decay forcibly removes an oscillator's phase relationship with nearby excited oscillators.

At $t = t_1 + t_2$, the third and final pulse interacts with the sample. Multiplying the density matrix with the dipole operator a third time results in zeroes along the diagonal and non-zero terms along the antidiagonal. In the Feynman picture, the bra and the ket contain dissimilar values once more. Similar to the system at $t = 0$, the molecules are in a coherence state and oscillate with frequency ω_{01} . However, R_1 is a rephasing pathway. In the Feynman diagram for R_4 , the initial and final coherence states are identical. Similarly, if a density matrix formalism were used to describe the time evolution of the system for R_4 , the coherence exists exclusively in ρ_{10} .

The process of changing among the phase-conjugate coherences is required for rephasing to eventually occur after the light interaction at t_3 . Pulse sequences such as those pictured in R_1 form the phase-conjugate coherence at t_3 . This allows the oscillators to evolve in a trajectory opposite of how they propagated during the population state. Therefore, the oscillators regain their phase relationships that were previously present during the first coherence period. A signal is emitted at $t = t_1 + t_2 + t_3$ regardless of whether the pulse sequence used was rephasing or non-rephasing. However, the signal obtained from a non-rephasing pulse sequence will exhibit inhomogeneous dephasing that is removed from the rephasing signal.

2.6 Femtosecond Pulsed Laser Instrumentation

In a pre-built system (SpectraPhysics, Millennia), a 40 W diode laser bar pumps a neodymium-doped yttrium orthovanadate crystal to generate 1064 nm continuous wave (CW) output. The output is then frequency doubled in a lithium triborate crystal, producing 532 nm light. The conversion process generates an output of roughly 5 W⁴⁹ that proceeds to pump a titanium sapphire rod (Ti:Sapph) in a passively modelocked oscillator (Kapteyn-Murnane Laboratories, Model MTS). The resultant pulses are centered at 800 nm with a full width half max (FWHM) of 50 nm⁴⁹ and a power of approximately 250 mW. These pulses serve as the seed pulses for the regenerative amplifier (SpectraPhysics Spitfire). The regenerative amplifier consists of a beam stretcher, an amplification cavity, and a compressor.

In the beam stretcher, the seed pulses reflect off a diffraction grating multiple times. The lower energy components of the light are diffracted by a smaller angle than the higher energy frequencies. By properly angling both the dispersive and reflective optics in the beam stretcher, the beam path is manipulated so that higher frequencies travel a greater pathlength than lower frequencies, and the lower frequencies arrive at the amplifier cavity first. In other words, the seed pulse has been intentionally chirped. Stretching the pulse in time ensures that the pulse power can be safely increased in the amplification cavity without damage to optics.⁵⁰

To create the pump pulses for the amplification cavity, a diode laser excites a neodymium-doped yttrium lithium fluoride crystal. The resultant Q-switched pulses are centered at 527 nm and have a repetition rate of 1 kHz (SpectraPhysics Empower). The

527 nm pump pulse and 800 nm seed pulse are then both aligned onto a Ti:Sapph rod in the amplification cavity.

The amplified pulses then pass through a compressor which shortens the pulse duration with diffraction gratings in a manner similar to what is used for the pulse stretcher. The final compressed output power is 1 W of 800 nm light with a pulse duration of 40 fs.² Each pulse contains ~1 mJ of power and the pulse train has a repetition rate of 1kHz.⁵¹ Approximately 500 mW of the 1 W output is aligned into an optical parametric amplifier (OPA, SpectraPhysics), and the other 500 mW are directed toward the opposite side of the laser table for a separate experiment.

The 500 mW directed toward the OPA is then split into three beam paths of varying strength. One of the beam paths is directed into a sapphire crystal to generate white light. The white light is then overlapped with the other two beam paths on a 3 mm thick β -barium borate crystal to generate near-IR signal and idler beams. The signal and idler beams are then difference frequency mixed in a 0.5 mm silver gallium sulfide crystal, generating 3-4 μ J mid-IR pulses that have a pulse duration of approximately 90 fs and a bandwidth of approximately 200 cm^{-1} at the full width half max (FWHM).⁵²

2.7 2D-IR Instrumentation

The mid-IR beam mentioned in section 2.6 is then passed through three 5 mm beam splitters angled at 45° to create a total of four beams used for 2D-IR data acquisition, the weakest of which is used as the local oscillator (LO). The three p-polarized pulses are focused with an off-axis parabolic reflector onto the sample in the BOXCARS geometry.⁵³ A carbon tetrachloride sample with a 50 μ m pathlength was used to maximize nonresonant

third-order signal by temporally and spatially overlapping the three beams at their focal point onto the sample. The vibrational echo was emitted in the phase-matched direction and coaligned with an LO into a 0.32 m monochromator with a 75 line/mm grating. The heterodyned signal was detected with a liquid N₂ cooled 64-element mercury cadmium telluride (MCT) linear array detector (Infrared Associates, Inc.). Spectra were collected by varying the delay between pulses 1 and 2, and 2 and 3 then Fourier transforming the heterodyned signal in order to build up the ω_τ and ω_m axes mentioned below.

2.8 2D-IR Processing & Analysis

An example 2D-IR spectrum is shown in Figure 2.4. A typical 2D-IR spectrum possesses two frequency axes, ω_τ and ω_m . ω_τ runs along the horizontal axis whereas ω_m runs along the vertical axis. For ease of understanding, ω_τ is also sometimes called ω_{pump} and ω_m is called ω_{probe} . Alternatively, data may also have the axes labeled ω_1 for ω_τ and ω_3 for ω_m . The presence of two contours, one sitting on top of and one sitting below the diagonal (Figure 2.4) is commonly observed in 2D-IR spectroscopy. For a system with three vibrational levels given by $|0\rangle$, $|1\rangle$, and $|2\rangle$, peaks shown on or above the diagonal are colored red to represent positive response in the form of ground state bleach and stimulated emission occurring from the 0-1 transition. The peak colored blue below the diagonal represents negative response in the form of excited state absorption and corresponds with the 1-2 transition. In the case of Figure 2.4, the 0-1 and 1-2 contours appear to be spaced approximately 80 cm⁻¹ apart along the ω_m axis. This distance between the 0-1 and 1-2 corresponds with the anharmonicity of the vibrational mode, and is the anharmonicity of the Si-H stretch in the case of Figure 2.4. Discussion regarding off

diagonal peaks and chemical exchange can be readily found in the literature³ and are briefly discussed in Chapters 4 and 5.

In Figure 2.4 the 0-1 and 1-2 peaks at $T_w = 0.5$ ps lack the roundness of the peaks at $T_w = 5$ ps. Herein T_w refers to the delay between pulses 2 and 3 as discussed during Feynman diagrams. The change in peak shape from diagonally elongated to uniformly round is a result of spectral diffusion. At early $T_w = 0.5$ ps, the peak is elongated along the diagonal because the ensembles of oscillators have not yet fully sampled the full range of solvation environments.

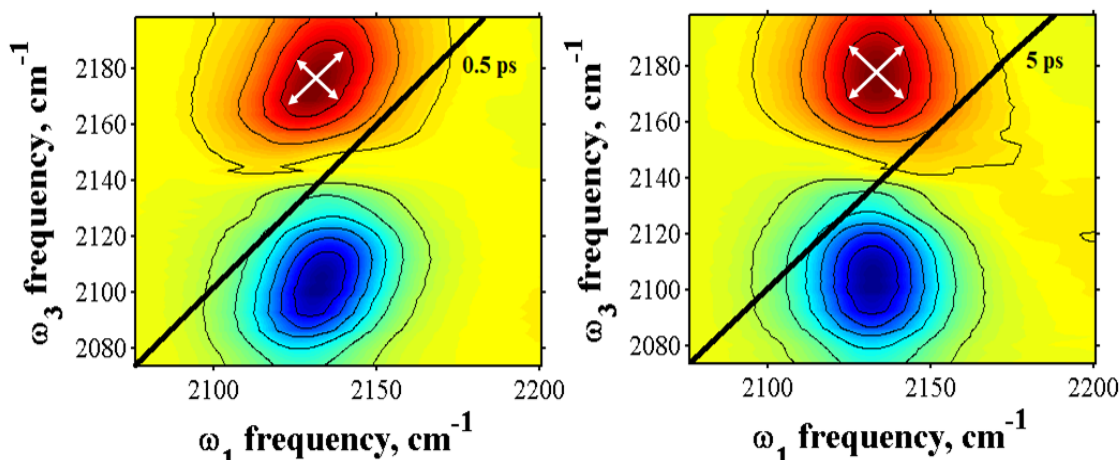


Figure 2.4 Two example 2D-IR spectra of TriPS in chloroform at an early T_w (0.5 ps) on the left and a later T_w (5 ps) on the right. White arrows are drawn to emphasize the pronounced diagonal elongation at early T_w s.

Properties about a system's molecular dynamics can be obtained from 2D-IR by quantifying the time scales over which spectral diffusion occurs. This is done by finding the center line slope (CLS). The CLS is a value that ranges from 0-1 and describes the extent to which a peak is elongated along the diagonal as a function of T_w . A value of 0 for the CLS indicates a peak that has undergone spectral diffusion and adequately sampled the full range of environment configurations. Alternatively, a value of 1 for the CLS indicates

a peak that is still highly correlated and the frequencies have not significantly evolved over time.

To obtain a value for the CLS of a given peak, the 2D-IR spectrum of a certain T_w is cut into slices running parallel to the ω_3 / ω_m axis and a Gaussian curve is fit the point of maximum signal intensity along the slice. A line is then drawn connecting the maxima of the Gaussians and the slope of the line is obtained. The CLS is then plotted as a function of T_w and fit to a decaying exponential. CLS analysis is a popular tool for 2D-IR spectroscopy for a few reasons: Apodizing data does not interfere with obtaining the correct value for the CLS because it depends on the slope instead of a line shape. Secondly, the CLS is proportional to the normalized frequency frequency correlation function (FFCF).^{3,}

^{48, 54} The normalized FFCF is related to the CLS decay and can be expressed as:

$$CLS(T_w) = \sum_i \Delta_i^2 e^{-\frac{t}{\tau_i}} \quad 2.26$$

Where Δ_i^2 is the frequency fluctuation amplitude associated with some inhomogeneous motion i , and τ_i is the time scale over which motion i occurs. Δ_i^2 and τ_i have their i subscripts because there are instances in which the CLS may appear to decay as a multiexponential instead of a single exponential. The τ_i time constants from the CLS decays have been shown to be highly accurate^{48, 55} for obtaining the FFCF, which is expressed as the following:

$$C(t) = \frac{\delta(t)}{T_2} + \sum_i \Delta_i^2 e^{-t/\tau_i} \quad 2.27$$

Where T_2 is the total homogeneous dephasing time mentioned before and the τ_i values are kept identical when switching from equation 2.26 to 2.27. The amplitude from the CLS

decay fits and the linear FTIR FWHM are used approximate Δ and T_2 of the full FFCF (2.27) by following the procedure of Kwak and co-workers.^{48, 55} These initial values are then applied to a FFCF, where the first-order response function is used to reproduce the linear FTIR line shape.^{54, 56} The FTIR line shape is fit by iteratively varying the amplitudes as well as the central frequencies. It is worth noting the CLS method was developed using the short-time approximation, so the values for Δ and T_2 are underestimated due to the inability of this method to distinguish between homogeneous terms and fast spectral diffusion (compared with the time scale of the free induction decay). Therefore, the floated Δ and T_2 are constrained to only increase from the estimated values.

3. The Vibrational Heavy Atom Effect and its Impact on Relaxation and Spectral Diffusion in Triphenyl Hydride Complexes

Reprinted with permission from:

Pyles, C. G., Olson, C. M., & Massari, A. M. (2018). Vibrational heavy atom effect controls relaxation and spectral diffusion in triphenyl hydride complexes. *Chemical Physics*, 512, 98-103.

Copyright © 2018 Chemical Physics.

3.1 Chapter Summary

In this chapter, a series of three triphenyl hydride compounds was investigated in a range of solvents by Fourier transform infrared (FTIR), IR pump-probe, and two-dimensional IR (2D-IR) spectroscopies. The mass of the central atom of the three compounds was varied systematically down the group 14 elements of silicon, germanium, and tin. FTIR studies provided evidence that the solvent perturbs the three hydride modes in a similar manner, as indicated by identical solvatochromic and broadening trends. IR pump-probe measurements showed that the vibrational lifetime of the hydride stretch increased when the mass of the central atom increased. Density functional theory calculations asserted that the vibrational modes of the three compounds are nearly identical except for the hydride stretching and wagging modes. Interestingly, frequency-frequency correlation functions obtained from 2D-IR spectra indicated that an increasingly large central atom produces small, but measurable changes in the dynamics of the solvation shell surrounding each compound.

3.2 Introduction

The ability to control the flow of vibrational energy in a molecule has the potential to enable bond-specific reactivity.^{57, 58} Pioneering work by Crim and coworkers showed that localizing energy in a vibrational mode that lies along the reaction coordinate activates that bond to break upon a subsequent collision or photodissociation event.⁵⁹⁻⁶¹ A crucial condition to achieve this level of control is that the desired chemical reaction must occur before intramolecular vibrational redistribution (IVR) is complete, typically on the picosecond time scale. IVR converts bond-localized energy into nothing more than

molecular scale heat.^{57, 58} For this reason, confining vibrational energy in a specific degree of freedom has remained a perennial theme for several decades. For example, structural motifs such as acetylene bridges have been shown experimentally to assert some control over IVR and direct product distributions.⁶² Classical trajectories highlighted the complexity of this effect showing that the influence of acetylene groups was difficult to predict and had a strong dependence on resonance conditions within the molecular structure that spanned the acetylene region.^{63, 64} IVR has also been studied in the condensed phase.^{44, 65-68}

In contrast to adding IVR blocking substituents, an alternate strategy is to vary the atomic masses involved in a vibrational mode. This can be effective for two reasons. First, varying the vibrational frequency modulates anharmonic coupling to lower frequency modes, as is often found in cases of isotopic substitution. For example, silicon surfaces passivated with deuterium rather than hydrogen exhibit decreased reactivity due to the shorter vibrational lifetime of the silicon deuteride mode.⁶⁹ Second, the inclusion of an atom with a larger mass can act as a vibrationally insulating element. Rogers and coworkers reported that the presence of a heavy central atom prevented IVR on the basis of product distributions following decomposition of excited tetraallyl tin radicals.⁷⁰ Similarly, Arrivo and Heilweil showed that vibrational excitation in an OH group bound to a silicon atom was conserved throughout collision and formation of a hydrogen bond, implying that even in the condensed phase a heavier atom could serve to prevent IVR.⁷¹ We refer to this phenomenon as the vibrational heavy atom effect (VHAE) to distinguish it from the better known “heavy atom effect” in which a massive atom enhances spin-orbit coupling and

intersystem crossing.⁷² The VHAE has found new utility in recent years to extend the lifetimes of vibrational probes in nonlinear spectroscopy so that chemical dynamics on longer time scales can be measured.⁷³⁻⁷⁸

Classical simulations by Lopez and Marcus confirmed that doubling the mass of a central atom inhibits energy transfer between ligands on a metal complex.⁷⁹ However, a series of studies by Wrigley and Rabinovich on allyl tin and lead complexes concluded that, although some experimental observations were suggestive of a VHAE, product distributions following reaction with hydrogen were not consistent with energy transfer blocking by the heavier atom.^{80, 81} Classical and quantum mechanical calculations have emphasized that mass alone cannot always explain many of the experimental reports and that local resonances proximal to the heavy atom as well as tunneling must be invoked for a more complete description.^{82, 83} Even amidst the resurgence of interest in the VHAE, examples exist in which the vibrational lifetime is unpredictable. For example, Bian and coworkers reported that trichlorosilane, triethylsilane, and deuterated chloroform had vibrational lifetimes of 148, 6.7, and 15.7 ps, respectively, clearly showing that IVR sometimes depends on more than atomic masses alone.⁷⁴

The current study compares vibrational energy relaxation (VER) for three triphenyl hydride complexes in which the mass of the central atom increases moving down the group 14 elements in the periodic table. IR pump-probe measurements were carried out on the hydride stretching mode (ν_{M-H}) in three different solvents to explore the possibility of solvent-assisted IVR and intermolecular VER. Complementary DFT calculations identified differences in electronic structure, while isotopic substitution was used to test

alternate relaxation pathways. The three compounds were then further analyzed via two-dimensional infrared (2D-IR) spectroscopy to establish the impact of atomic mass on spectral diffusion.

3.3 Materials & Methods

Triphenyl silane (TriPS), triphenyl germanium hydride (TriPG), triphenyl tin hydride (97% purity, TriPT), tetrahydrofuran (THF, anhydrous, 99.9% purity), dimethylformamide (DMF, anhydrous, 99% purity), dimethylsulfoxide (DMSO, 99.9% purity), 1-octanol (99% purity), isopropanol (anhydrous, 99.5% purity), ethanol (99% purity), and methanol (99.9% purity) were used as received from Sigma Aldrich. Acetone (99.9% purity), pentane (98% purity), and 1-butanol (99.9% purity) were used as received from Fisher Scientific. Chloroform (anhydrous, 99.9% purity) was purchased from Acros Organics.

Deuterated TriPS- d_1 was synthesized in accordance with previously published procedures⁸⁴ by dissolving LiAlD₄ in THF at -10 °C. The THF solution was then added dropwise to Ph₃SnCl. After reacting for approximately one hour, nearly 99% substitution of Cl by D occurred according to ¹H-NMR and ²H-NMR spectra. The reaction was quenched with water and the product was extracted to yield a pale-yellow oil.

All solutions studied via linear and nonlinear IR spectroscopies were 5% w/w Ph₃M-H in various solvents, with M representing Si, Ge, or Sn. IR measurements were performed within 2 hours of solution preparation. TriPG and TriPT solutions were sonicated and filtered through a 0.45 μm syringe filter to minimize scatter. All spectroscopic measurements studied a small volume of sample solution sandwiched between two 3 mm thick CaF₂ windows with a 50 μM Teflon spacer.

Fourier-transform infrared (FTIR) spectra were collected on a Nicolet 6700 FTIR spectrometer (Thermo Scientific) as an average of 16 scans with a resolution of 0.5 cm^{-1} . The FTIR sample chamber was purged with dry air ($-100\text{ }^{\circ}\text{F}$ dew point) to minimize contributions from water vapor absorption. TriPS and TriPG spectra had their corresponding neat solvent spectra subtracted. TriPT spectra were processed by subtracting the spectra of Ph_3SnCl in corresponding solvents with a small axis offset to remove phenyl ligand overtone absorptions that overlapped with the Sn hydride stretch.

The laser system for 2D-IR and pump probe measurements has been described in previous publications^{52, 85} and Chapter 2 of this thesis. The mid-IR pulses were centered at approximately 2160 , 2040 , or 1840 cm^{-1} for the Si, Ge, or Sn hydride vibrations, respectively. The instrument was continuously purged with dry air ($-100\text{ }^{\circ}\text{F}$ dew point) from the point of mid-IR generation to signal detection for all data collection.

IR pump-probe measurements were performed with the pump beam polarization set to the magic angle relative to the probe beam ($\sim 54.7^{\circ}$) immediately before the sample.³⁶ The transmitted probe beam passed through an analyzing polarizer set to transmit p-polarized radiation (parallel to the table surface) immediately after the sample. The probe beam was then spectrally resolved in a 0.32 m monochromator with a 75 lines/mm grating and detected with a liquid- N_2 -cooled 64-element mercury cadmium telluride (MCT) linear array detector (Infrared Associates, Inc.). The spectral resolution of the system was 4 cm^{-1} . Vibrational relaxation lifetimes (T_1) were obtained by fitting a single exponential decay without an offset to the data in the $\nu=0-1$ transition region. The 2D-IR data were analyzed with the center line slope (CLS) method and processed with the FTIR spectra to obtain the

frequency-frequency correlation function (FFCF) for each hydride mode.^{48, 55} Density functional theory (DFT) calculations were performed for all three hydride complexes in Gaussian09 using the restricted B3LYP functional with the LANL2DZ basis set.⁸⁶

3.4 Results and Discussion

FTIR spectra highlighting the hydride stretching mode on TriPS, TriPG, and TriPT in pentane, chloroform, and isopropanol are presented in Figure 3.1.

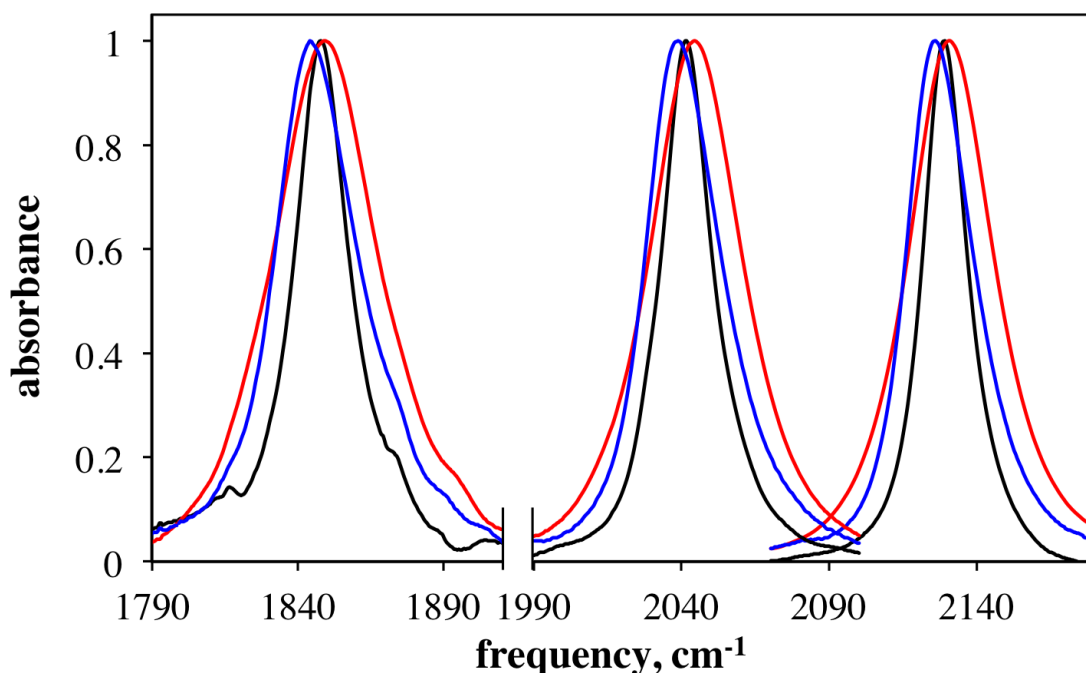


Figure 3.1. Solvent-subtracted, baselined, and normalized FTIR spectra of the M-H vibrational mode for TriPS, TriPG, and TriPT in pentane (black), chloroform (red), and isopropanol (blue).

These three solvents were chosen to sample the full ranges of hydride peak widths and central frequencies based on an extensive study of the three compounds in a wide range of solvents (Figure 3.2). The spectral broadening trends imparted by the solvents are consistent for all three compounds: the peaks exhibit the most broadening in chloroform and the narrowest spectra in pentane. The hydride stretches also exhibit the same solvatochromic shifts with ν_{M-H} following the trend of isopropanol < pentane < chloroform,

with chloroform inducing the largest red-shift. We have recently shown that the solvatochromic trends for TriPS can be attributed to specific hydrogen and halogen bonding interactions for isopropanol and chloroform, respectively.⁴⁶

Figure 3.3 demonstrates that the identity of the central atom has little influence on the extent to which the average frequency is perturbed by the surrounding solvent. The fact that the solvent interacts similarly with these three compounds is preliminary evidence that any differences observed in hydride relaxation are not due to anomalous differences in solvent-assisted relaxation.

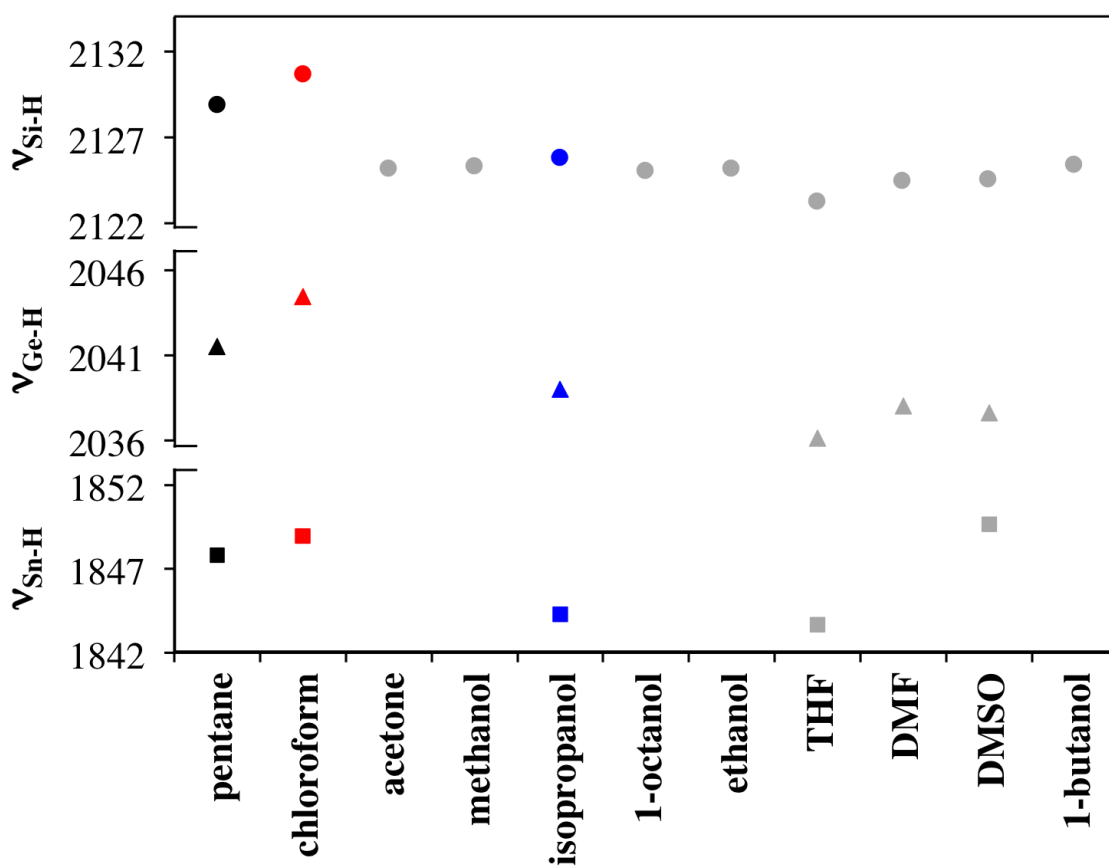


Figure 3.2. Center frequencies for the $\nu_{\text{Si-H}}$ (circles), $\nu_{\text{Ge-H}}$ (triangles), and $\nu_{\text{Sn-H}}$ (squares) in various solvents. Black, red and blue symbols indicate samples in pentane, chloroform, and isopropanol, respectively, that were further studied via pump-probe spectroscopy.

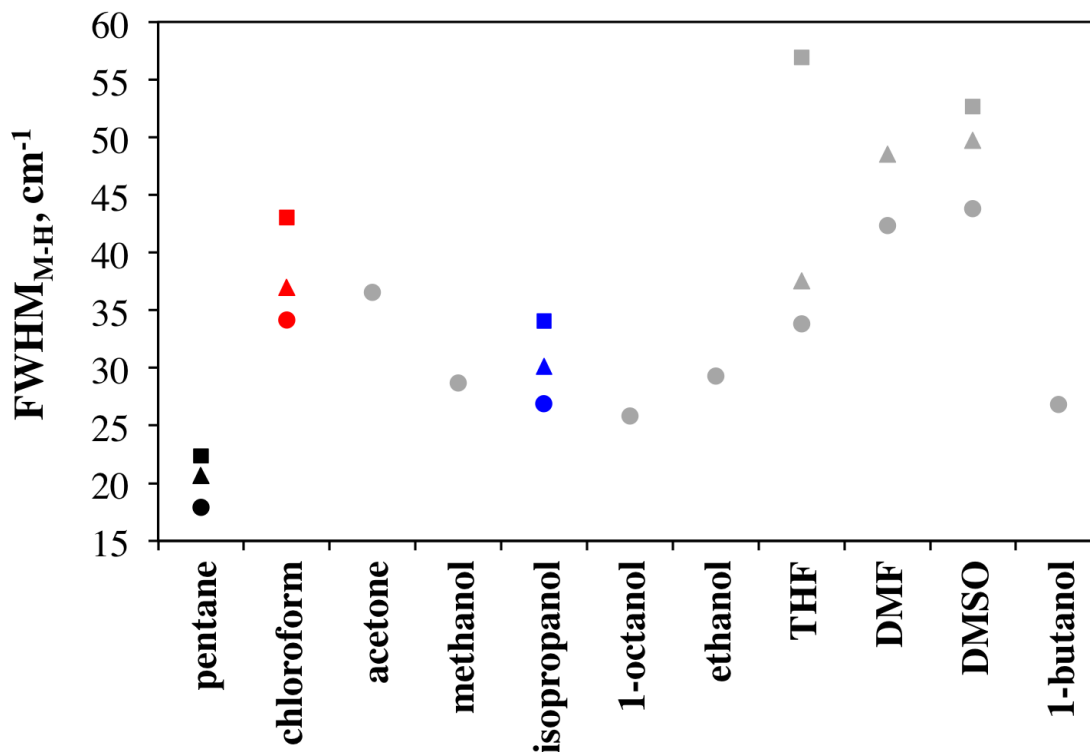


Figure 3.3. FWHM values for the M-H stretch of TriPS (circles), TriPG (triangles), and TriPT (squares) in various solvents.

The hydride vibrational relaxation times (T_1) were determined by IR pump-probe spectroscopy for all three compounds in the same set of solvents. Population decays show that germanium and tin hydrides (Figure 3.4 b, c) relax notably slower than silicon hydride (Figure 3.4a) regardless of the solvent. This is consistent with the isolating effect of the heavier atoms on the vibrational energy in the hydride bond. The vibrational lifetime is only slightly longer on average for TriPT relative to TriPG, despite the fact that tin is in the period below germanium.

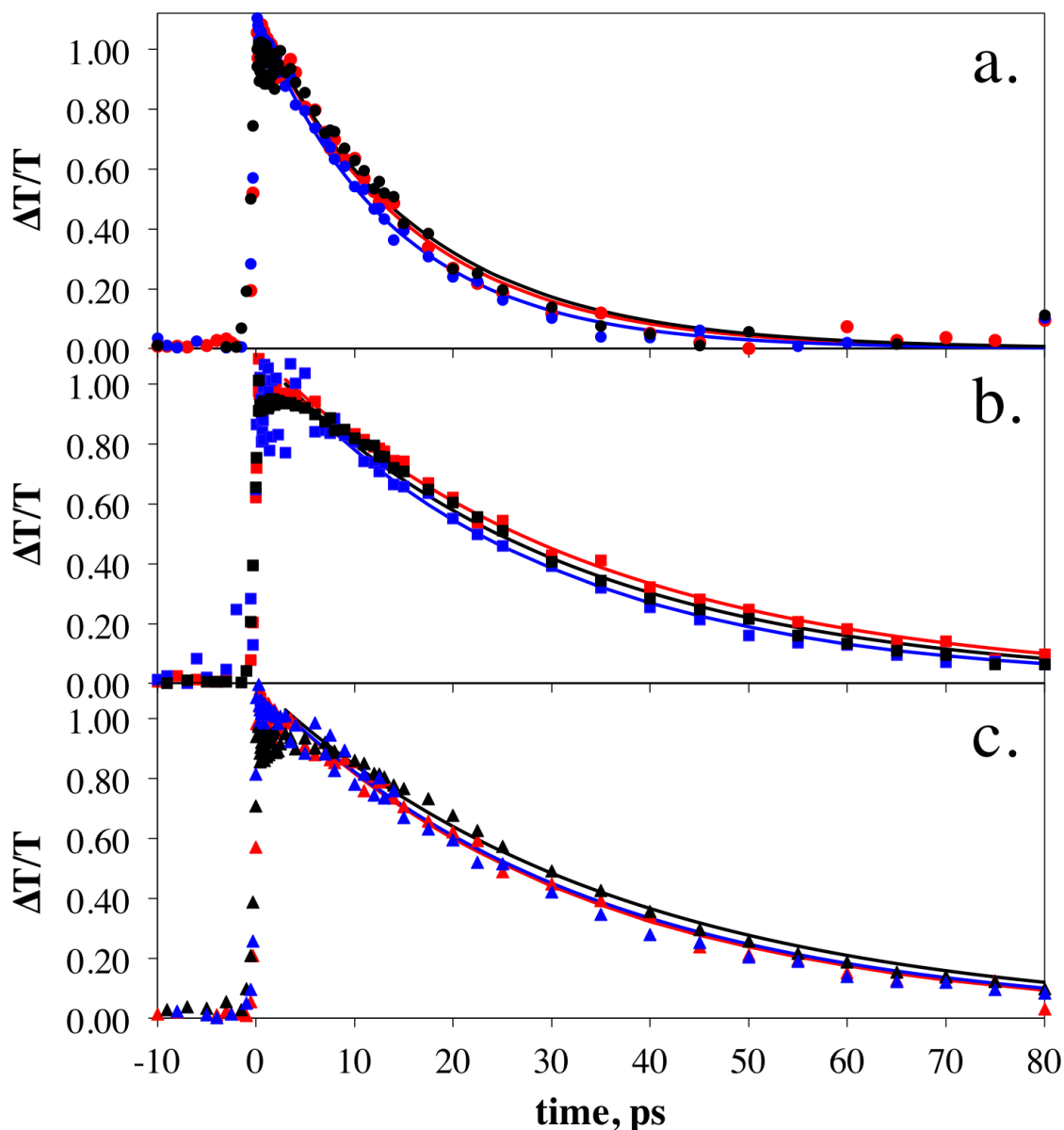


Figure 3.4. IR pump probe decays for the hydride stretch on (a) TriPS near 2132 cm^{-1} , (b) TriPG near 2045 cm^{-1} , and (c) TriPT near 1855 cm^{-1} . Black, red, and blue colors correspond to pentane, chloroform, and isopropanol, respectively, in all three frames. Overlaid solid lines of the same color show single exponential curves that fit the data. Error is reflected in the fit to single exponential parameters mentioned in Table 3.1.

The data in are well described by single exponential decays without an offset and the relaxation lifetimes are compiled in Table 3.1. In chloroform, the hydride T_1 values for TriPG and TriPT are the same within error, but are statistically longer for TriPT than TriPG in isopropanol and pentane. The changes in vibrational lifetime with solvent are subtle

among the three different central atom types, but show a mild trend toward faster relaxation in more polar solvents. The relative insensitivity of T_1 to solvent type indicates that intermolecular VER into solvent modes is not a dominant relaxation pathway and that the solvent has a minimal influence on intramolecular redistribution.

Table 3.1. Hydride vibrational lifetimes. Errors represent the standard error of the fit.

compound	T_1 (ps)		
	pentane	chloroform	isopropanol
TriPS	17.1 (± 0.3)	16.3 (± 0.4)	14.0 (± 0.2)
TriPS- d_1		16 (± 1.4)	
TriPG	32.3 (± 0.4)	33.9 (± 0.5)	29 (± 1.0)
TriPT	38.2 (± 0.7)	34 (± 1.0)	31.1 (± 0.3)

The VHAE can be understood to first order by treating the rate of vibrational energy transfer to a continuum of accepting states with Fermi's Golden Rule (FGR). The FGR treatment predicts that the rate coefficient should be proportional to the coupling matrix element, and work by Lederman and coworkers showed that the coupling varies inversely with the mass of the central atom.⁸⁷ Figure 3.5 presents the measured rate coefficients for energy relaxation as a function of the inverse mass. The data collected in pentane are consistent with the linear dependence on inverse atomic mass and support the notion that the VHAE is driven by a decrease in coupling of energy out of the excited hydride mode when solvation is non-specific. Similar trends are present in chloroform and isopropanol but deviations from linearity are apparent. The strongest deviations occur in chloroform, which we recently showed to have halogen bonding interactions with silicon hydrides.³⁶

Figure 3.5 indicates that relaxation remains dominated by vibrational coupling, but that specific solvent-solute interactions may modulate IVR and/or VER.^{85, 88}

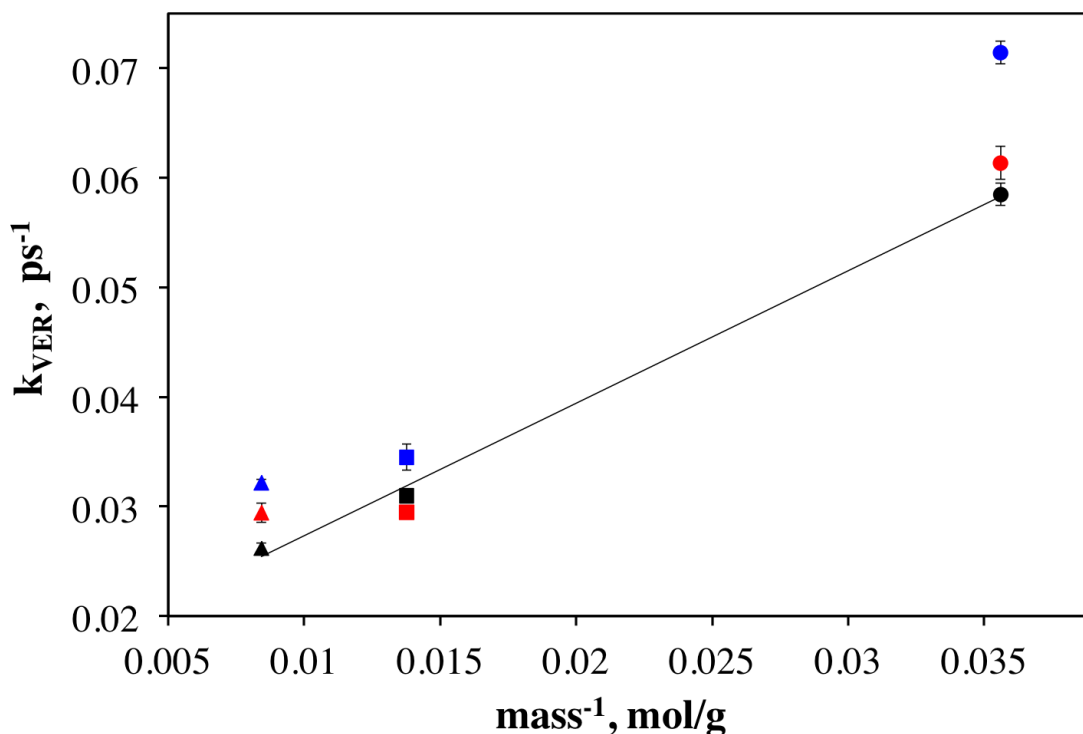


Figure 3.5. Rate coefficients for energy relaxation as a function of the inverse mass of the central atom (Si = circles, Ge = squares, Sn = triangles) in pentane (black), chloroform (red), and isopropanol (blue). The solid line is a linear regression fit to the pentane data points only.

One challenge with comparing these lifetimes directly is that the hydride stretching frequency changes with the central atom identity, as shown in Figure 3.1. Frequency shifts associated with changes in reduced mass and electronic structure open the possibility for alternate relaxation pathways that may utilize a different palette of vibrational modes acting as energy acceptors. This would in turn lead to a different relaxation rate that was not due to the VHAЕ. To investigate this possibility, DFT calculations were performed at the LANL2DZ level of theory to compare changes in electronic structure induced by the central atom. Figure 3.6 shows frequency calculations for the three compounds. The high frequency hydride stretches are affected by the reduced mass in the hydride mode, but

replacing the central atom has a relatively small impact on the reduced mass. These mass changes alone would lead to shifts of less than 30 cm^{-1} for Ge-H or Sn-H relative to Si-H. Changes in the electronic configuration with different metals lead to more significant shifts in the hydride frequency. Nonetheless, most of the non-hydride vibrations are minimally perturbed by the central atom identity. The large frequency shifts in the hydride allow different combinations of accepting modes for the three compounds. For example, TriPS could be efficiently relaxed by transferring two quanta directly into C-C ligand modes that reside at exactly half of the Si-H stretching frequency, while the Ge-H nor Sn-H frequencies are too low to utilize this pathway. Each compound also has one other mode, the hydride wagging mode, which is notably sensitive at 830 , 740 , and 605 cm^{-1} for TriPS, TriPG, and TriPT, respectively.

In order to test the role of electronic structure changes on VER, we carried out IR pump-probe measurements on TriPS- d_1 in chloroform in which the hydrogen was replaced with deuterium (Figure 3.7). As shown in Table 3.1, we find that the dramatic frequency change has no impact on the vibrational lifetime. The DFT calculated frequencies are overlaid in Figure 3.6 as well and show that only the hydride stretching and wagging modes are notably impacted by deuteration.

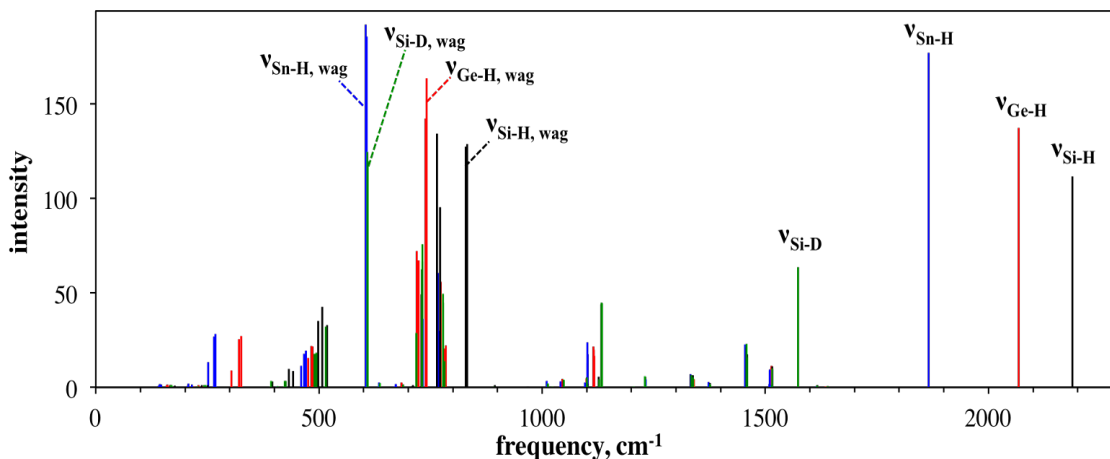


Figure 3.6. DFT calculated vibrational frequencies and intensities for TriPS (black), TriPG (red), TriPT (blue), and TriPS- d_1 (green) in the gas phase using the LANL2DZ functional and B3LYP basis set.

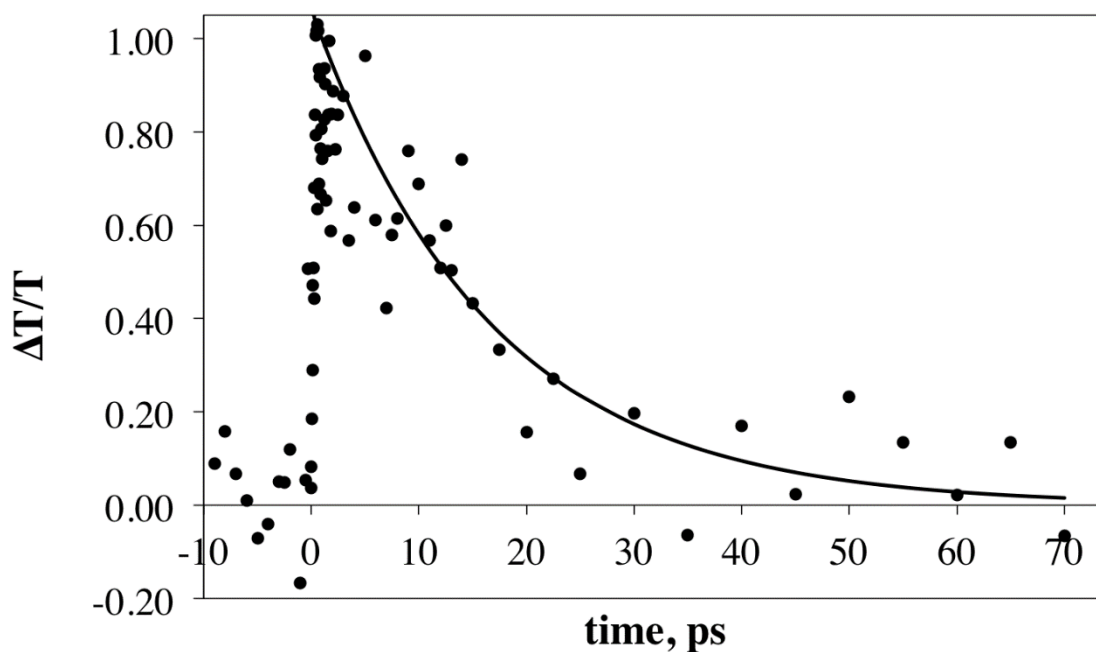


Figure 3.7. IR pump-probe decay for the $\nu=0-1$ transition of the deuteride stretch ($\nu_{\text{Si-D}}$) on TriPS- d_1 at 1550 cm^{-1} .

Fortuitously, the Si-D wagging mode for TriPS- d_1 is nearly identical (609 cm^{-1}) to the Sn-H wagging mode for TriPT, yet the hydride relaxation matches that of TriPS. The relaxation mechanism must be the same for this vibrational mode on a triphenyl hydride complex regardless of whether it is at 2160 cm^{-1} or 1549 cm^{-1} , and arguably for the TriPG

and TriPT hydride frequencies that fall within this range as well. This further supports the conclusion that VER is slower in TriPG and TriPT as a result of the VHAE, rather than an electronic effect leading to anomalously fast relaxation for TriPS. Despite regular usage to extend the dynamic range of vibrational probes in 2D-IR spectroscopy, to the best of our knowledge, it has not been demonstrated whether the VHAE impacts spectral diffusion. To this end, 2D-IR measurements were carried out on TriPS, TriPG, and TriPT in chloroform. These measurements were restricted to chloroform given that it is a strongly interacting solvent and would offer the most apparent differences in dynamics. Figure 3.8 shows representative 2D-IR spectra at short and long T_w values.

CLS analysis was carried out on all 2D-IR spectra (Figure 3.9 and Figure 3.10). The decay times obtained in the CLS decays are an accurate measurement of the system dynamics and are shown in Table 3.2 as the τ parameter. The amplitudes of the exponential terms do not give accurately either the dynamic contributions to the FTIR line shape or the homogeneous linewidth. However, it has been shown that the CLS decay can be processed with the FTIR line shape to obtain the full FFCF describing the vibrational dynamics of a mode.^{48, 55} The FTIR spectra and CLS decays were used to obtain the FFCF parameters shown in Table 3.2, which quantify the dynamics occurring for each compound. Differences between the parameters are subtle and in some cases the error bars are overlapping, yet there are some trends worth noting. A heavier atom in the hydride bond not only extends T_1 but also increases the inhomogeneous correlation time, τ . The change in central atom apparently has a mild influence on the time scales of frequency fluctuations

experienced by ν_{M-H} . Furthermore, there is a small but statistically significant decrease in the homogeneous linewidth, Γ , as the mass of the central atom increases.

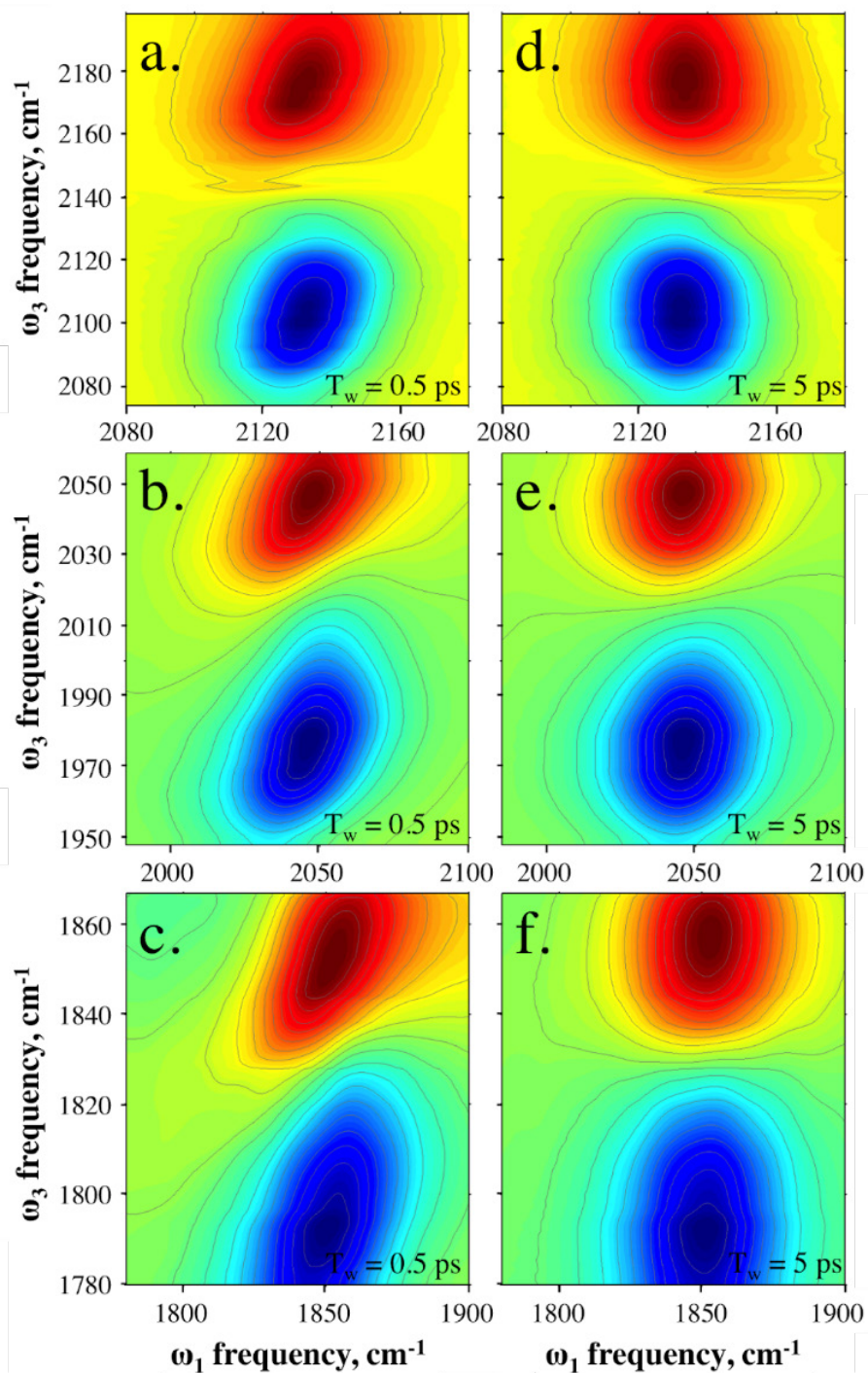


Figure 3.8. Representative 2D-IR spectra of (top to bottom) TriPS, TriPG, and TriPT in chloroform. Spectra in the left column were recorded at $T_w = 0.5$ ps; spectra on the right column were recorded at $T_w = 5$ ps.

Figure 3.11 demonstrates the trends in correlation time and homogeneous linewidth obtained by 2D-IR. The atomic radius of the central atom was chosen as the independent variable, since it changes monotonically with the elemental mass. There is no reason to expect a linear change in a particular solvation parameter with the atomic radius, and the curvatures of these plots are arbitrary. What is of note is that minor differences in molecular structure induced by atomic substitution lead to changes in the solvation shell, and small but measurable differences in spectral diffusion and homogeneous dynamics. Even though the three complexes are structurally similar, the size of the central atom will affect the overall molecular diameter and relative degree of exposure of the hydride mode to the solvent. In other words, the solvation shell proximal to the hydride mode may vary with atomic size, leading to the observed trends in spectral diffusion and homogeneous dephasing.

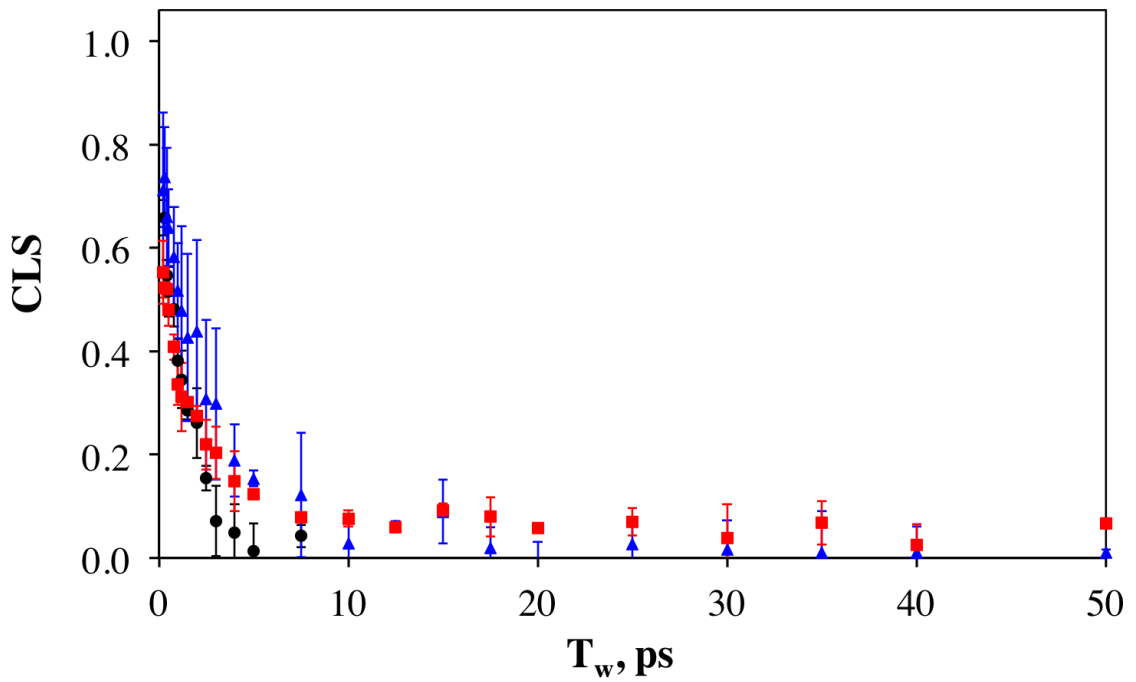


Figure 3.9. CLS values as a function of T_w for TriPS (black circles), TriPG (red squares), and TriPT (blue triangles). All three CLS decays were plotted to a single exponential and decay to approximately zero at long T_w s. Error bars represent the standard deviation of CLS values for a given T_w across three scans.

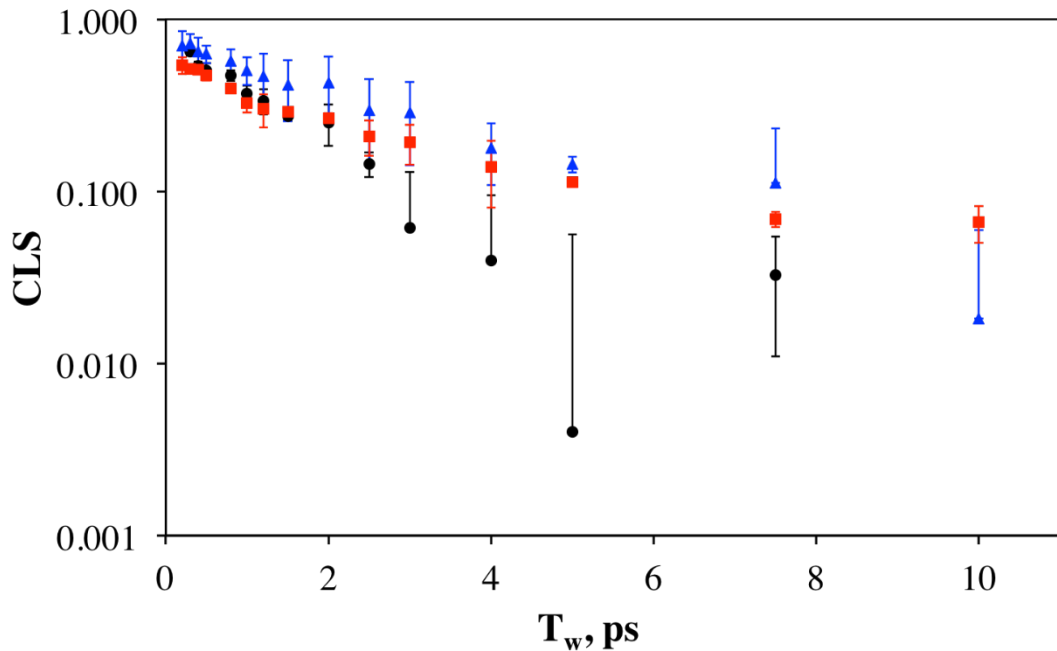


Figure 3.10. CLS values as a function of T_w (same as) at shorter T_w s and with a logarithmic y-axis to highlight subtle differences on this time scale. Error bars represent the standard deviation of CLS values for a given T_w across three scans.

Table 3.2. FFCF parameters obtained for the three triphenyl hydride compounds in chloroform.

compound	Δ (cm ⁻¹) ^a	τ (ps) ^b	Γ (cm ⁻¹) ^a
TriPS	15 (± 2)	1.5 (± 0.1)	6.2 (+0.7/-0.8)
TriPG	12.8 (± 0.3)	2.0 (± 0.7)	4.1 (+0.7/-1.0)
TriPT	18.4 (± 0.1)	2.9 (± 0.6)	3.6 (+0.2/-0.3)

a. Errors show the range over which the parameter could be increased while the other parameters floated to fit the FTIR line shape 95% as well as the best value

b. Standard error of the exponential fit

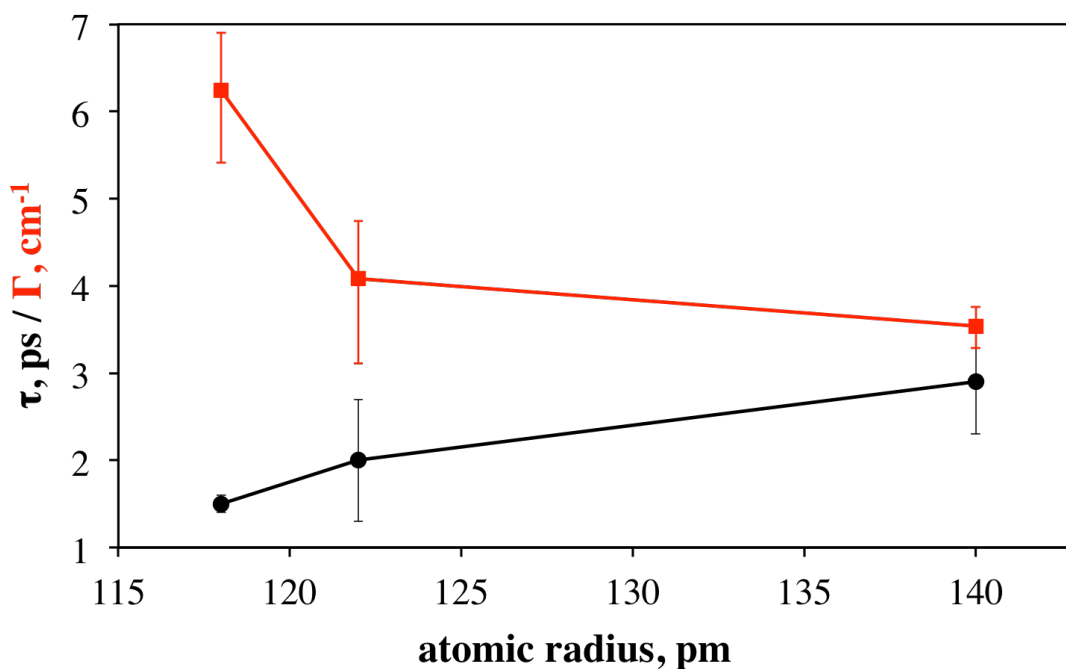


Figure 3.11. Trends in FFCF parameters τ (black circles) and Γ (red squares) as a function of atomic radius for TriPS, TriPG, and TriPT in CHCl₃.

3.5 Conclusions

The VHAE was found to prevent IVR and extend the vibrational lifetimes of a series of homologous triphenyl hydrides. When solvent-solute interactions were weak, the vibrational relaxation rate was inversely related to the mass of the central atom, showing that the heavier mass acts to decrease coupling of the excited state to a continuum of accepting modes. Stronger, more specific solvent interactions modulate IVR to some degree, most likely by varying the density of accepting states, as described by others.⁸⁸ Isotopic substitution in the silicon hydride resulted in no change in relaxation rate, demonstrating that the observed VHAE is not dependent on resonance conditions or changes in electronic structure induced by the heavier atom. 2D-IR measurements revealed that small but systematic changes were present in the spectral diffusion experienced by the hydride modes in this set of compounds. In the context of using the VHAE to extend the lifetime of vibrational probes, this is a cautionary observation that replacing a single atom in a molecular structure can lead to subtle structural changes that perturb the solvation shell in the vicinity of the sensing mode and modify the observed dynamics.

3.6 Full Set of 2D-IR Data

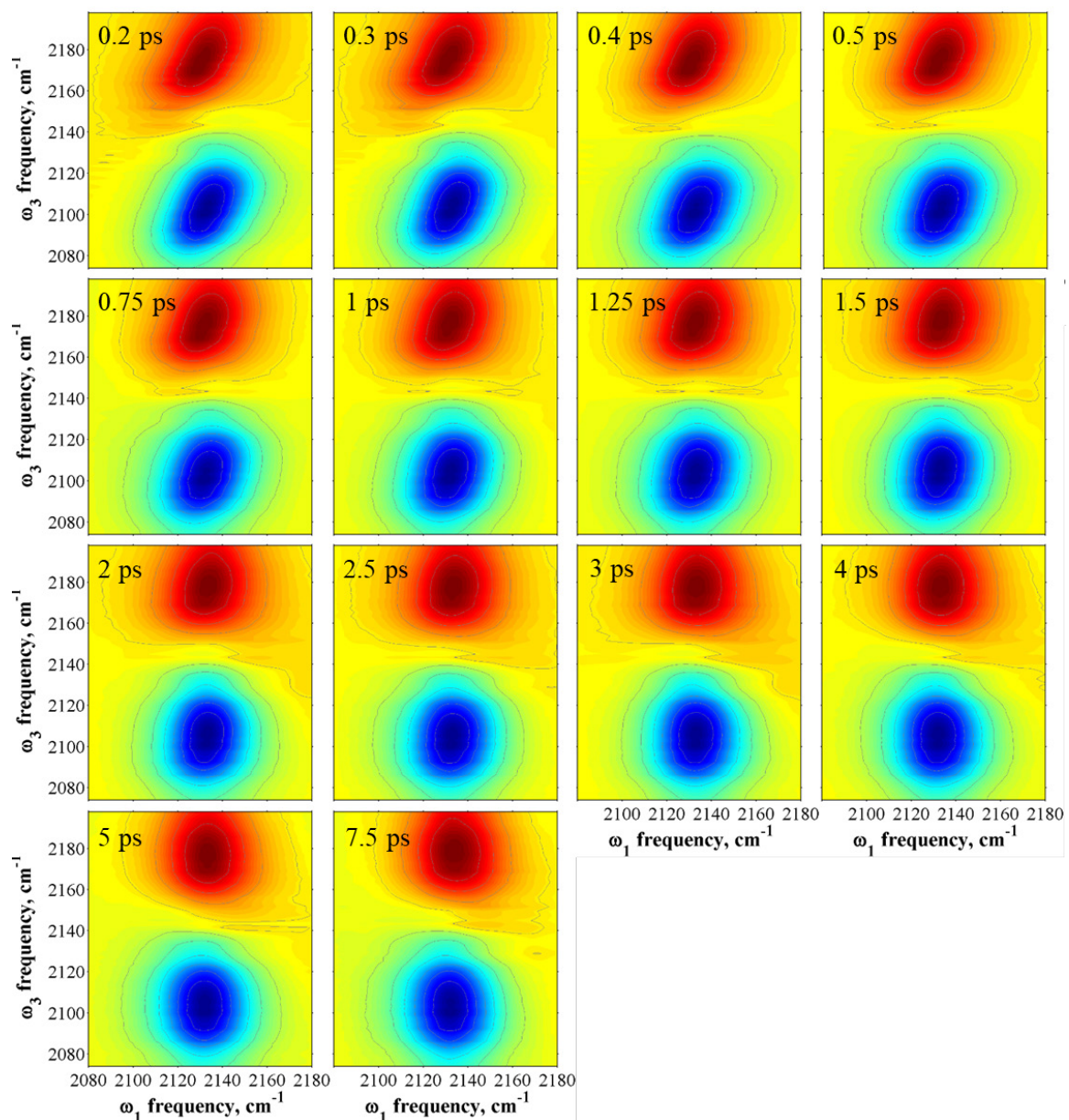


Figure 3.12: Complete set of averaged 2D-IR spectra for the $\nu_{\text{Si-H}}$ stretch of TriPS in CHCl_3 at a range of T_{ws} .

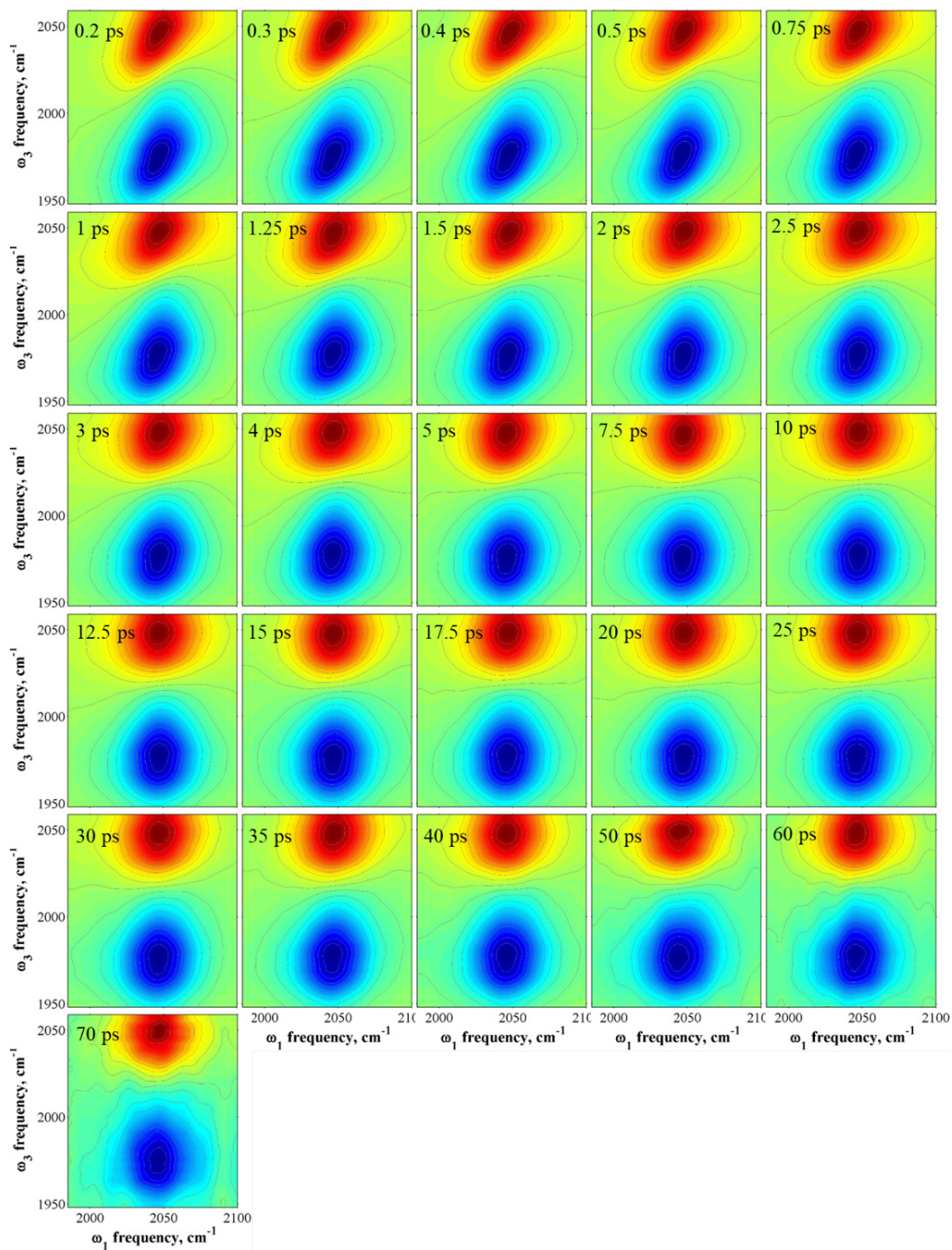


Figure 3.13. Complete set of averaged 2D-IR spectra for the $\nu_{\text{Ge-H}}$ stretch of TriPG in CHCl_3 at a range of T_{ws} .

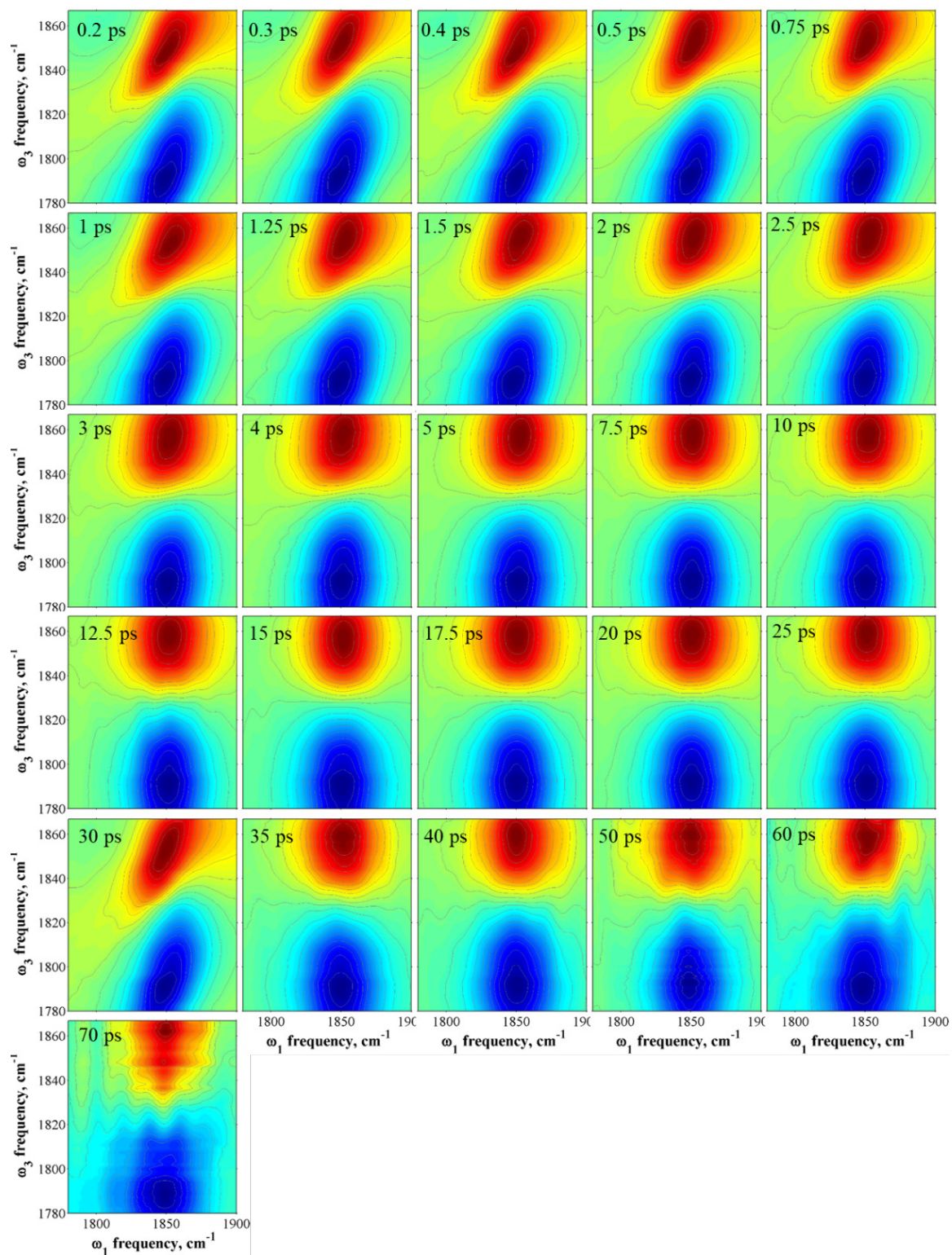


Figure 3.14. Complete set of averaged 2D-IR spectra for the $\nu_{\text{Sn-H}}$ stretch of TriPT in CHCl_3 at a range of T_{ws} .

4. Ultrafast Studies of CO₂ (g) as a Precursor to Dissolved Gases

Results herein are co-authored with Ivan C. Spector of the Massari group and can also be found in Chapter 5 of the thesis,

Spector, Ivan. (2020). Two-Dimensional Infrared Spectroscopy of Heterogeneous Systems: On the Path to Measuring Charge Transfer in Solution Processed Organic Electronic Thin Films. Retrieved from the University of Minnesota Digital Conservancy, <https://hdl.handle.net/11299/218681>.

4.1 Chapter Summary

Two-dimensional IR (2D-IR) spectroscopy was used to study a gaseous CO₂ – N₂ mixture under ambient pressure and temperature. Given the low temperature and pressure used for these measurements, molecule collisions happen infrequently. This leads to minimal J-state scrambling, in which multiple rovibrational transitions on a 2D spectrum fail to coalesce into one peak even with significant waiting times (T_w). Instead, we observe strong coupling and correlation of quantum mechanical states during the vibrationally excited state period. Coherence and population exchange occurring during vibrational excitation give rise to off-diagonal features in the 2D-IR spectra. The curvature of these features can be used to accurately calculate rotational and rotation-vibration interaction constants. Spectra were collected on both 70 and 150 lines/mm gratings; the higher resolution data reported herein confirmed the predicted off-diagonal peak splitting. These results provide an alternative method for determining rotational constants of gaseous systems. An understanding of the gas-phase spectra also aids interpretation of mixed systems in which CO₂ may exist as a combination of gaseous and dissolved molecules.

4.2 Introduction

Carbon dioxide (CO₂) is the most abundant of antropogenic greenhouse gases. The literature contains a multitude of experimental and computational studies aimed at both understanding its behavior and determining how to use CO₂ as an alternative fuel source.⁸⁹⁻
⁹³ Despite the depth and quantity of existing reports, it is not clear how CO₂ behaves at high temperatures and pressures, especially when confined to a storage medium. The nature

of the storage medium such as pore size, intermolecular interactions, and glass transition temperature can also affect the behavior of the CO₂ guest. This chapter aims to understand the gaseous behavior prior to containment, whereas Chapter 5 describes CO₂ dissolved in polymers and Chapter 7 describes the expected results when CO₂ adsorbs to a microporous structure.

Various spectroscopic methods have previously described the behavior of gaseous CO₂ by determining average structures of molecules and molecular clusters.⁹⁴⁻⁹⁷ These approaches inevitably use ensemble averaging, making it difficult to determine if structural configurations interconvert between one another. Line shape analysis can reveal some of the underlying gas-phase dynamics⁹⁸ but we aimed to better understand the motions of CO₂ on an ultrafast time scale. Prior studies by Mandal et. al used 2D-IR to study the ultrafast dynamics of the N₂O ν_3 asymmetric when incorporated with sulfur hexafluoride (SF₆) under pressures of 17 and 26 atm.⁹⁹ Pack and coworkers continued this study by measuring N₂O ν_3 dynamics under a variety of SF₆ pressures, ranging from a gaseous mixture to supercritical fluid, and eventually N₂O in liquid SF₆.¹⁰⁰ The studies conducted with a pressure of SF₆ \leq 26 atm yield intriguing results; At early waiting times (0.2 ps) rotational quantum numbers are conserved despite interconversion of the P- and R- branch species. However, molecular collisions occurring within the first ten picoseconds scramble the J-quantum numbers⁹⁹ and the line shape begins to more closely resemble that of N₂O in liquid SF₆. The N₂O ν_3 dynamics show evidence of free rotor character at all gas and supercritical densities, but an increase in SF₆ pressure makes collisions happen more frequently, thereby expediting the CLS decay for both diagonal and antidiagonal features

in the spectra.¹⁰⁰ Linear spectroscopic methods are unable to glean these insights about gas phase dynamics, highlighting the utility of 2D-IR spectroscopy.

In this chapter, I describe the 2D-IR spectra of a dilute CO₂ – N₂ mixture under ambient pressure and temperature (1 atm, 294 K). The CO₂ system uses a sufficiently low pressure such that rotational quantum numbers are conserved for nearly 100 ps and minimal J-scrambling occurs due to the infrequency of collisions. The off-diagonal features of a 2D-IR spectrum can also help determine rotational constants and anharmonic correction terms through a series of fitting steps which I describe in detail. The results herein reinforce the capability of 2D-IR to measure gas phase dynamics, even in dilute systems. Additionally, these results help inform more complex studies such as CO₂ dissolved inside polymers which I describe in Chapter 5.

4.3 Materials & Methods

Two 3 mm CaF₂ windows are separated by a 1 mm spacer in a custom-machined sample cell. Mass flow controllers (Unit Instruments Inc., UFC-1100) applied a continuous flow of carbon dioxide (99% purity, Airgas) through the cell during the measurements. High purity N₂ (99.9% purity, Airgas) was added as necessary to achieve 1 atm of pressure. Samples studied via 2D-IR typically had an optical density of 1.5 mOD at the P(2) rotational-vibrational band in the CO₂ asymmetric stretch. The absorption coefficient for CO₂ at 300 K of 0.025 Pa⁻¹m⁻¹ (or 2.53 atm⁻¹mm⁻¹),¹⁰¹ allows for estimating the partial pressure of CO₂ which was approximately 0.0006 atm for all measurements.

The 2D-IR instrument has been described in previous publications^{102, 103} and Chapter 2 of this thesis. Mid-IR pulses (3 μJ/pulse, 1 kHz repetition rate, 90 fs duration FWHM, ~200

cm⁻¹ bandwidth FWHM) were tuned to the CO₂ asymmetric stretching region (~ 2340 cm⁻¹). After dividing into three ~1 μJ p-polarized pulses, and the beams were focused on the sample in a BOXCARS geometry.¹⁰⁴ The vibrational echo generated by the sample must then be coaligned with a local oscillator pulse to obtain phase information. The signal was spectrally resolved in a 0.32 meter monochromator with a 75 or 150 line/mm grating, and detected with a liquid N₂ cooled 64-element mercury cadmium telluride (MCT) linear array detector (Infrared Associates, Inc.). The spectral resolution of the detection system was ~ 4 cm⁻¹ and 2 cm⁻¹ using 75 and 150 line gratings, respectively. Approximately 90% of the incident IR beams are absorbed by atmospheric CO₂, necessitating a constant positive pressure of dry N₂ and sealing the instrument throughout all measurements. Failure to adequately purge the instrument resulted in complete loss of signal.

4.4 Results and Discussion

2D-IR plots shown in Figure 4.1 show CO₂ at a short (1 ps) and long (100 ps) waiting time, denoted T_w. Each plot includes the FTIR spectrum of CO₂ at the top to highlight the similarities between the diagonal slice of the 2D spectrum and the linear absorption. The CO₂ spectrum has a P- branch due to J – 1 transitions during a v ± 1 transition and an R-branch due to J + 1 transitions during a v ± 1 transition.⁹⁸ However, the molecular symmetry of CO₂ (D_{∞h}) and spin statistics⁹⁸ dictate that only rotational transitions from even J states are allowed. This means the P- and R-branches only show every other transition beginning with P(2) and R(0), respectively. The peak spacing within each branch is given by 4B instead of the typical 2B, where B is the rotational constant, and the P(2) and R(0) peaks are separated by 6B instead of the usual 4B due to the absence of the P(1) peak.^{98, 105}

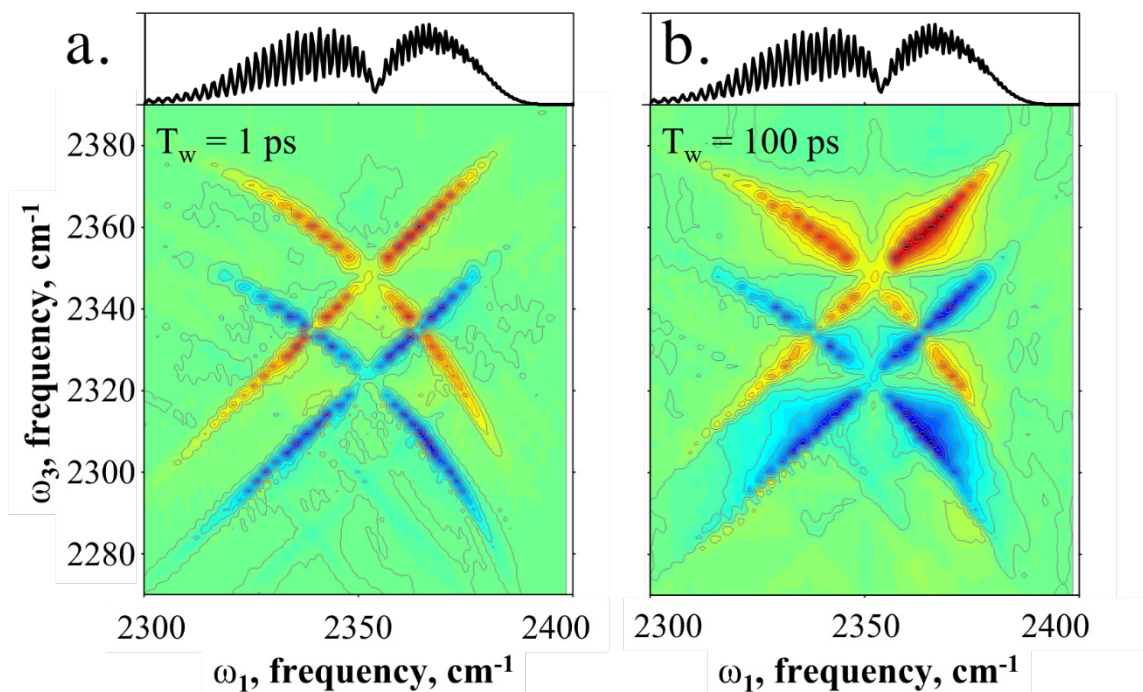


Figure 4.1. 2D-IR spectra of gaseous CO₂ at 6×10^{-4} atm diluted in N₂ to 1 atm at a) $T_w = 1$ ps and b) $T_w = 100$ ps. The FTIR spectrum of CO₂ is plotted above each 2D-IR spectrum for reference.

Red contours along the diagonal represent oscillators undergoing ground state bleach. In the context of CO₂ more specifically, this refers to oscillators which are excited from and emit vibrational echo in the same branch. The lower-frequency portion of the transitions along the diagonal represent the P- branch, whereas peaks further along the diagonal toward 2400 cm⁻¹ belong to the R- branch. The specific pathways that result in on-diagonal intensity are shown in Figures 2a and 2b. Blue peaks following the diagonal represent signal from excited state absorption. The excited state absorption is shifted down the ω_3 axis relative to the ground state bleach, and the magnitude of this shift represents the vibrational anharmonicity. For CO₂ (g) this value is 24 cm⁻¹ and is in agreement with previous results.¹⁰⁶ It is worth noting that the FTIR contain significantly more distinct peaks; Resolution limitations of the 2D-IR spectrometer make it difficult to separate each

individual rovibrational transition.

Peaks along the antidiagonal direction^{99, 100} and result in an “x” type pattern in the 2D spectra. Excited state population exchange occurring during waiting time T_w is one example of a process that leads to off-diagonal features (see Figure 4.2 panel c and d). A four-wave mixing experiment can give rise to 36 different density matrix pathways, though 6 are highlighted to aid in interpreting the “x” pattern on the 2D spectra.

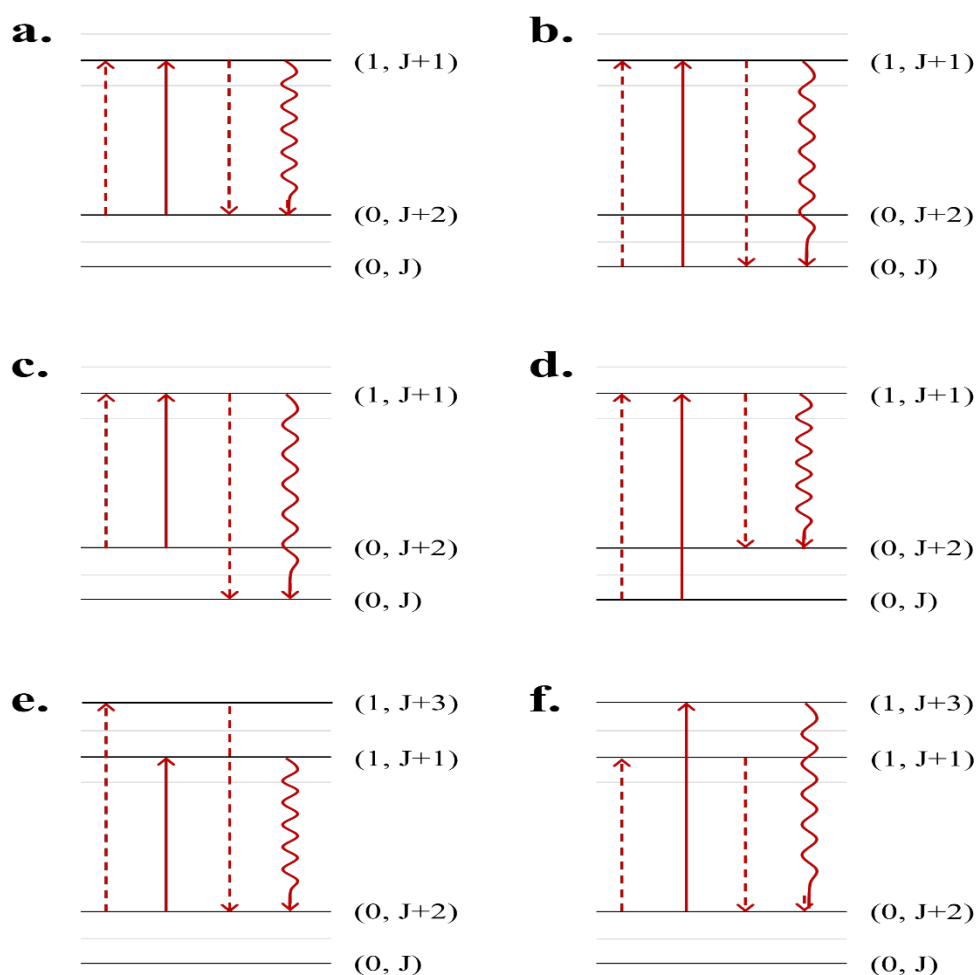


Figure 4.2. Six density matrix pathways which lead to 2D-IR signals for (a and b) ground state bleach, (c and d) population exchange, and (e and f) coherence exchange. Straight arrows represent the system interacting with an IR pulse on either the bra or ket side of the density matrix (solid and dashed arrows respectively); wavy lines indicate emission of vibrational echo signal.

For given rotational-vibrational state $|v, J\rangle$, the P- and R- branches provide two different pathways for creating that state via the first two pulse interactions of a 2D-IR experiment. When the state does not undergo J-scrambling (i.e spectral diffusion) during T_w , the state can likewise be stimulated to emit vibrational echo by two pathways back to the ground vibrational state. For example, the $|1, 1\rangle$ state can be formed by exciting either the the R(0) or P(2) transitions, denoted $|0, 0\rangle$ or $|0, 2\rangle$ respectively. The $|1, 1\rangle$ can then be stimulated to emit from that state back to either of the two starting states. In this example, excitation to $|1, 1\rangle$ via the P(2) followed by emission from $|1, 1\rangle$ to R(0) results in an off-diagonal peak.

Moderately dense samples can undergo J-scrambling via molecular collisions and exhibit line shape coalescence, i.e the peak loses its “x” character and appears more rounded even at early T_w s. The resulting peak shapes bear more resemblance to the vibrational probe dissolved in a liquid^{99, 100} than that of a free rotor. However, this study is carried out at ambient pressure and temperature such that the average collision time is ~ 200 ps. The shape of the outer contours of the 2D-IR spectrum at $T_w = 100$ ps (Figure 4.1 b) show weak evidence of J-scrambling. However, taking the summation of the off-diagonal contours and normalizing by the on-diagonal intensity^{107, 108} for a range of T_w s exhibits a monotonic increase indicative of J-scrambling. The off-diagonal growth is too slow to determine a time constant for this process with the limited data range. However, the long vibrational relaxation times for gaseous species make it possible to directly measure these dynamics on instruments with longer delay times.^{99, 100} To summarize, these measurements spanning

the a T_w of 100 ps show quantum states preserved for the vast majority of the CO_2 oscillators.

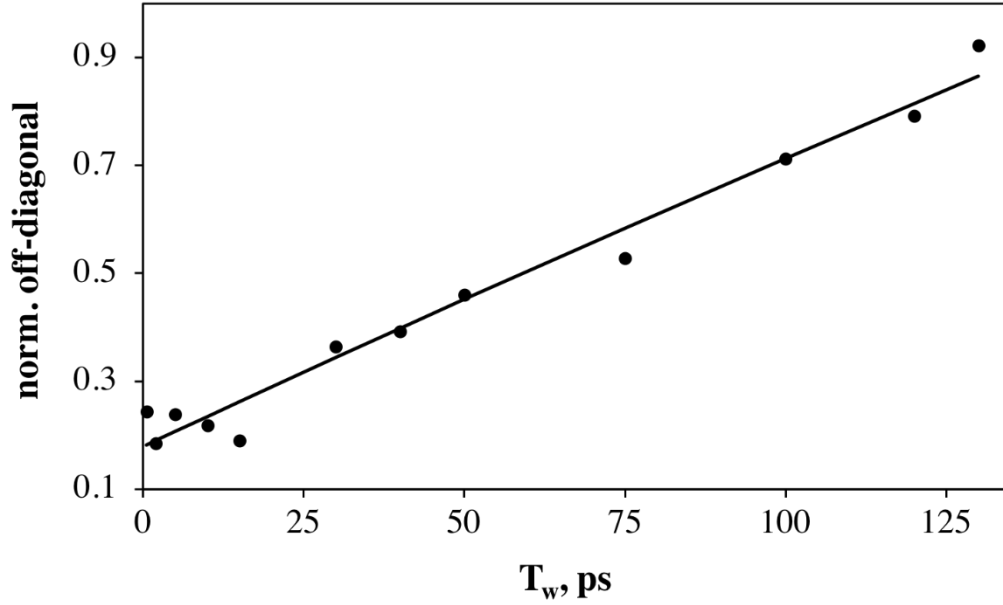


Figure 4.3. Off-diagonal intensity for the $v=0-1$ transition normalized by the on-diagonal intensity as a function of T_w .

The peaks laying along the diagonal follow a mostly straight line, yet the antidiagonal contours in Figure 4.1 possess a downward curvature. Transition frequencies in the P- and R- branches can be predicted with Equations 4.1 and 4.2:⁹⁸

$$\nu_P(J) = \nu_0 - 2J B_e - J(J - 2)\alpha_e \quad 4.1$$

$$\nu_R(J) = \nu_0 + 2(J + 1)B_e - (J + 1)(J + 3)\alpha_e \quad 4.2$$

Where these equations adjust the rotational constant B_v for each vibrational quantum state v . This is done through the use of the equilibrium rotational constant B_e , that is adjusted by the rotation-vibration interaction constant, α_e :

$$B_v = B_e - \alpha_e \left(v + \frac{1}{2} \right) \quad 4.3$$

The peak frequencies of transitions in the R-branch get closer with increasing J , whereas they become further apart in the P-branch. This is due to the α_e -dependence as seen in Equations 4.1 and 4.2. The transitions in both branches also grow increasingly closer in energy as the frequencies increase, due to J 's own increase toward negative and positive frequencies in the P- and R-branches, respectively. A spectrum schematic in Figure 4.4 demonstrates both of these trends, wherein the peaks growing closer with increasing frequency results in crosspeaks that curve downward. This behavior results from the influence of vibrational excitation on the rotational constant (B_v).

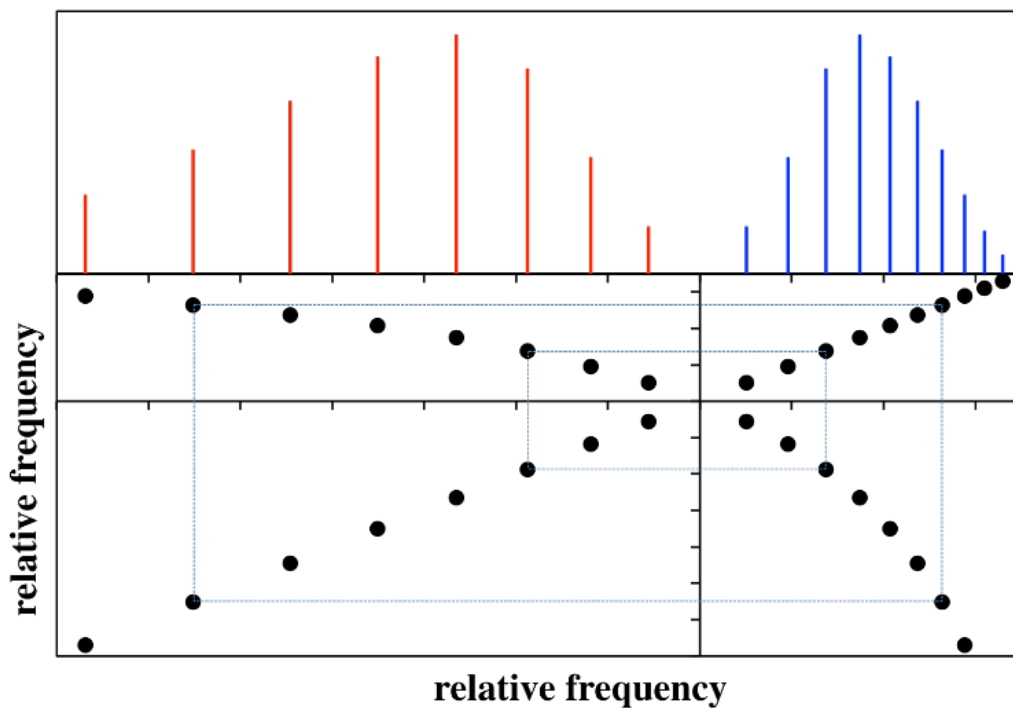


Figure 4.4. Schematic of a typical rotational-vibrational spectrum in which the transition spacing decreases in both P- and R-branches toward higher frequencies. The lower frame shows the resulting off-diagonal peaks that occur with downward curvature, as seen in experimentally in Figure 1.

The coordinates of an off-diagonal peak in the 2D-IR spectrum are given by (ω_1, ω_3) . For quadrant II (upper left), the position can be solved for by using by Equations 4.1 and 4.2 for the x and y-axis values respectively; the x- and y-axis values in quadrant IV (lower right) are given by Equations 4.2 and 4.1, respectively, for each particular rotational quantum number.

One can then construct Equation 4.4 that gives the y-coordinate as a function of an x-coordinate for the peaks in off-diagonal quadrants II and IV. This results in a curve that can be used to fit experimental 2D-IR data:

$$\omega_3 = \nu_0 + 10B_e + 4CB_e - 6\alpha_e C - \frac{3B_e^2}{\alpha_e} - 8\alpha_e - \alpha_e C^2 \quad 4.4$$

where:

$$C = \sqrt{\left(1 - \frac{B_e}{\alpha_e}\right)^2 - \left(\frac{\omega_1 - \nu_0}{\alpha_e}\right)} \quad 4.5$$

Equation 4.4 gives the off-diagonal values for ω_3 as a function of ω_1 on the 2D-IR axes. The peak positions in these coordinates were determined by fitting vertical slices across the data at $T_w = 1$ to Gaussian curves to identify the maxima, which are plotted in Figure 4.5. Equation 4.4 was then fitted to these data using ν_0 , B_e , and α_e as adjustable parameters. The calibration of the y-axis values in the 2D-IR instrument gives rise to the largest source of uncertainty in the fit, though these values are typically accurate to within 1-2 cm^{-1} . To circumvent this we used the crossing point of the on- and off-diagonal ridges (2351 cm^{-1}) as ν_0 and then allowed B_e and α_e to float in the fitting procedure. This yields $B_e = 0.39 \text{ cm}^{-1}$ and $\alpha_e = 0.0029 \text{ cm}^{-1}$, which are within 0.1% and 7% of the literature values for B_e and α_e , respectively.^{109, 110} In the absence of α_e there is no curvature in the off-

diagonal regions. However, the effect of this anharmonic correction term is amplified by terms in which α_e is a product with B_e . This analysis shows that these rotational-vibrational parameters can be determined with reasonable accuracy from a 2D-IR plot by simply fitting the curvature of the off-diagonal peaks, despite lacking the spectral resolution to resolve every individual rotational-vibrational transition as seen in the FTIR spectra.

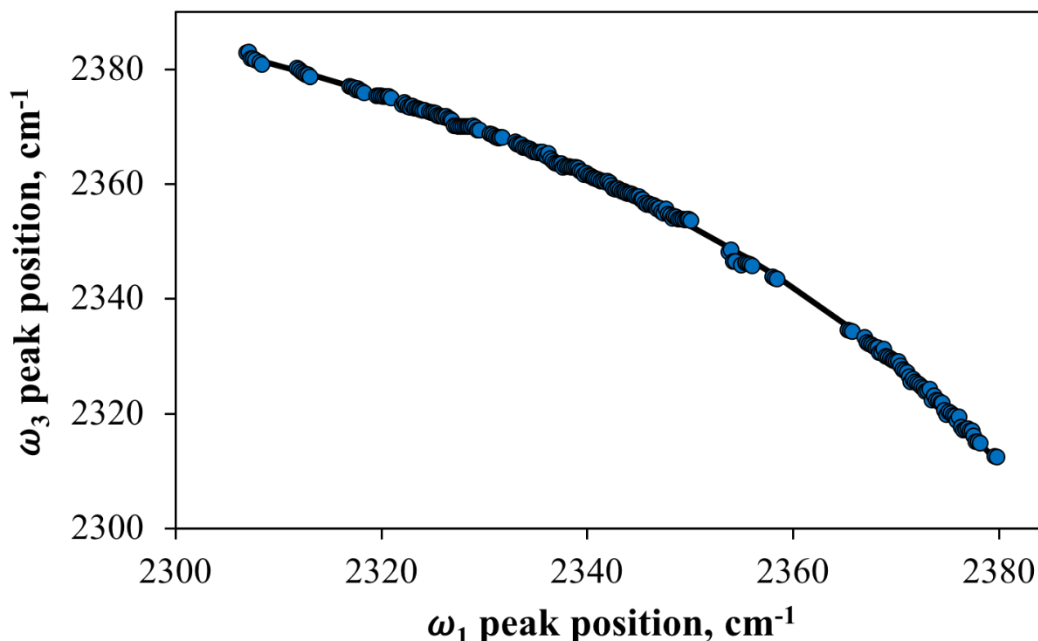


Figure 4.5. Off-diagonal peak positions extracted from the 2D-IR spectrum at $T_w = 1$ ps overlaid with Equation 3 (solid black line) using best fit parameters: $\nu_0 = 2351$ cm^{-1} , $B_e = 0.39$ cm^{-1} , $\alpha_e = 0.0029$ cm^{-1} .

A four wave mixing experiment results in 36 possible quantum pathways⁹⁹ though for simplicity this discussion will only focus on 6. Figure 4.2 a-d shows four different pathways which produce positive signal (red contours) representing ground state bleach. 2D-IR can prepare vibrationally excited state populations (blue contours) but is also sensitive to rotational-vibrational coherences (i.e. Figure 4.2e and f) which cannot be measured via FTIR. After the T_w waiting time, P/R coherences can be stimulated to emit

at either a P- or R-branch frequency and this will produce a new pair of off-diagonal peaks in quadrants II and IV. For example, an oscillator that experiences excitation through interaction with the P(2) transition could then be stimulated to emit vibrational echo at R(0) (Figure 4.2c) or R(2) (Figure 4.2f). Assuming B_e is orders of magnitude larger than α_e , these off-diagonal peaks are separated by approximately $4B_e$. Figure 4.6 shows that one can in fact resolve these peak pairs using a higher resolution grating at the detection side of the 2D-IR instrument. The peak separation here is 2.24 cm^{-1} on average, corresponding to $B_e = 0.56 \text{ cm}^{-1}$; this value does not match the literature as closely as that obtained by fitting the curvature of the full off-diagonal dataset, but it is still within a factor of two.

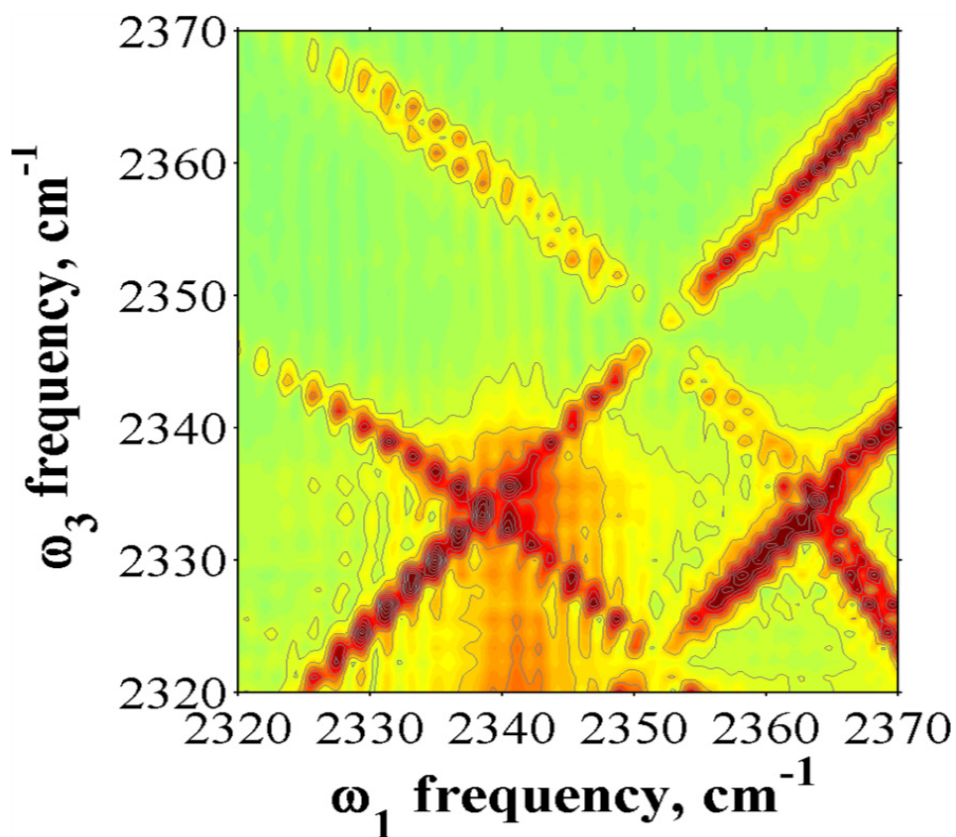


Figure 4.6. Absolute value 2D-IR spectrum at $T_w = 1 \text{ ps}$ for CO_2 gas measured with a higher resolution diffraction grating to identify peak twinning in the off-diagonal quadrants.

Understanding the 2D spectra of gaseous species becomes important when determining the origin of peaks for CO₂ dissolved in systems such as polymers. A sample with uneven thickness or crater-like defects may result in voids consisting of only CO₂ (g) and no polymer. If the beam focal volume is sufficiently large that these voids are probed during a measurement in addition to the polymeric sample, the resulting 2D spectrum will possess features belonging to both gas-phase and dissolved CO₂. The two species have distinctly different 2D spectra (Figure 4.7) and the gaseous signal can be subtracted with some success. However, subtraction methods are limited by factors such as laser drift that may occur between the acquisition of the sample spectrum and the gaseous spectrum.

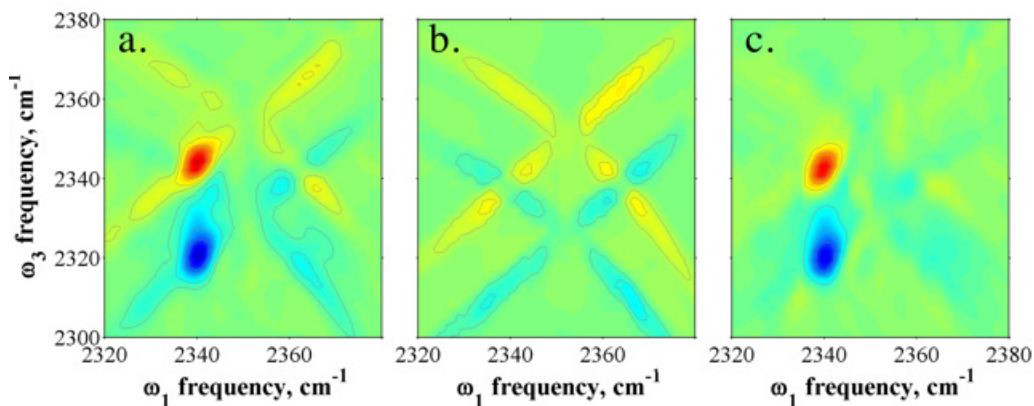


Figure 4.7. 2D-IR spectra at $T_w = 0.5$ ps for a) CO₂ gas dissolved inside PMMA, b) CO₂ gas by itself, and c) the resultant spectrum upon subtracting b from a.

Another topic worth addressing is the presence of a Fermi resonance in CO₂ between the symmetric stretch and doubly degenerate bending modes: At this point, it is unclear whether the Fermi resonance contributes dynamic behavior to the asymmetric stretch in the case of this work as well as Chapter 5. Prior findings by Brinzer et al. describing CO₂ dissolved inside ionic liquids demonstrate anharmonic coupling between the asymmetric stretch and the thermally excited bend, giving rise to a shoulder red-shifted from the

asymmetric stretch.¹⁰⁶ The authors note that the 2D-IR spectra possess unexplained spectral features that may have some contribution from Fermi resonances,¹¹¹ yet the frequency assignments do not match existing gas-phase data.¹¹¹ This only further emphasizes the need to study the ultrafast behavior of CO₂. An intimate knowledge of the CO₂ (g) spectrum also prevents one from ascribing gaseous artifacts as crosspeaks belonging to the dissolved sample. Improved sample preparation methods can almost entirely omit these artifacts and will be referenced in the next chapter, as well as a discussion on how CO₂ behaves when dissolved inside polymeric matrices.

4.5 Conclusions

Given the abundance of anthropogenic CO₂ and its perilous affects on the climate, it has become increasingly important to determine ways to somehow trap, separate, or repurpose excess CO₂. An understanding of the gas-phase dynamics is key to optimizing simulations that can then model and predict the dynamic behavior of separations. 2D-IR is uniquely suitable for measuring the dynamics of gaseous molecules undergoing collisions at ambient conditions. Herein I presented the 2D-IR spectra of CO₂ under ambient temperature and pressure to highlight spectral features arising from conservation of quantum mechanical states. The data did not exhibit spectral diffusion i.e J-scrambling due to the low gas pressures used, such that a significant amount of time elapses between each molecular collision. However, the curvature of off-diagonal features can be used in analyses that then yield rotational constants for gaseous systems even in the absence of high resolution instruments. These results also provided a foundation for understanding

the spectra of CO₂ dissolved inside more complex systems such as polymers, which will be described in the next chapter.

4.6 Full Set of 2D-IR Data

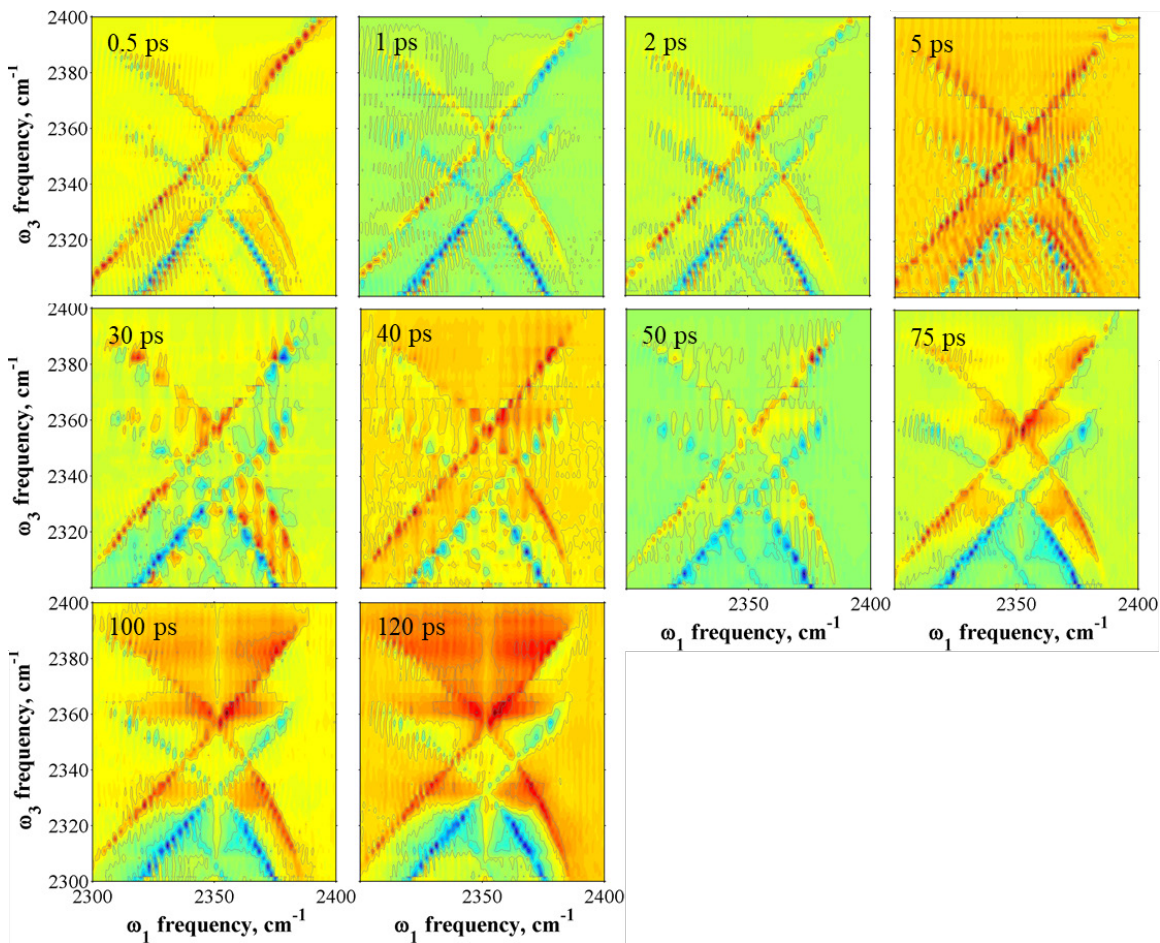


Figure 4.8. Full set of 2D-IR spectra probing the asymmetric stretch of gaseous CO₂ at a range of waiting time T_{ws} , as indicated in the upper left hand corner of each plot.

5. CO₂ Diffusion in Polymeric Matrices

Reprinted with permission from:

Pyles, C.G.; Gretz, G.M.; Spector, I.C.; Massari, A.M. “Ultrafast Dynamics Experienced by Carbon Dioxide Diffusing Through Polymer Matrices” *J. Phys. Chem. B.* **2021**, 125, 31, 8997-9004.

Copyright © 2021 American Chemical Society.

5.1 Chapter Summary

In this chapter, Fourier transform infrared, pump-probe polarization anisotropy, and two-dimensional infrared spectroscopies were used to study the steady-state and time-dependent behavior of carbon dioxide dissolved in three different polymer systems. Gas reorientation dynamics in poly(methyl methacrylate), poly(methyl acrylate), and poly(dimethylsiloxane) were sensitive to the nature of chemical interactions between the gas and polymer, as well as whether the polymer was in a glassy or rubbery phase. The homogeneous dynamics experienced by the asymmetric stretching vibration were found to be fastest for rubbery polymers with weak, non-specific gas-polymer interactions. Spectral diffusion was absent for the carbon dioxide vibrational mode in glassy poly(methyl methacrylate), but was activated for the chemically similar but rubbery poly(methyl acrylate). The vibrational dynamics are shown to have a direct correlation with the diffusivity of carbon dioxide through the polymer matrices.

5.2 Introduction

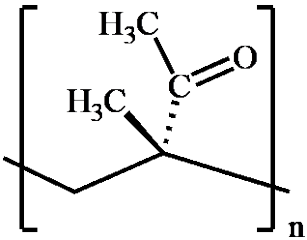
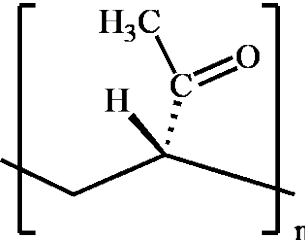
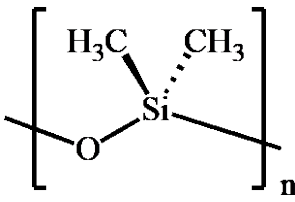
Carbon dioxide (CO₂) is the most abundant of anthropogenic greenhouse gases. In 2015, temperatures increased by nearly one degree Celsius relative to pre-industrial times due in part to CO₂. Carbon dioxide removal (CDR) technologies could help society mitigate further CO₂ emissions, but they are limited by their efficiency and scalability.^{112, 113} Mixed-matrix membranes are one promising CDR method. These systems often contain nanoporous CO₂ capturing agents (e.g zeolites or metal-organic frameworks) inside a gas-permeable polymer.^{114, 115} Gas diffusion through these membranes relies on polymer motions that span a wide range of time scales from tens to hundreds of picoseconds.^{23, 26,}

¹¹⁶⁻¹²⁰ In order to maximize their potential, methods must be developed that are capable of measuring and accurately modeling the ultrafast dynamics of the polymeric matrix and its interactions with CO₂ guests.

Gas diffusion is typically described at a molecular level by the free volume model in which the gas resides in microcavities whose boundaries are defined by polymer chains.^{116, 121-123} These volumes are dynamic and undergo structural fluctuations that can perturb the molecular structure of encapsulated gas molecules. These fluctuations depend on temperature and pressure, and exhibit phase transitions such as the glass transition temperature, T_g , above which segmental mobility is thermally activated.¹²⁴ Polymers below their characteristic T_g are referred to as glassy; those above T_g are termed rubbery. Microcavity structural dynamics are significantly enhanced above T_g .^{116, 121-123} Gas diffusion then proceeds by collective polymer motions that create transient conduits through which the gas molecule is able to move in stochastic jumps to reach an adjacent microcavity.^{116, 121-123}

In this study, I use IR pump-probe polarization anisotropy and two-dimensional infrared (2D-IR) spectroscopies to monitor the structural dynamics of several polymeric matrices as reported by a CO₂ guest that is encapsulated in and diffusing between polymeric microcavities. I compare the ultrafast vibrational and reorientational dynamics of the CO₂ asymmetric stretching mode (ν_3) in poly(methyl methacrylate) (PMMA), poly(methyl acrylate) (PMA), and poly(dimethylsiloxane) (PDMS) (Table 5.1).

Table 5.1. Chemical structure of polymers studied with glass transition temperatures (T_g) and mutual diffusion coefficients (D). The top row of T_g values are obtained from DSC measurements, and the bottom from the literature.

			
	poly(methyl methacrylate) (PMMA)	poly(methyl acrylate) (PMA)	poly(dimethylsiloxane) (PDMS)
T_g , °C	-124 (-123) ¹²⁵	-18 (3) ¹²⁵	93 (108) ¹²⁵
D , cm ² /s	2.43×10^{-9} at 298 K ¹²⁶	3.68×10^{-8} at 308 K ¹²⁷	2.6×10^{-5} at 308 K ¹¹⁶

This particular set of polymers offers a valuable comparative study since PMMA and PMA are chemically similar and are known to have specific interactions with CO₂,^{128, 129} but PMMA is glassy at room temperature while PMA is rubbery. PDMS is rubbery at room temperature like PMA,¹²⁵ but lacks the chemical specificity for CO₂ at the low pressures used herein.^{130, 131} The results demonstrate that time-dependent frequency fluctuations and molecular reorientation of CO₂ are directly correlated with the polymeric structural dynamics above the glass transition temperature. We also show that the ultrafast dynamics reported by the CO₂ guest are readily mapped onto the characteristic diffusivity of CO₂ in each of the polymer systems.

5.3 Materials & Methods

5.3.1 Polymeric Sample Preparation

Approximately 0.2 g of poly(methyl methacrylate) (PMMA, average $M_w \sim 15,000$, Sigma Aldrich) were dissolved in 5 mL of chloroform (99.9% purity, anhydrous, Acros Organics). After placing 1 mL of this solution on a CaF_2 window, the sample was spin-coated for 2 minutes at 200 RPM with an acceleration of 40 RPM/s. This resulted in a film with a thickness of approximately 45 μm . Two spin cast films pressed against each other were heated to 80 °C under a pressure of $\sim 0.6 \text{ N/cm}^2$ for 2-3 hours to eliminate air gaps between the film and windows caused by surface irregularities. The resulting sample was used for measurements at room temperature. Heated PMMA studies described later in this work required thicker films. 3 mL aliquots of the previously mentioned PMMA solution were drop cast on CaF_2 windows to create films with an estimated thickness of 150 μm . Drop cast films pressed against an additional CaF_2 window were then heated to 80 °C under a pressure of $\sim 0.6 \text{ N/cm}^2$ to eliminate air gaps.

Poly(methyl acrylate) (PMA, $\sim 40 \text{ wt. \%}$ in toluene, average $M_w \sim 40,000$, Sigma Aldrich) was dried under vacuum ($\sim 10^{-7}$ torr) for 72 hours to evaporate the toluene. The resulting polymer was highly viscous. A thin film was created by annealing a small volume of the polymer between two CaF_2 windows and exerting a pressure of $\sim 0.6 \text{ N/cm}^2$ with a spacer in place to create an 80 μm film.

Thin cross-linked poly(dimethylsiloxane) (PDMS) elastomer films were created with a Sylgard 184 silicone elastomer kit purchased from Dow Corning. The elastomer base (Sylgard-184A) and curing agent (Sylgard-184B) were combined in a 10:1 mass ratio. A

50 μm Teflon spacer and 25 μm Teflon spacer were stacked on top of a 3 mm thick CaF_2 window. After cutting a 1.5 cm diameter hole from the middle of each spacer, the elastomer mixture was doctor-bladed across the opening of the stacked spacers. The sample cured for 2 days at ambient conditions resulting in a transparent film roughly 75 μm in thickness. PDMS films retained elasticity and flexibility following the curing process.

During data acquisition, CaF_2 windows containing the polymer thin film samples sat inside a custom built gas-flow cell. Mass flow controllers (Unit Instruments Inc., UFC-1100) applied carbon dioxide (99% purity, Airgas) with a positive pressure ranging from $6\text{-}12 \times 10^{-4}$ atm across the thin films. The CO_2 asymmetric stretch (ν_3) provided spectroscopic evidence of gas dissolving within the thin films. Flow rates ranged between .006-.009 atm of positive pressure to provide roughly 100-200 milliOD of infrared absorption in each sample. All Fourier transform infrared (FTIR) spectra of polymer samples were collected with a Nicolet 6700 FTIR spectrometer (Thermo Scientific) as an average of 16 scans with a resolution of 1 cm^{-1} .

Differential Scanning Calorimetry (DSC) measurements of neat polymer samples prior to adhering to CaF_2 windows were collected on a TA Instruments Q1000. PMMA was heated from 40°C to 150°C at a rate of $10.00^\circ\text{C}/\text{min}$, then cycled back down to 40°C . PMA was heated from room temperature to 40°C , cooled to -50°C , then brought back to room temperature at a rate of $10.00^\circ\text{C}/\text{min}$. PDMS was heated from room temperature to 40°C , cooled to -160°C , then brought back to room temperature at a rate of $10.00^\circ\text{C}/\text{min}$.

5.3.2 Ultrafast Data Collection (2D-IR, pump probe anisotropy)

The laser instrumentation for pump probe and 2D-IR measurements has been described previously^{52, 85} and in Chapter 2 of this thesis. The mid-IR pulses were centered at approximately 2340 cm^{-1} corresponding to the CO_2 asymmetric stretching region for all spectroscopic measurements. Failure to purge the laser enclosure allowed atmospheric CO_2 to absorb $\sim 90\%$ of the generated mid-IR and eliminated all signal. Thus, the entire instrument was sealed and continuously purged with dry N_2 during all data collection.

For 2D-IR measurements, the mid-IR centered at 2340 cm^{-1} was split into three paths ($\sim 1\text{ }\mu\text{J}$ per pulse) and pointed onto the sample in the BOXCARS geometry.⁵³ The vibrational echo generated by the sample was interfered with a local oscillator ($0.3\text{-}0.5\text{ nJ}$ per pulse). The x- or ω_1 -axis was created by varying the delay time between the first two pulses and then taking the Fourier transform of the result. The y- or ω_3 -axis was optically Fourier transformed by spectrally resolving the heterodyned signal in a 0.32 m monochromator (150 line/mm grating, resolution 2 cm^{-1}). Signal was detected with a liquid N_2 cooled 64-element mercury cadmium telluride (MCT) array detector (Infrared Associates, Inc.) The data were analyzed by the centerline slope (CLS) method.^{132, 133} Due to the narrowness of the 2D-IR peaks ($\sim 5\text{ cm}^{-1}$), the centerline was defined by fitting Gaussian slices parallel to the ω_1 axis instead of the ω_3 axis, then taking the reciprocal of the resultant slope.

Pump-probe anisotropy measurements were performed by splitting the aforementioned mid-IR into two beam paths, denoted the pump and probe. The pump beam transmitted through a $\lambda/2$ waveplate (Altechna, 4500 nm) to rotate the p-polarized light to 45° . The probe beam was kept p-polarized. A mid-IR polarizer was placed in the pump beam path

immediately before the sample and set to 45° . An analyzer polarizer placed immediately after the sample in the probe path was rotated -45° and $+45^\circ$ relative to the pump, to resolve parallel ($S_{\parallel}(t)$) and perpendicular ($S_{\perp}(t)$) contributions to the population decay. A final polarizer was placed immediately before the monochromator entrance slit and rotated to maximize probe transmission without the analyzer in place. After installing the analyzer, the final polarizer was rotated \pm a few degrees to ensure the probe intensity through the sample (without the pump) was equivalent for the parallel and perpendicular orientations.³⁷

¹³⁴ Polarization anisotropy data were collected out to 105 ps for analysis.

The parallel ($S_{\parallel}(t)$) and perpendicular ($S_{\perp}(t)$) signals give rise to the population decay through the following relation:³⁷

$$P(t) = \frac{S_{\parallel}(t) + S_{\perp}(t)}{3} \quad 5.1$$

The orientational dynamics can be characterized by the polarization anisotropy, $r(t)$:³⁷

$$r(t) = \frac{S_{\parallel}(t) - S_{\perp}(t)}{S_{\parallel}(t) + 2S_{\perp}(t)} \quad 5.2$$

Wobbling in a cone analysis was conducted as described on page 11 in section 1.3.4

5.4 Results and Discussion

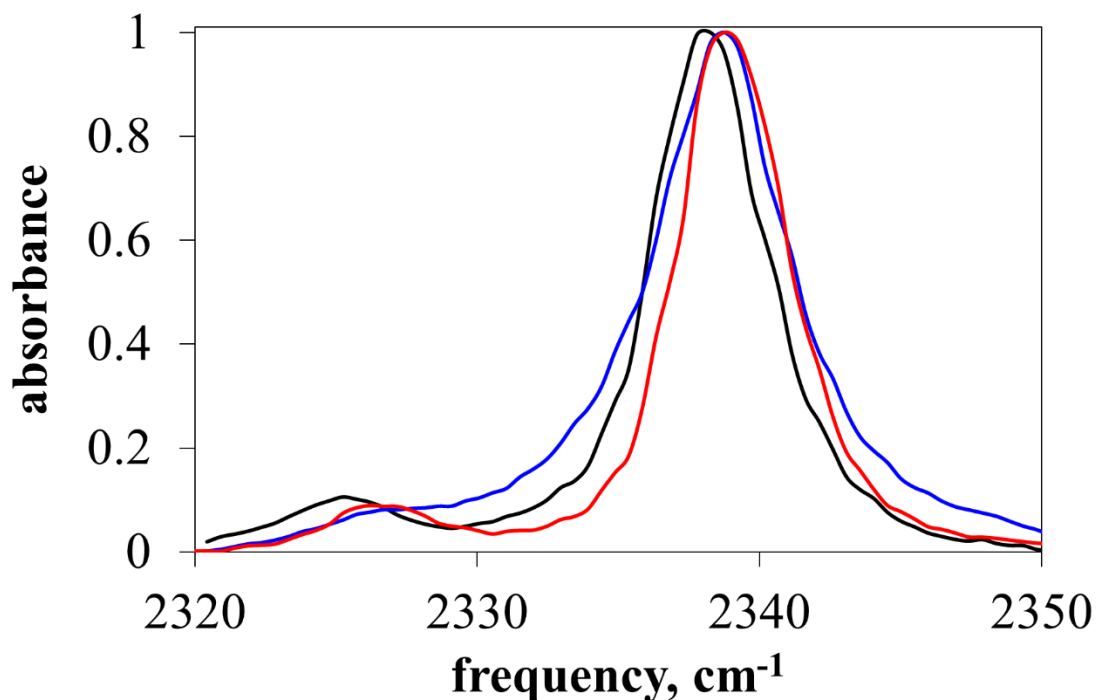


Figure 5.1. Normalized FTIR spectra of the CO₂ 0-1 asymmetric stretch in PMMA (black), PMA (red), and PDMS (blue).

Figure 5.1 shows FTIR spectra of the asymmetric stretching vibration (ν_3) of CO₂ dissolved in thin films of PMMA, PMA, and PDMS. The spectra are characteristic of CO₂ dissolved in the condensed-phase, lacking all of the rotational-vibrational features that are typically associated with gas-phase molecules. The CO₂ solute is solvated by interactions with the polymeric microcavity rather than existing as a gas-phase molecule in small voids within the polymer film. These dynamic interactions facilitate gas diffusion through the polymer and lead to the vibrational dynamics described below. The frequency of ν_3 ranges 2338 to 2339 cm⁻¹ in these three polymers, and serves as a molecular probe of the chemical structure and dynamics. It has been noted by others that the asymmetric stretch is solvatochromic and readily senses differing chemical environments.¹⁰⁶ The three FTIR

spectra were fit to pseudo-Voigt functions to obtain peak centers and full width at half maximum (FWHM) values (Table 5.2).

Table 5.2 Values extracted from a pseudo-Voigt fit to the FTIR spectra in Figure 5.1.

polymer	peak center (cm⁻¹)	combination band shift (cm⁻¹)	FWHM (cm⁻¹)	Gaussian	Lorentzian
PMMA	2338.2	13.1	4.8	32 %	68 %
	2325.1		4.5	60 %	40 %
PMA	2339.0	12.4	4.6	46 %	54 %
	2326.6		4.0	92 %	8 %
PDMS	2338.6	10.6	5.7	7 %	93 %
	2328.0		7.1	99 %	1 %

The peak shapes in PMA and PMMA are identical except for their center frequencies. The ν_3 of CO₂ in PDMS is similar in frequency to the methacrylate polymers but slightly wider and with a notably higher Lorentzian character. All three spectra also exhibit a small red-shifted peak that has been previously assigned to a vibrational hot band originating from coupling of ν_3 to a thermally excited bending mode near 667 cm⁻¹.^{106, 135} The amplitude and frequency shift of this hot band from the ν_3 mode is reflective of the coupling strength between the stretch and bend vibrations.^{106, 5, 34, 135} Table 5.2 shows that this combination band shift is 13.1, 12.4, and 10.6 cm⁻¹ for CO₂ solvated in PMMA, PMA, and PDMS, respectively. This stronger coupling of the stretch to the bending motion will be shown to have a direct impact on the vibrational dynamics.

The subtle differences in FTIR peak shapes arise from a combination of homogeneous

and inhomogeneous broadening experienced by CO₂ in these three polymeric environments. These broadening processes are dynamic in nature: homogeneous broadening originates from ultrafast vibrational population relaxation (T_1), molecular reorientation (T_{or}), and pure dephasing (T_2^*) within the polymer matrices, whereas inhomogeneous broadening is born out of spectral diffusion dynamics over a wide range of time scales.^{107, 136} The latter dynamics can range from ultrafast frequency fluctuations caused by the surrounding chemical environments to slow, pseudo-static ensembles that do not interconvert on the time scale of these measurements. The remainder of this study will focus on decomposing the seemingly similar FTIR line shapes in Figure 5.1 to reveal dramatic differences in their underlying dynamics.

Population and orientational dynamics were characterized by polarization-controlled IR pump-probe measurements on the CO₂ ν_3 mode in PMA, PMMA, and PDMS. Figure 5.2 shows the ν_3 population relaxation for CO₂ in PMMA, PMA, and PDMS. It is clear that there is more than one dynamic process captured in these decays. All three systems were best modeled with a biexponential decay; the best fit parameters are tabulated in Table 5.3. The longer time constant obtained from each biexponential fit was ascribed to population relaxation, T_1 .

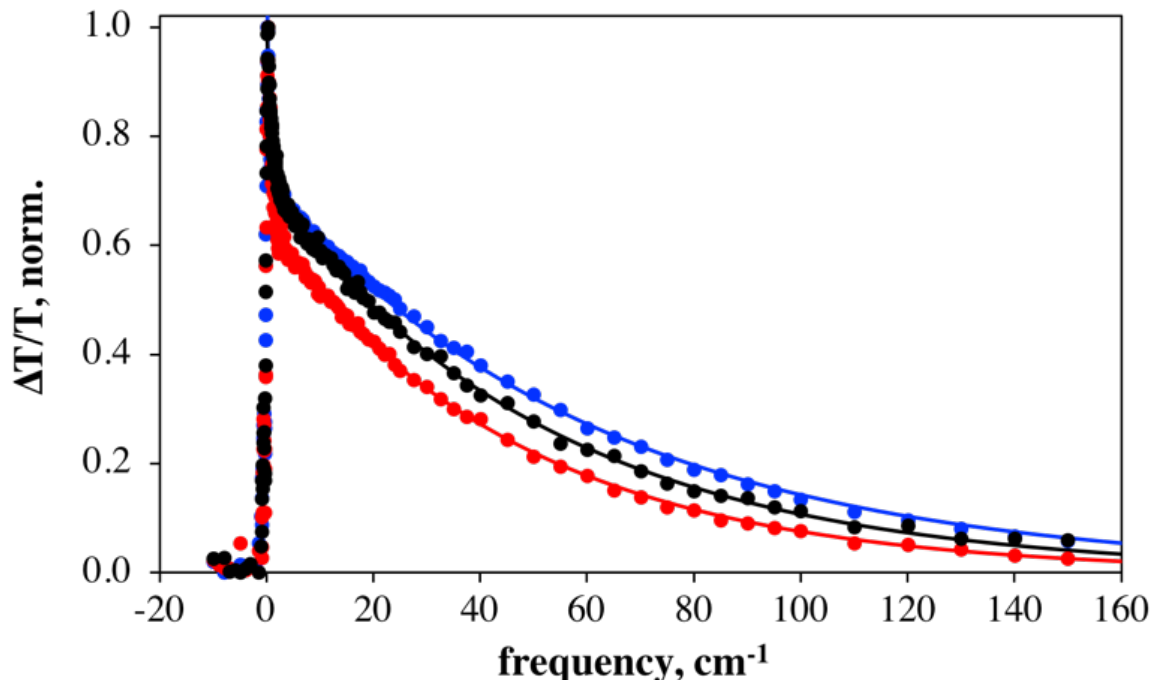


Figure 5.2. Normalized population decays measured for the 0-1 ν_3 for CO₂ in PMMA (black), PMA (red), and PDMS (blue). Markers show experimental data, solid lines show best biexponential fit.

Table 5.3. Population and orientational decay time constants for CO₂ in PMA, PMMA, and PDMS.

polymer	vibrational lifetime (T_1) (ps)	τ_{fast} (ps)	$r(t)$ decay time, (ps)	D_c^{-1} , cone diffusion constant (ps)
PMMA	53 (± 1.1)	0.88 (± 0.12)	1.3 (± 1.3)	25 (± 12)
PMA	47 (± 1.5)	0.82 (± 0.072)	0.66 (± 0.45)	7.9 (± 0.82)
PDMS	62 (± 0.98)	0.24 (± 0.016)	0.67 (± 0.11)	5.8 (± 0.53)

*Standard error obtained via fitting time constants with a 95% confidence interval

CO₂ is a small symmetric molecule with only four vibrational modes. Relaxation of ν_3 proceeds by intramolecular redistribution (IVR) into these few modes and intermolecular energy transfer to accepting modes and phonons in the polymeric matrices in which it is solvated. Previous studies of the asymmetric stretch relaxation in ionic liquids have shown that relaxation proceeds through anharmonic coupling to the CO₂ bending vibration at 667

cm^{-1} .¹⁰⁶ The ν_3 lifetimes for these three different polymer environments demonstrate that the relaxation time is approximately 10 ps faster in the methacrylate polymers (PMA and PMMA) than in PDMS. This is consistent with the stronger coupling shown by the larger peak splitting between the asymmetric stretch and hot band vibrations in the FTIR and Table 5.2. Relaxation likely proceeds by IVR and transfer to the CO_2 bending mode plus a phonon to conserve energy in a mechanism that has slight differences in coupling between CO_2 and the respective polymers.^{65, 137, 138} In order to better ascertain the origin of the τ_{fast} component in the pump probe decays, we then performed pump probe polarization anisotropy (Figure 5.3).

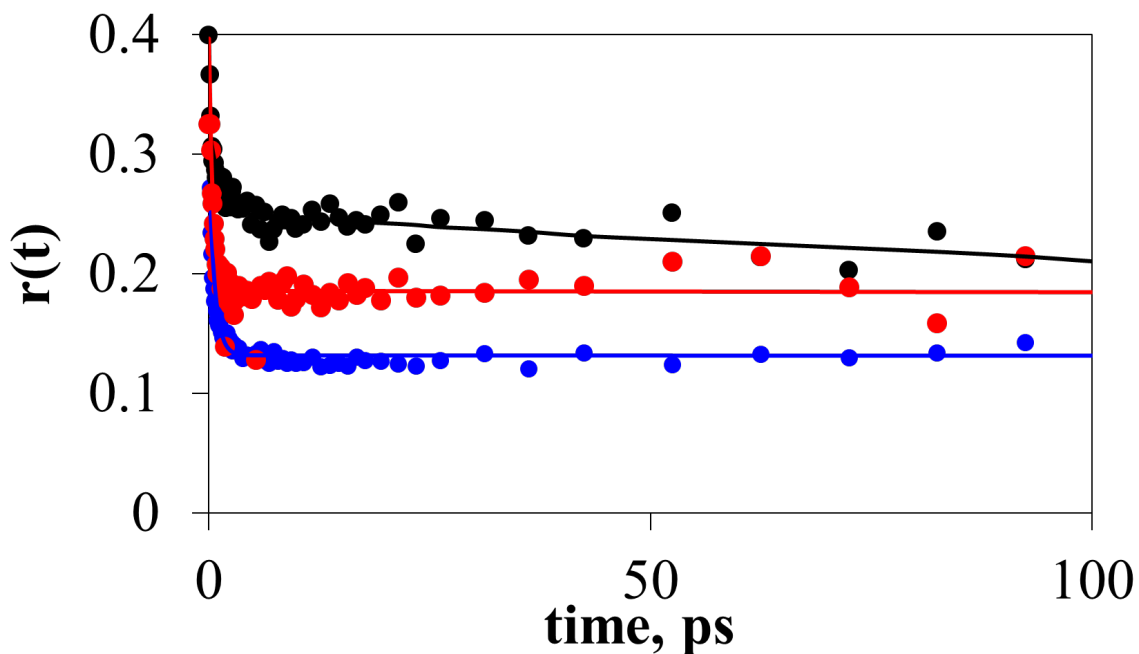


Figure 5.3. Polarization anisotropy decays for PMMA (black), PMA (red), and PDMS (blue). Overlaid solid lines are biexponential fits.

Polarization anisotropy, $r(t)$, for the ν_3 mode reveals that CO_2 rapidly reorients while solvated in microcavities in all three polymer environments. Each anisotropy decay was successfully fit by a biexponential function including a fast exponential decay with a time

constant of less than 2 ps (Table 5.3). An exceptionally long time constant was required to capture molecular reorientation taking place on time scales longer than we are able to resolve.

Table 5.4. Full results of biexponential fits for pump probe anisotropy of CO₂ dissolved in the three polymer systems.

Sample	τ_1 (ps)	amp. 1	% Fast	τ_2 (ps)	amp. 2	% Slow
PMA, CO ₂ (g)	0.66 (± 0.45)	0.11 (± 0.12)	38%	1363 (± 1912)	0.18 (± 0.0041)	62%
PMMA, CO ₂ (g)	1.3 (± 1.3)	0.080 (± 0.050)	24%	680 (± 670)	0.25 (± 0.016)	76%
PDMS, CO ₂ (g)	0.67 (± 0.11)	0.16 (± 0.018)	55%	47000 ($\pm 64E4$)	0.13 (± 0.0031)	45%

An offset in the $r(t)$ decay persists at long times for all three samples that increases in order from PDMS < PMA < PMMA. This is likely due to interactions between the CO₂ probe and polymer backbone that prevent it from reorienting, and the strength of those interactions increases from PDMS < PMA < PMMA. Previous work has shown that the ν_2 bend degeneracy is broken through Lewis acid-base type interactions between the carbonyl functional groups in PMMA and CO₂, which are also present in PMA.^{128, 129} Although CO₂ can perturb the methyl chains in PDMS at pressures exceeding approximately 1-2 MPa, the pressures used herein are orders of magnitude too small for such interactions to be readily observable. When these high pressures are used, the ν_3 stretch red shifts from 2338 cm⁻¹ by up to 3 cm⁻¹.^{130, 131} The lack of specific chemical interactions occurring in PDMS for the pressures of CO₂ used give it the smallest $r(t)$ offset. Figure 5.3 also implies that the interaction is stronger between CO₂ and PMMA than it is between CO₂ and PMA, as

shown by the larger $r(t)$ offset at long waiting times. As stated above, at room temperature, PMA is above its T_g whereas PMMA is glassy. We hypothesize that the interaction strength between CO_2 and PMA is weakened by the structural dynamics experienced by the gas molecule in the rubbery polymer microcavity.

The $r(t)$ data were analyzed by a wobbling-in-a-cone model in which the vibrational transition dipole is envisioned to reorient rapidly within a limited range of angles (the cone angle, θ_c), and more completely on longer time scales.^{37, 139, 140} Using the time constants from the biexponential fits to $r(t)$, this treatment allows one to determine the cone diffusion constant, D_c , which reflects the time required for the dipole wobbling inside the cone to explore its full range of angles. Fitting the longer-lived contribution of $r(t)$ extracts D_m^{-1} , the inverse orientational diffusion constant. This constant characterizes the time scale required for the entire cone to reorient, upon which $r(t)$ decays to zero. The D_c values for CO_2 in the three polymers are tabulated in Table 5.3 and show that reorientation in PMA is more similar to PDMS. The full parameter list from wobbling-in-a-cone analysis is provided in Table 5.5.

Table 5.5. Parameters obtained from wobbling-in-a-cone analysis of CO_2 in the three polymers.

polymer	θ_{in}	θ_{tot}	D_c^{-1}	D_m^{-1}
PMMA	21 (± 12)	31 (± 17)	25 (± 12)	2.5×10^{-4} ($\pm 1.2 \times 10^{-4}$)
PMA	26 (± 16)	40 (± 0.50)	7.9 (± 0.82)	1.3×10^{-4} ($\pm 7.7 \times 10^{-5}$)
PDMS	27 (± 3)	47 (± 0.45)	5.8 (± 0.53)	3.6×10^{-6} ($\pm 3.3 \times 10^{-6}$)

It is surprising that the similarity in reorientation dynamics is found between PMA and PDMS, rather than with the chemically similar PMMA. Though localized chemical interactions may hinder the cone diffusion, DSC measurements (Table 5.1, Figure 5.4) indicate that PMMA prepared for this study encounters T_g at 93 °C, whereas the transition occurs at -18 °C for PMA and -124 °C for PDMS. Thus, at room temperature where the spectroscopic data presented above were collected, PMMA is in a glassy state, while PMA and PDMS are both in a rubbery state. This demonstrates that polymer structural motions above T_g exert a stronger influence on CO₂ reorientation dynamics than the chemical interactions with the carbonyl groups in PMMA and PMA.

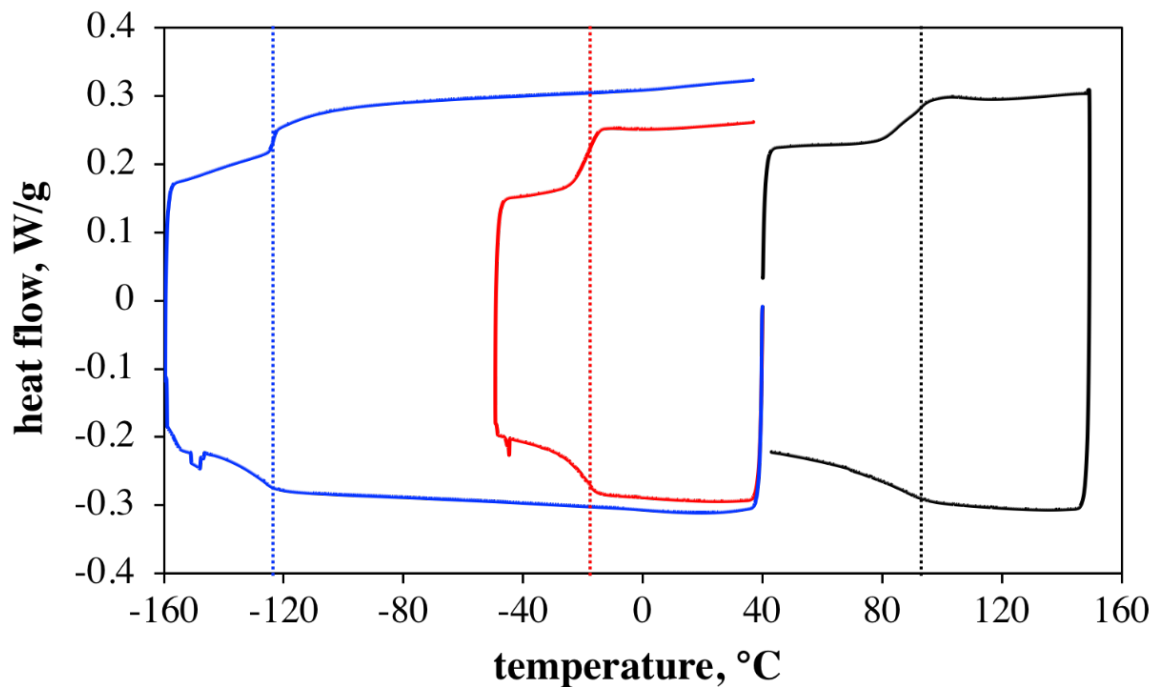


Figure 5.4. DSC measurements indicate the PDMS sample (blue) encounters the glass transition at -124°C, whereas this transition occurs at -18°C for PMA (red) and 93°C for PMMA (black). Literature values for transitions are shown in Table 5.1 in parentheses.

2D-IR spectroscopy was used to further probe the polymer dynamics experienced by the CO₂ guest and to disentangle the homogeneous and inhomogeneous contributions to the IR linewidth.^{107, 141-145} Figure 5.5 shows the 2D-IR spectra of CO₂ in PMMA, PMA, and PDMS thin films. The ω_1 axis represents the frequencies of IR light used to excite the CO₂ molecule; the ω_3 axis represents the emitted IR frequencies of CO₂ molecules after interacting with their polymeric environments for a specified waiting time, T_w . The red contours in Figure 5.5 indicate positive signal belonging to ground state bleach of the $\nu=0-1$ vibrational transition. Taking a slice along the diagonal of the 0-1 peak would reveal an absorption spectrum that is nearly identical to the FTIR spectrum. Blue contours depict negative signal corresponding to excited state absorption due to a $\nu=1-2$ transition. The anharmonicity of the vibrational mode being probed dictates the separation between the centers of the 0-1 and 1-2 peaks along the ω_3 axis and is measured here to be 24.8 cm⁻¹.

A first observation from Figure 5.5 is that the 2D-IR spectra in these three polymers are quite different despite their relatively similar FTIR spectra. At early waiting times ($T_w = 0.5$ ps), the ν_3 peaks in the PMMA and PMA samples (Figure 5.5a and Figure 5.5c, respectively) are elongated along the diagonal. Fluctuations of the polymer surroundings during the waiting time of 0.5 ps perturb the ν_3 mode so that it is stimulated to emit different frequencies of light than it had initially absorbed. This decorrelation of vibrational oscillators, or spectral diffusion, has not occurred to an appreciable degree even after 10 ps for PMMA or PMA (Figures Figure 5.5b and Figure 5.5d, respectively). In PDMS, however, even at $T_w = 0.5$ ps, the 0-1 and 1-2 contours have already taken on a rounded

shape indicative of nearly complete spectral diffusion (Figure 5.5e). At 10 ps, the PDMS peak does not qualitatively appear to grow rounder (Figure 5.5f).

Off-diagonal peaks are present between the on-diagonal asymmetric stretch and hot band peak for all three polymers due to energetic exchange between the CO₂ bend and the asymmetric stretch.¹⁰⁶ Brinzer and coworkers showed through simulations that the rate of random thermal fluctuation between the ground and first excited bending state will dictate the appearance of the 2D-IR spectrum.¹⁰⁶ In previous studies, these off-diagonal features have been shown to grow in with T_w , indicating thermal exchange with the bending mode on a time scale that is comparable to the waiting times.^{5, 34, 106, 135} A thorough analysis of the off-diagonal intensity in these 2D-IR spectra show that the peaks actually do not grow in intensity with T_w (Figure 5.6) for any of the polymeric systems studied here.

In the case of PDMS, off-diagonal peaks are present and do not increase with T_w ; In the cases of PMMA and PMA, off-diagonal peaks are not clearly resolved and show no evidence of growing in. Therefore energy is transferred quickly compared to the measurement time scale and peaks are present even at the shortest waiting times. This rapid exchange of thermal energy with the bending mode causes off-diagonal peaks to have constant normalized amplitude at all T_w s. Qualitative comparisons of the 2D-IR spectra show that spectral diffusion of the CO₂ ν_3 mode in PMA and PMMA proceeds slowly in comparison to PDMS. The rate at which spectral diffusion occurs can be quantified by extracting the center line slope (CLS) as a function of T_w .⁴⁸

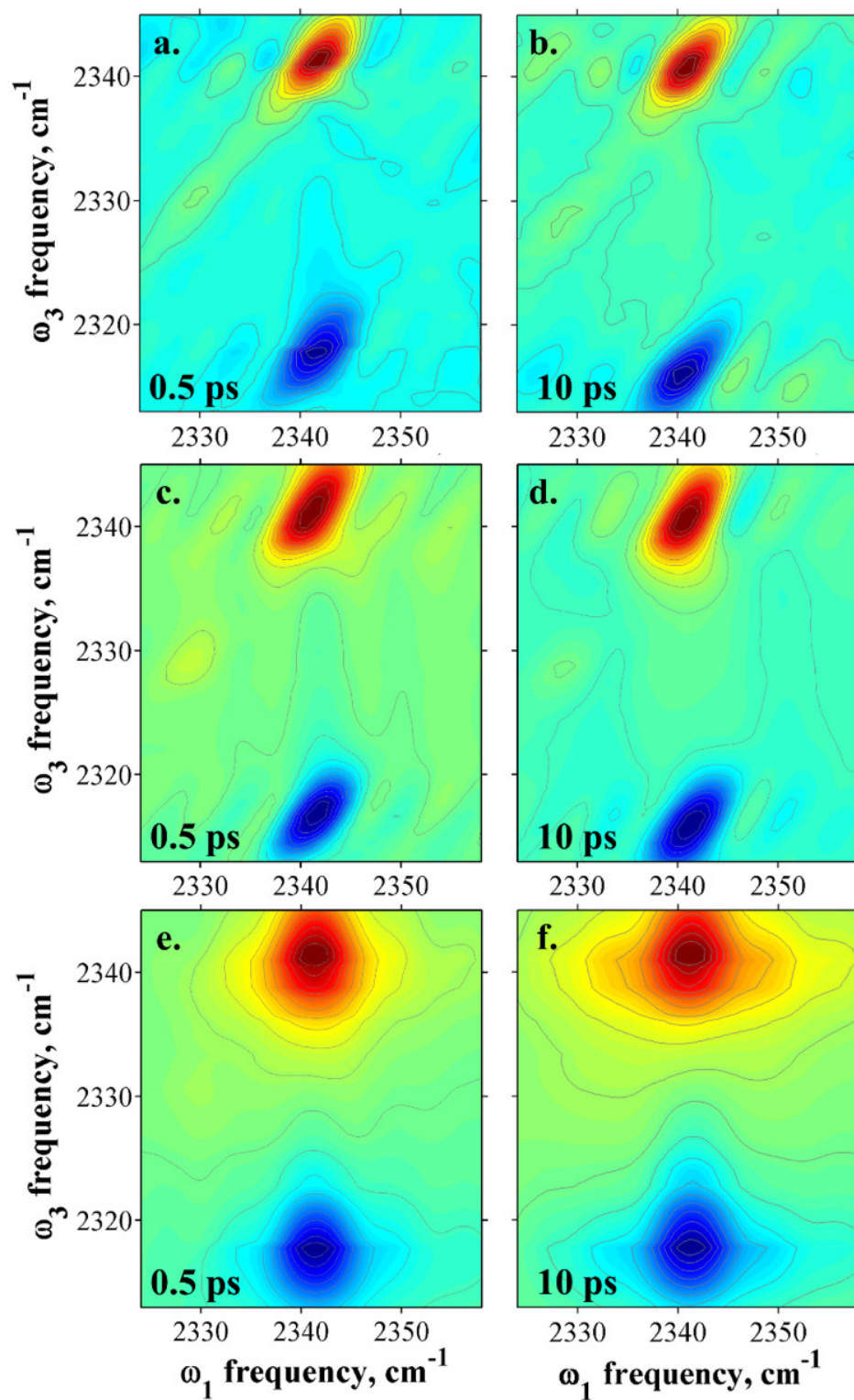


Figure 5.5. 2D-IR spectra of the CO₂ v₃ mode, dissolved in PMMA (a, b), PMA (c, d), and PDMS (e, f) at $T_w = 0.5$ ps (left column) and $T_w = 10$ ps (right column).

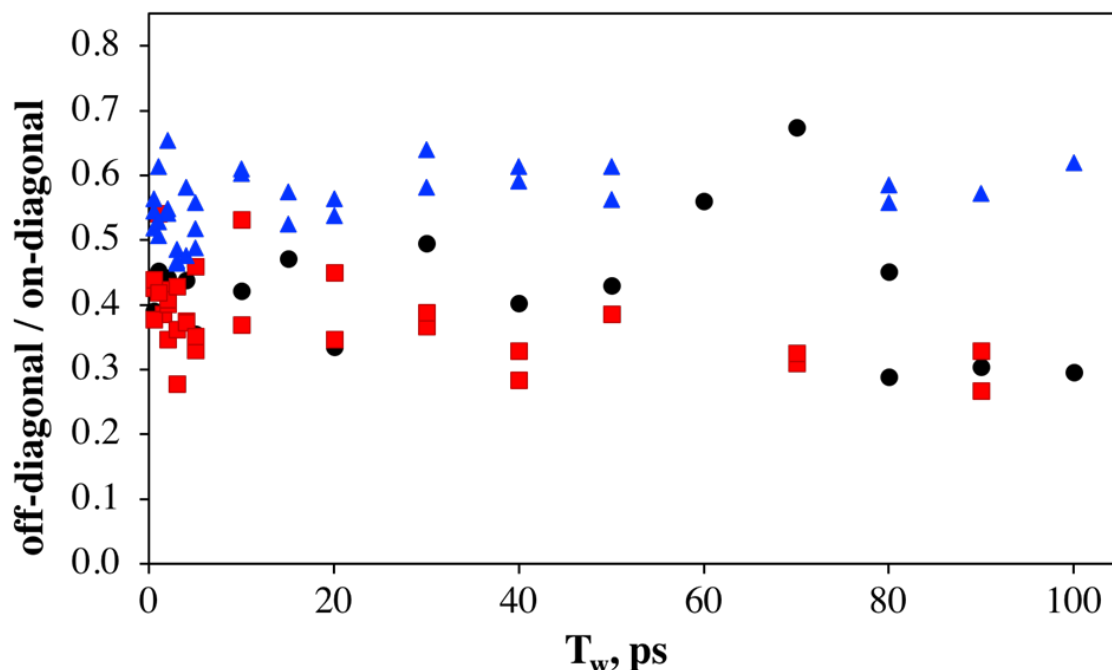


Figure 5.6. Off-diagonal intensity normalized by the on-diagonal intensity at the emission frequency for PMMA (black circles), PMA (red squares), and PDMS (blue triangles). The data demonstrate that the off-diagonal intensity does not grow in as T_w is increased for any of the polymeric systems.

A CLS value of one represents a completely correlated set of vibrational probes. The CLS becomes zero when vibrational oscillators completely de-correlate over the elapsed waiting time. The CLS values are plotted in Figure 5.7 for the 2D-IR spectra collected from several sample scans for each of the three polymer types. The fit parameters are tabulated in Table 5.6.

PDMS has a minimal CLS offset at long T_w s compared to those exhibited by PMA and PMMA. The near baseline CLS indicates that the ν_3 mode on CO_2 in PDMS experiences relatively fast structural dynamics that perturb its frequency and lead to complete spectral diffusion. The CLS values show that CO_2 in PDMS experiences the most decorrelation of its oscillator frequencies, just as it showed the most decorrelation of dipole orientations in Figure 5.3.

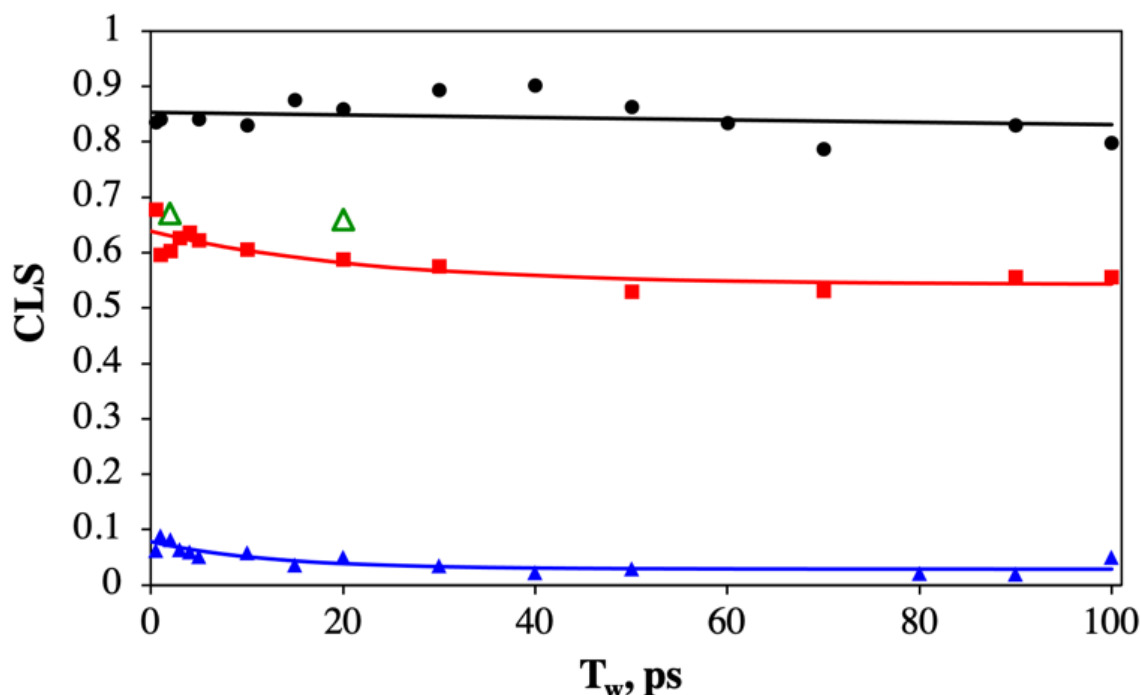


Figure 5.7. CLS as a function of T_w for PMMA (black circles), PMA (red squares), and PDMS (blue triangles) measured at 25 °C. Each set of data were fit to a single exponential with an offset. Open green triangle markers show CLS values measured in PMMA sample heated to 150 °C.

Table 5.6. Amplitudes (A_1) and time constants (τ_1) for single exponential decay plus constant (A_0) fit to CLS values as a function of T_w .

Sample	A_1	τ_1 (ps)	A_0
PMMA	0.19 (± 40)	825 (± 10)	0.66 (± 40)
PMA	0.096 (± 0.016)	22 (± 12)	0.54 (± 0.01)
PDMS	0.049 (± 0.007)	12 (± 5)	0.029 (± 0.005)

The CLS offsets are higher for PMMA and PMA, with PMMA showing almost no spectral diffusion over 100 ps. Recalling that a fundamental difference between these chemically similar polymers is that PMA is rubbery while PMMA is glassy at room temperature, we hypothesized that the thermally activated dynamics in PMA are the source of CO₂ spectral diffusion dynamics. To test this hypothesis, the PMMA sample was heated above T_g to 150 °C and 2D-IR spectra were collected (Figure 5.8). The CLS values

extracted from these 2D-IR spectra are shown as green triangles in Figure 5.7. As expected, the data lay on top of the CLS values for PMA when the PMMA sample is above T_g . Upon activating segmental mobility above T_g , the two methacrylate polymers have remarkably similar spectral diffusion.

Comparing the time scales of the CLS decays in Table 5.6 to those of polarization anisotropy in Table 5.2, we must further conclude that the vibrational dynamics captured in the CLS do not originate from CO_2 reorientation. For one thing, the fast reorientation time constants obtained from the $r(t)$ fits are an order of magnitude faster than any of those obtained from the CLS. Furthermore, CO_2 reorientation in PDMS is quite similar to PMA but the two systems have dramatically different time constants for spectral diffusion. Additionally, the $r(t)$ in PDMS has a nonnegligible offset of ~ 0.1 at tens of picoseconds (where $r(t)$ can have a maximum value of 0.4), yet the CLS offset is nearly at the baseline after tens of picoseconds. Therefore, CO_2 probes in PDMS have almost completely sampled their range of possible vibrational energies, despite incomplete reorientation.

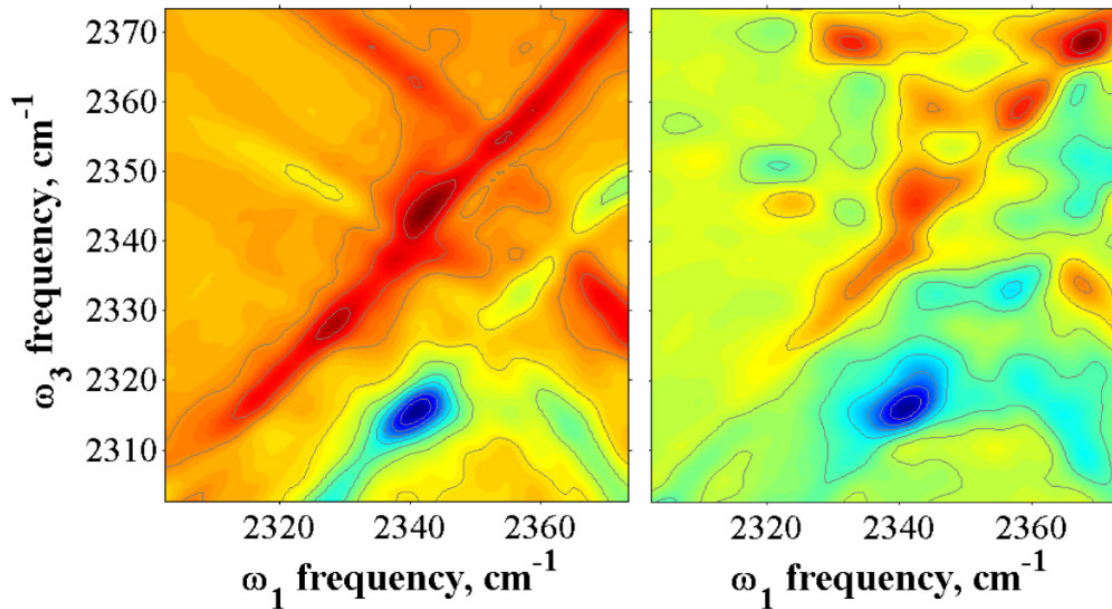


Figure 5.8. 2D-IR spectra of PMMA heated above its T_g mimic those of PMA which is well beyond its T_g at room temperature. Shown is $T_w = 0.5$ ps (upper left) and $T_w = 20$ ps (upper right). The 1-2 transition was chosen for analysis due to on-diagonal scatter and partial gas phase contribution.

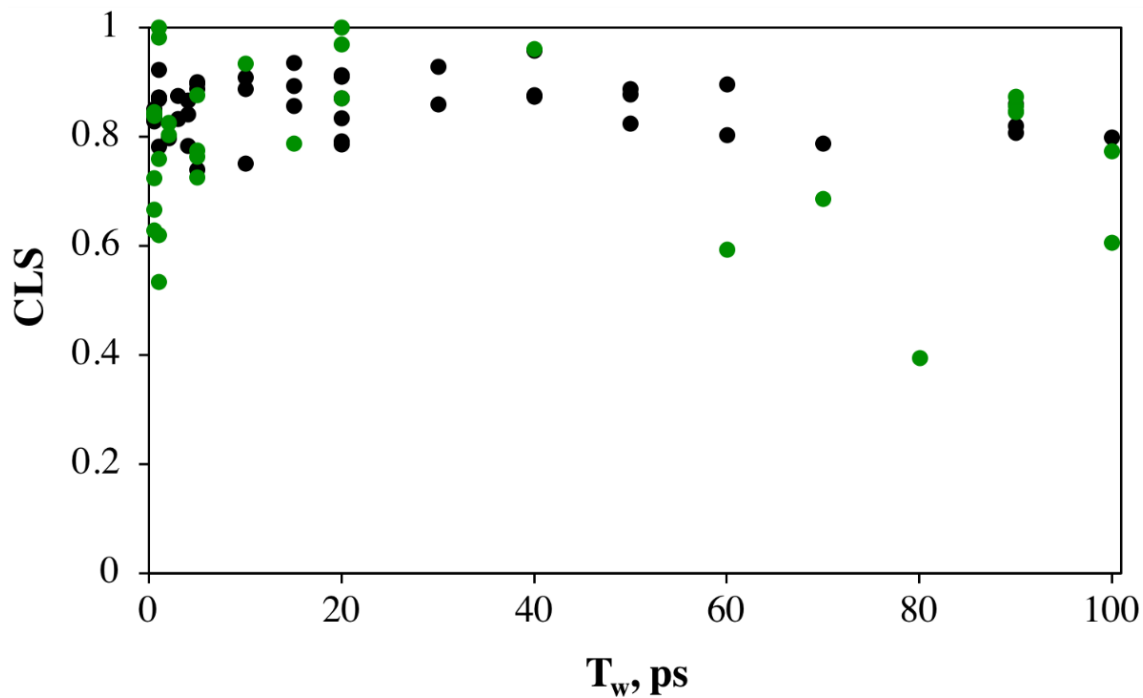


Figure 5.9. CLS plotted as a function of T_w for the 0-1 (black) and 1-2 (green) peak associated with the asymmetric stretch of CO_2 in PMMA, collected at room temperature. Though the 1-2 has more noise, the data points follow a similar trend at long T_w s. These values were tabulated to confirm the validity of comparing the CLS values of the 1-2 in heated PMMA to those of the 0-1 in room temperature PMA.

The 2D-IR spectra can be used to determine the amplitudes and time scales for homogeneous and inhomogeneous contributions to the linear FTIR spectra in Figure 5.1 through the frequency-frequency correlation function (FFCF).^{48, 107} The calculated FFCF parameters are shown in Table 5.7. T_2 represents the homogeneous dephasing time for each sample and encompasses pure dephasing, molecular reorientation, and population decay. Γ expresses the homogeneous contribution to linewidth. For the tabulated values shown below, τ_1 gives the time scale on which inhomogeneous processes occur that yield the Δ_1 contribution to the overall peak width. Any inhomogeneous processes that are too slow to be captured by τ_1 become contributors toward the inhomogeneous offset, Δ_0 .

Table 5.7. Parameters obtained from the FFCF fit of the CO₂ ν_3 mode when dissolved in PDMS, PMMA, and PMA.

Sample	T_2 (ps)	Γ (cm⁻¹)	τ_1 (ps)	Δ_1 (cm⁻¹)	Δ_0 (cm⁻¹)
PMMA	17 (± 4)	0.6 (± 0.2)	825 (± 10)	0.8 (± 0.5)	1.7 (± 0.4)
PMA	11 (± 2)	1.0 (± 0.2)	22 (± 12)	0.7 (± 0.2)	1.6 (± 0.1)
PDMS	7.8 (± 0.6)	1.4 (± 0.1)	12 (± 7)	1.5 (± 0.6)	1 (± 0.3)

The homogeneous portions of the line shapes, get progressively larger from PMMA < PMA < PDMS. Neglecting the vibrational lifetime for CO₂ (which is relatively long in all three polymer systems and has a minimal contribution to the homogeneous linewidth), the progression of Γ shows that the fast, homogeneous frequency fluctuations experienced by CO₂ are fastest in PDMS, which is above its T_g and has only weak non-specific interactions with the gas molecules. In contrast, PMMA, which is below its T_g and has stronger intermolecular interactions with CO₂, has only unresolvably fast dynamics in Γ and unresolvably slow dynamics in the inhomogeneous terms in Table 5.7. From the D_c^{-1} values

calculated previously, we know that orientational contribution to Γ will also increase in order of PMMA < PMA < PDMS due to the wobbling cone diffusion becoming faster. However, the contribution is most likely small in magnitude compared to the aforementioned frequency fluctuations. As shown above, dipole reorientation is not a prerequisite for spectral diffusion.

Interestingly, we again find that CO₂ spectral diffusion in PMA more closely resembles that of PDMS rather than the chemically similar PMMA. It appears that the segmental motions that are activated in PMA above its T_g contribute to the ν_3 frequency fluctuations that lead to spectral diffusion on the time scale of 22 ps. This time scale has overlapping error bars with the 12 ps frequency fluctuations in PDMS. The somewhat slower dynamics in PMA are characteristic of the chemical differences from PDMS and might be determined through computer simulations of the two polymer systems, but is completely distinct from the unresolvably fast and slow dynamics in PMMA. However, on very long time scales captured by Δ_0 in the FFCF, the acrylate polymers are marginally more similar, perhaps implying that the chemical interactions play a role in spectral diffusion in this temporal regime.

5.5 Conclusion

Despite the insensitivity of the FTIR spectra, the asymmetric stretching vibration of CO₂ solvated in three different polymeric environments can be used to probe the time-dependent structural dynamics of the gas and its surroundings. The dynamics of this small molecule, as reported by a vibrational mode, are surprisingly rich with details about its chemical and physical interactions with the polymer matrix. I find that molecular reorientation of CO₂

and spectral diffusion of its ν_3 mode are more similar in PMA and PDMS than in PMMA, despite the chemical similarities between PMA and PMMA. Dynamic differences above T_g appear to weaken the intermolecular forces between CO_2 and the polymer matrix without significantly changing the rate of vibrational relaxation of this mode. This results in more liberal molecular reorientation and spectral diffusion on the time scale of tens of ps. The dynamics that are accessible through time-resolved vibrational measurements of ν_3 appear to play a direct role in diffusion of CO_2 through polymer matrices.

The relevance of the dynamics measured in this study can be shown by comparison to the mutual diffusion coefficients of CO_2 through these polymer systems, as reported in the literature (Table 5.1). Within the Stokes-Einstein relationship, we can treat the inverse of each diffusion coefficient as a measure of the relative viscosity, η_{rel} , of each polymer towards the movement of CO_2 through its interior. Figure 5.10 plots the cone reorientation times, D_c^{-1} , and the homogeneous dephasing times, T_2 , measured in this study as a function of this relative viscosity parameter. The figure clearly shows that there is a correlation between reorientation and dephasing dynamics with faster gas diffusion. I recognize that correlation is not necessarily causality, but my results show that when the polymer is less viscous to CO_2 , the gas molecules reorient faster and their vibrations dephase more efficiently. A comparison of these measured dynamics could be combined with molecular dynamics simulations in the future to obtain an atomistic perspective of CO_2 transport through mixed-matrix membranes.

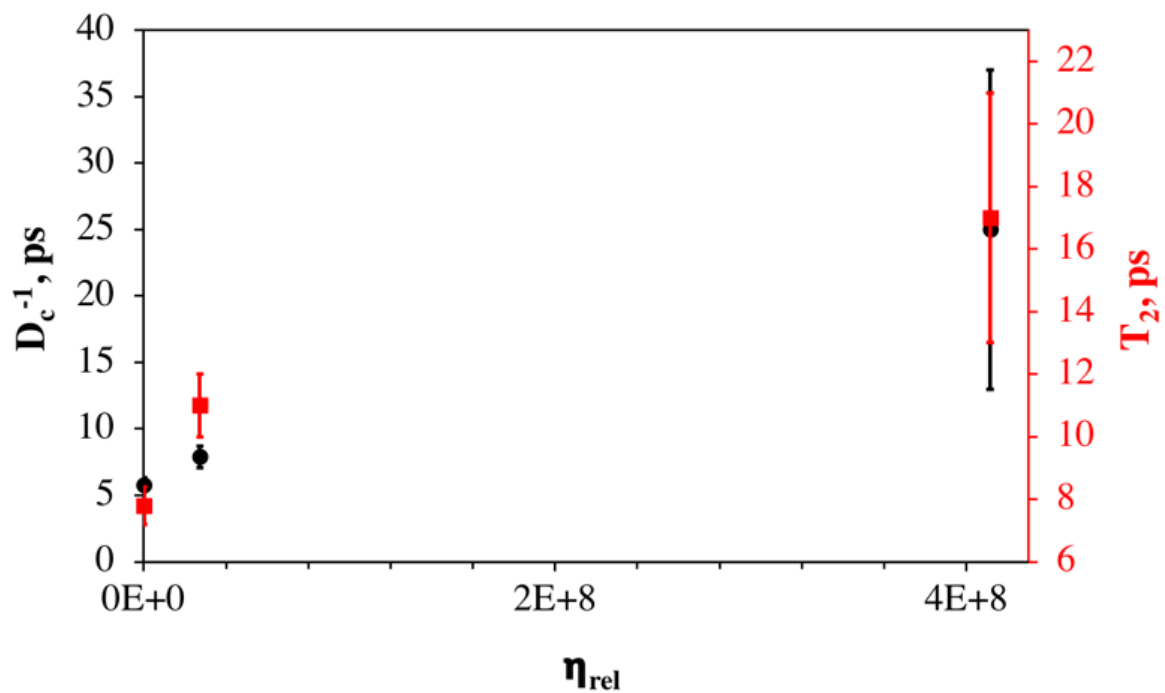


Figure 5.10. The CO₂ cone diffusion times and spectral dephasing times as a function of the relative viscosity parameter (the inverse of the mutual diffusion coefficients for CO₂ in each of the three polymers studied).

5.6 Full Set of 2D-IR Data

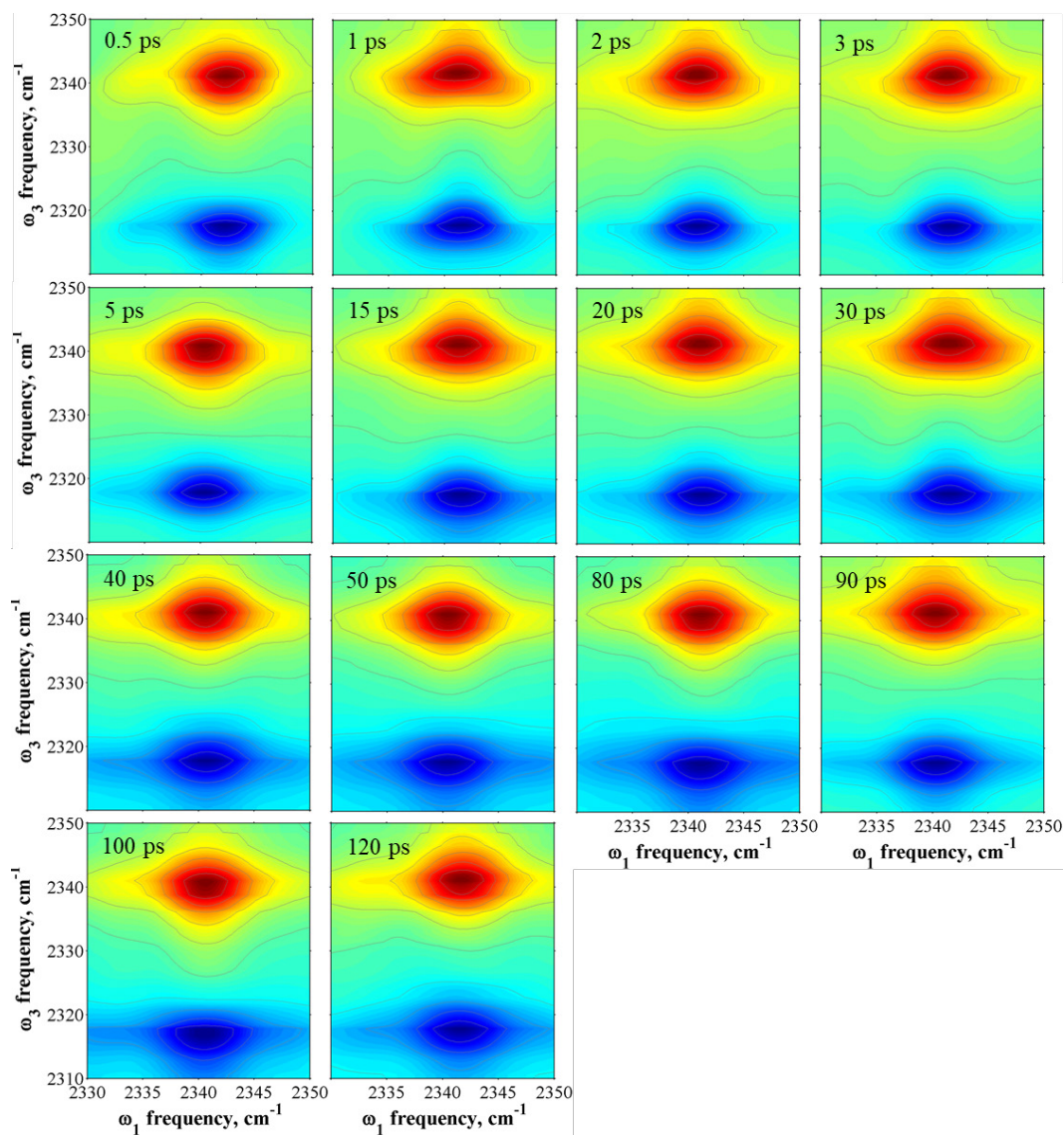


Figure 5.11. 2D-IR spectra of the CO₂ v₃ mode, dissolved in PDMS at a range of waiting time T_w values.

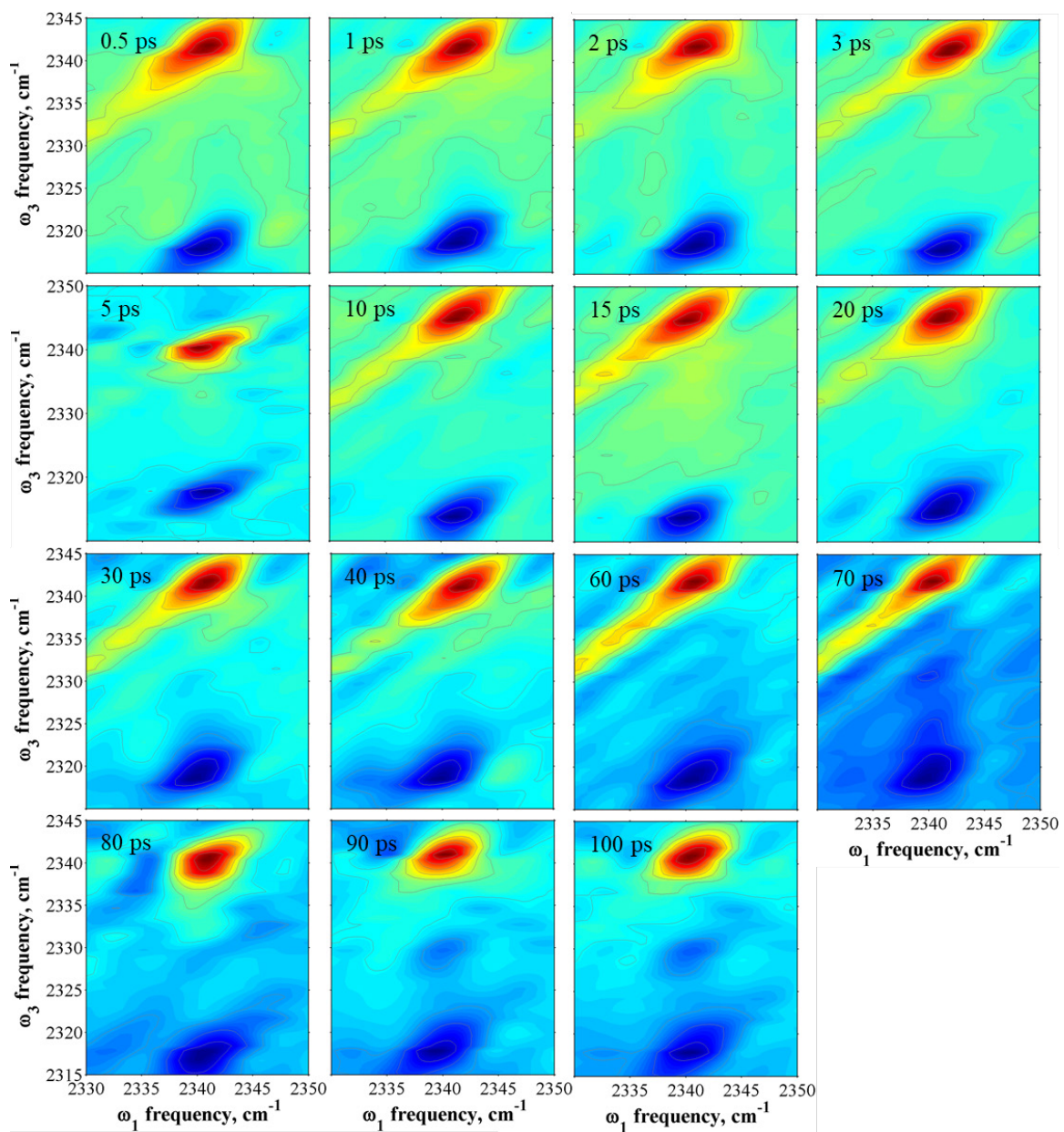


Figure 5.12. 2D-IR spectra of the CO₂ v₃ mode, dissolved in PMMA at a range of waiting time T_w values.

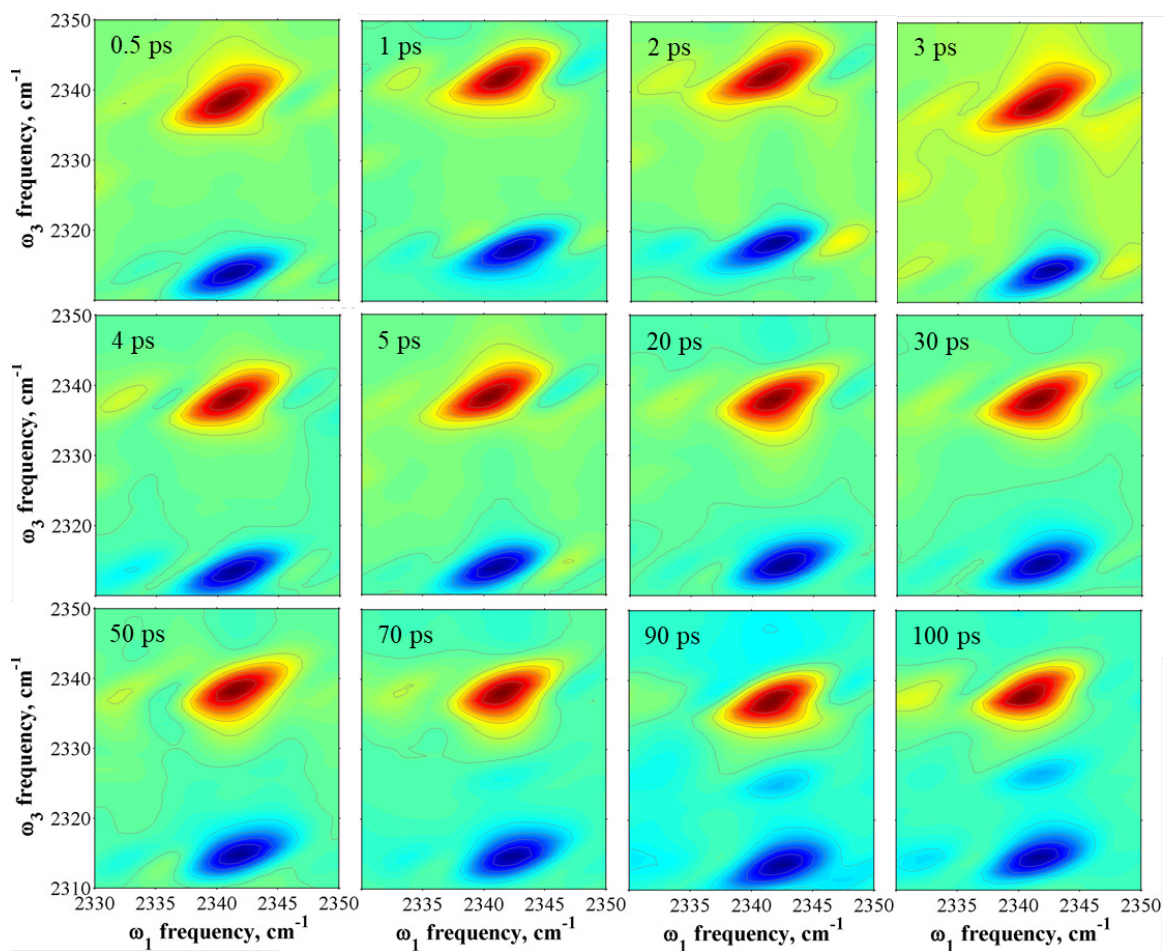


Figure 5.13. 2D-IR spectra of the CO₂ ν_3 mode, dissolved in PMA at a range of waiting time T_w values.

6. Carbon Dioxide in Microporous Structures

6.1 Chapter Summary

In this chapter, FTIR spectroscopy was used to study the behavior of CO₂ adsorbed to microporous structures such as MIL-53(Al) and ZIF-8. Pseudo-Voigt fits were used to describe possible differences in the dynamics of CO₂ dissolved inside the various structures. Preliminary 2D-IR studies of CO₂ adsorbed to MIL-53(Al) are presented, though the results were unable to provide significant dynamic insight due to artifacts such as scatter. The limitations of my current ultrafast spectroscopic setup are addressed, and I briefly discuss some scatter-reduction strategies that were attempted and might be employed in the future.

6.2 Introduction

Over the span of a single decade, the number of new publications discussing metal organic frameworks (MOFs) have dramatically increased from 500 to over 4,000 per year.¹⁴⁶ This newfound fascination with MOFs is for good reason too: they have a wide variety of potential applications including catalysis,¹⁴⁷⁻¹⁴⁹ gas storage,¹⁵⁰⁻¹⁵⁴ chemical sensing,¹⁵⁵⁻¹⁵⁸ drug delivery,¹⁵⁹⁻¹⁶¹ water purification,¹⁶² and luminescence.^{157, 163, 164}

The most basic of MOFs are constructed by linking metal cations with organic ligands to form a 3D network. Typically transition metals or lanthanides serve as the metal cation. However, some variations of MOFs may use elements such as aluminum or zinc instead. Examples of this include MIL-53(Al), and zeolitic imidazolate framework-8 (ZIF-8). Whether the guest molecule is solvent, an ion, or a gaseous molecule, the guest typically occupies the inner void of the pore. Most MOFs are designed to be microporous materials, to ensure the best mass to surface area ratio for the applications mentioned above.

Microporous materials are classified by having pore sizes of 2 nm or smaller.¹⁶⁵ Standard synthetic methods usually entail a one-pot hydrothermal or solvothermal reaction, making MOFs a feasible reality for industrial purposes.

Though MOFs have many applications, we focus on exploiting their gas storage capabilities. CO₂ is the most abundant of anthropogenic greenhouse gases leading to climate change. Carbon dioxide removal (CDR) technologies could help society mitigate further CO₂ emissions, but they are limited by their efficiency and scalability.^{112, 113} Mixed-matrix membranes are one promising CDR method. These systems often contain microporous CO₂ capturing agents (e.g zeolites or metal-organic frameworks) inside a gas-permeable polymer.^{114, 115}

Metal organic frameworks (MOFs) were previously regarded as rigid structures, but in recent years more MOFs have been shown to exhibit linker-dependent flexibility^{166, 167}. There are even instances of MOFs in which the pore size expands depending on how much guest molecule is present,¹⁶⁷ including MIL-53(Al).^{168, 169} Because of MIL-53's demonstrated ability to selectively bind large quantities of CO₂,¹⁵³ it presents itself as a potentially excellent solution for environmental cleaning purposes. If the dynamics of CO₂ adsorbed onto MIL-53(Al) change as a function of ambient gas pressure, analysis of 2D-IR spectra may help determine the fundamental reasoning for pore flexibility. A more flexible pore structure may be able to enhance gas loading capabilities for a given MOF. Understanding the dynamics of CO₂ adsorbed onto a family of flexible MOFs would inform synthetic chemists how to create structures with enhanced flexibility and improved gas loading ability.

In this chapter, I describe the processes for activating and loading CO₂ onto microporous structures, their resultant FTIR spectra, and the setbacks associated with ultrafast data collection.

6.3 Materials & Methods

6.3.1 MIL-53(Al) KBr Pellet Preparation

Basolite® A100 powder, also known as MIL-53(Al), was purchased from Sigma Aldrich. MIL-53(Al) powder was soxhlet extracted in DMF at 160 °C for 48 hours to ensure purity. After soxhlet extraction, the powder dried in an oven at 150 °C for minimum 24 hours to evaporate the majority of remaining DMF solvent. KBr powder (Sigma Aldrich, 99% purity) was stored in the same oven at 150°C for an indefinite amount of time until immediately before use in creating KBr pellets.

The soxhlet extracted powder was combined with KBr to create a ~10% by weight MIL-53(Al) mixture. Approximately 100 mg was loaded into a 13 mm KBr pellet press (Pike Technologies) and held under 8 tons of pressure for 15 minutes.

6.3.2 ZIF-8 KBr Pellet Preparation

Zinc 2-methylimidazole metal-organic framework (ZIF-8) was purchased from Strem Chemicals, Inc. The powder was kept at ambient temperature and moisture when not in use. KBr powder (Sigma Aldrich, 99% purity) was stored in an oven at 150°C for an indefinite amount of time until immediately before use in creating KBr pellets. ZIF-8 and KBr were combined to create a ~5% by weight ZIF-8 mixture. Approximately 70mg was loaded into a 13mm KBr hand pellet press (Pike Technologies) and compressed under 130 foot pounds of torque for 15 minutes.

6.3.3 MIL-53(Al) Sample Activation

MIL-53(Al) samples were activated following procedures adapted from the literature^{153, 170} to account for lower vacuum pump pressures used. To expunge any remaining H₂O and DMF, a MIL-53 sample was encased between two 25.4 mm diameter 3 mm thick CaF₂ windows inside the sample holder of a cryostat (Janis VPF-100). The cryostat was equipped with two external 50.8 mm diameter 3mm thick CaF₂ windows, allowing for optical measurements during the activation process. A dual stage rotary vane vacuum pump (TriVac D16A) brought the sample from atmospheric pressure down to approximately 50 torr. The sample temperature was controlled by a thermocouple connected to a controller (Lake Shore Cryotronics 325). Sample temperatures were raised by approximately 10 K every 10 minutes to prevent sample and CaF₂ window damage. After reaching 500 K, the high-temperature low-pressure environment was maintained for 18 hours to activate the sample. FTIR spectra were obtained before and after evacuation to ensure adequate release of DMF and water from the sample pores.

Following activation, MIL-53 samples were cooled to room temperature, then transported from the cryostat to a gas flow cell under an inert N₂ atmosphere. A system of two mass flow controllers were attached to N₂ and CO₂ regulators, and allowed for fine adjustments of the ratio of carrier (N₂) to analyte (CO₂) that flowed over the MIL-53 substrates.

6.3.4 ZIF-8 Sample Activation

ZIF-8 samples were activated according to procedures adapted from the literature.^{171,}
¹⁷² Similar to MIL-53(Al) samples, ZIF-8 samples were suspended between two 25.4 mm

diameter 3 mm thick CaF₂ windows inside the sample holder of a cryostat (Janis VPF-100). A dual stage rotary vane vacuum pump (TriVac D16A) brought the sample from atmospheric pressure down to approximately 50 torr. The sample temperature was controlled by a thermocouple connected to a controller (Lake Shore Cryotronics 325). Sample temperatures were raised by approximately 10 K every 10 minutes to prevent sample and CaF₂ window damage. After reaching 400 K, the high-temperature low-pressure environment was maintained for 18 hours to activate the sample.

Following activation, ZIF-8 samples were cooled to room temperature, then transported from the cryostat to a gas flow cell under an inert N₂ atmosphere. A system of two mass flow controllers were attached to N₂ and CO₂ regulators, and allowed for fine adjustments of the ratio of carrier (N₂) to analyte (CO₂) that flowed over the ZIF-8 substrates.

6.3.5 FTIR Spectra Collection

All FTIR spectra were collected using a Nicolet 6700 FTIR spectrometer (Thermo Scientific). The resolution was 1 cm⁻¹ at 16 scans. A section of the gas flow cell lacking KBr pellet was used as the background for all spectra.

6.3.6 Ultrafast Data Collection

The laser instrumentation for pump probe and 2D-IR measurements has been described previously.^{52, 85} Briefly, a regeneratively amplified Ti:Sapphire laser (Spectra-Physics, 800 nm, 40 fs pulse duration FWHM, 30 nm bandwidth FWHM) pumped an optical parametric amplifier (Spectra-Physics OPA 800-C) with a 1 kHz repetition rate. The resultant signal and idler beams were difference frequency mixed within a AgGaS₂ crystal to generate ~3 μJ mid-IR pulses (200 cm⁻¹ FWHM, 90 fs FWHM). The mid-IR pulses were centered at

approximately 2340 cm^{-1} corresponding to the CO_2 asymmetric stretching region for all spectroscopic measurements. Failure to purge the laser enclosure allowed atmospheric CO_2 to absorb $\sim 90\%$ of the generated mid-IR and eliminated all signal. Thus, the entire instrument was sealed and continuously purged with dry N_2 during all data collection.

For 2D-IR measurements, the mid-IR centered at 2340 cm^{-1} was split into three paths ($\sim 1\text{ }\mu\text{J}$ per pulse) and pointed onto the sample in the BOXCARS geometry.⁵³ The vibrational echo generated by the sample was interfered with a local oscillator ($0.3\text{-}0.5\text{ nJ}$ per pulse). The x- or ω_1 -axis was created by varying the delay time between the first two pulses and then taking the Fourier transform of the result. The y- or ω_3 -axis was optically Fourier transformed by spectrally resolving the heterodyned signal in a 0.32 m monochromator (150 line/mm grating, resolution 2 cm^{-1}). Signal was detected with a liquid N_2 cooled 64-element mercury cadmium telluride (MCT) array detector (Infrared Associates, Inc).

6.4 Results and Discussion

FTIR spectra of ZIF-8 and MIL-53(Al) samples before and after loading with CO_2 (g) are shown in Figure 6.1. I focus my analysis on the ν_3 stretch of CO_2 due to its known sensitivity to both solvatochromic shift^{106, 173} and ultrafast dynamics.¹⁷⁴ The spectra were fit to pseudo-Voigt functions and the pertinent values from this fit are displayed in Table 6.1. The ZIF-8 spectrum is dominated by a Gaussian contribution to the line shape (82%) whereas the MIL-53(Al) spectrum is dominated by a Lorentzian shape (95%). This difference between the two samples is intriguing given the pseudo-Voigt fits of CO_2 dissolved in polymers (Chapter 5) possessed mostly Lorentzian character. However, the linewidth contributions obtained from the FFCF indicated all three CO_2 -polymer systems

were actually dominated by inhomogeneous dynamics. This discrepancy between the linear fit and ultrafast variables highlights the need to study these systems via 2D-IR spectroscopy for a more accurate analysis of the dynamics.

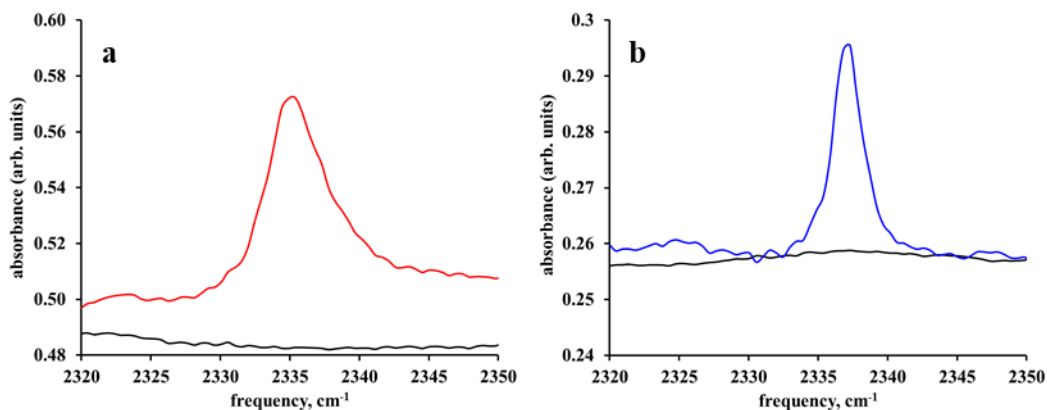


Figure 6.1. FTIR spectra of CO₂ v₃ stretch when adsorbed to ZIF-8 (a) and MIL-53(b) KBr pellets. Black lines in both spectra correspond to the respective samples before activation and CO₂ loading.

Table 6.1. Pseudo-Voigt parameters extracted from FTIR spectra of CO₂ loaded on ZIF-8 and MIL-53(Al) KBr pellets.

Sample	Center Freq. (cm ⁻¹)	FWHM (cm ⁻¹)	% Gaussian:	% Lorentzian:
ZIF-8	2336	5	82	18
MIL-53(Al)	2337	3	5	95

One important feature to note in both spectra is the magnitude of the baselines and their slight curvature. Mie scattering is especially efficient in the 2000-3000 cm⁻¹ range for objects with a radius of approximately 4-7 μm.¹⁷⁵ Work by Taheri et al. suggests that the particle size of MIL-53(Al) clusters is sensitive to the synthesis temperature. They successfully synthesized particles ranging from 1.5-3.6 μm by adjusting the reaction temperature from 473 to 493 K.¹⁷⁶ However, alternative findings from Embrechts states

the particle size is dictated by the concentration of organic linker. By manipulating this variable, they successfully synthesized MIL-53(Al) particles ranging from $<0.1 - 1.2 \mu\text{m}$.¹⁷⁷ A single MIL-53(Al) particle would not contribute significant scatter via Mie mechanisms, but the aggregation of multiple MIL-53(Al) particles could give rise to the observed background (Figure 6.1b). These difficulties could hold true for ZIF-8 samples as well, with reported particle sizes ranging from $<20 \text{ nm}$ to $2.8 \mu\text{m}$.^{178, 179} Similar phenomena are reported for samples like nanoporous silica in which a heterogeneous distribution of absorbing material in the matrix causes micron-sized regions that both absorb and scatter to a significant degree.¹⁸⁰

Attempts at collecting ultrafast spectra of the MIL-53(Al) and ZIF-8 samples loaded with CO_2 were ultimately hindered by scatter. The current setup is unable to circumvent the scatter, as shown by a sample spectrum in Figure 6.2. Scatter from these samples primarily manifests along the diagonal ($\omega_1 = \omega_3$), however Fourier ringing also persists across the ω_1 axis. The integrated intensity (I) captured by the MCT detector can be expressed as the following:¹⁸¹

$$I \propto |E_{LO} + E_{signal} + E_{1,scatter} + E_{2,scatter} + E_{3,scatter}|^2 \quad 6.1$$

Where E_{LO} represents the electric field of the local oscillator (LO) and E_{signal} is the vibrational photon echo from the sample that is heterodyned by the LO. The resultant interferogram must then be Fourier transformed to yield the desired 2D-IR spectrum.

Each of the beams used in the BOXCARS geometry generates its own scatter when interacting with the sample ($E_{1,scatter}$, etc.) and this subsequent scatter also interferes with the LO. Some of the terms in 6.1 can be subtracted off through the use of an optical

chopper, and I attempted to employ experimental schemes using multiple choppers and shutters like those found in the literature.¹⁸² The existing body of 2D-IR research contains various methods of scatter reduction, some of which are practiced in our own lab such as fibrillation. To summarize, fibrillation refers to reflecting both beam 3 and the LO off a delay stage that has a piezo actuator (PZA) equipped. A wave-form generator drives the PZA with a triangle-wave at ~ 17 Hz to cancel out scatter from beam 3 with the LO.¹⁸¹ Other methods of scatter reduction include techniques such as pulse shaping^{183, 184} and phase cycling.^{185, 186}

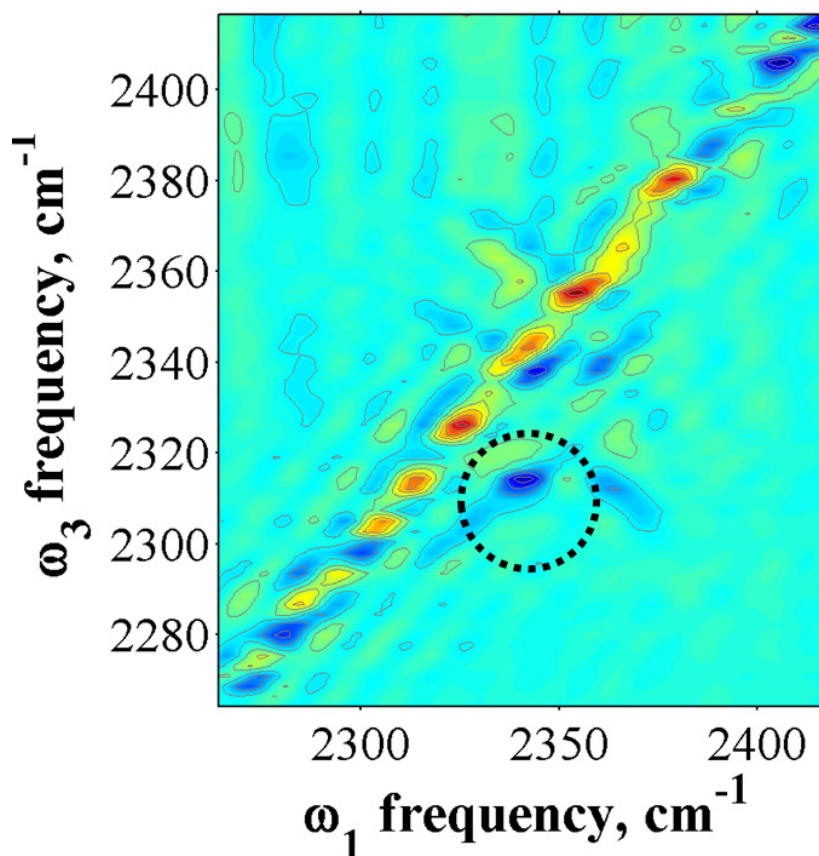


Figure 6.2. Sample 2D-IR spectrum at $T_w = 3$ ps for CO_2 in MIL-53(Al). The black circled region is a possible 1-2 peak but it is obfuscated by both scatter and gaseous CO_2 .

Thus far, the existing 2D-IR literature has only measured dynamics in three MOF systems: The first studied functionalized MOFs that had Fe-bound carbonyls added to serve as a vibrational probe.¹⁸⁷ Subsequent studies by Nishida examined hydroxyl ligands in MIL-53(Al).¹⁸⁸ Most recently, Hack et al. examined dynamics of protonated water clusters encapsulated by a zeolite.¹⁸⁹ They successfully observed enhanced inhomogeneous broadening at an early T_w compared to bulk water due to confinement, as well as cross peaks occurring between free and hydrogen-bonded H₂O molecules.¹⁸⁹ The sensitivity of water to the surroundings is a promising sign that 2D-IR is an excellent method for studying even more MOF-guest systems such as CO₂ in MIL-53(Al).

CO₂ in MIL-53(Al) is a particularly interesting future system of study due to the presence of spectrally separated gas adsorption conformations. The ν_3 stretch of CO₂ has been shown to occur at 2337 cm⁻¹ when low pressures of gas are used and the molecules exist as monomers inside the porous framework. With sufficiently high pressures, CO₂ dimers begin to form and a second peak appears at 2334 cm⁻¹.¹⁵³ If CO₂ molecules follow a mechanism of hopping from isolated pores to occupied pores to form a dimer, then crosspeak behavior between the 2334 and 2337 cm⁻¹ peaks could be correlated with mechanisms of gas diffusion in MIL-53(Al). Other microporous structures such as ZIF-8 with flexible pores also exhibit pressure-dependent absorption behavior.¹⁹⁰ 2D-IR spectra of such systems could provide valuable insights on gas diffusion mechanisms in microporous structures to inform the synthesis of better CDR technologies.

6.5 Conclusion

I was unable to obtain ultrafast data of CO₂ loaded on MIL-53(Al) and ZIF-8. The literature contains additional scatter reduction strategies that could be tried as an alternate means of data collection.¹⁸⁹ Given the lack of 2D-IR data describing guest molecules in microporous structures such as MOFs and zeolites, the aforementioned samples present an interesting avenue of research worth exploring in the future. 2D-IR possesses the required sensitivity to probe subtle changes in the surroundings of a vibrational probe, which would allow us to learn more about the dynamics of guest molecules.

7. Ruthenium Hydride Formation in Sol-Gel Glasses Results in Different Ultrafast Vibrational Dynamics

Reproduced from

Pyles, C.G.; Patrow, J.G.; Cheng, Y.; Tonks, I.; Massari, A.M.; "Ruthenium Hydride Formation in Sol-Gel Glasses Results in New Ultrafast Vibrational Dynamics" *J. Chem. Phys.* **2022**, *submitted*.

Copyright © AIP Publishing.

7.1 Chapter Summary

In a recent study, $\text{Ru}_3(\text{CO})_{12}$ entrapped in a silica sol-gel was found to be catalytically inactive,² yet the entrapped hydride is catalytically active. I performed FTIR, 2D-IR, and infrared pump probe spectroscopies to ascertain the origins of the enhanced catalytic activity. My comparative studies examined $\text{Ru}_3(\text{CO})_{12}$ dissolved in THF, the encapsulated hydride $[\text{HRu}_3(\text{CO})_{11}]^-$ which forms upon alumina gelation, and the synthesized hydride $[\text{NEt}_4][\text{HRu}_3(\text{CO})_{11}]$ in bulk THF. These studies also show a 2D-IR probe like the 2019 cm^{-1} CO stretch in each hydride is highly sensitive to both local and long-range surroundings, as evidenced by inhomogeneous offsets that had a small yet genuine difference in their magnitude upon introduction of the alumina matrix. Though more information is needed to ascertain the origins of catalytic activity for this system, 2D-IR nonetheless revealed new information about the nature of the THF solvent shell in these three samples.

7.2 Introduction

The dynamics of molecules in the first solvation shell around a catalyst are key to enabling reactants to reach a transition state and form products.¹⁹¹⁻¹⁹⁴ These time-dependent solvent-solute interactions stabilize or destabilize the transition state, thereby directly influencing the rate coefficient.¹⁹⁵⁻¹⁹⁹ It is for precisely this reason that catalytic rate constants are always solvent specific.²⁰⁰⁻²⁰³ The random, thermally-driven motions of solvent molecules effectively allow the catalyst (and substrate) to sample the energetic landscape that spans the reaction coordinate. In biomacromolecules for example, key structural motions for the reactivity of enzymes have been tied to the dynamics of the

surrounding solvation layer.²⁰⁴⁻²⁰⁹ Ultrafast dynamics in the solvation shell have also been implicated in mechanistic steps for organometallic catalysts.^{210,211}

In addition to changing the identity of the solvent itself, the reactivity of catalysts can also be controlled by encapsulation in small volumes of solvent inside of solid support matrices, such as zeolites or sol-gel glasses.²¹²⁻²¹⁶ Alumina sol-gels have been shown to increase the catalytic activity of homogeneous catalysts entrapped inside of the sol-gel pores.²¹⁷⁻²¹⁹ In a recent study, it was shown that encapsulation of $\text{Ru}_3(\text{CO})_{12}$ in alumina sol-gels increased its catalytic activity for hydrogenation reactions.²¹⁸ It was proposed that the improved activity originated from the formation of catalytically-active metal hydrides during the sol-gel aging process;²¹⁹ metal hydrides have a long history in chemical catalysis.²²⁰⁻²²² In a subsequent study, our group demonstrated definitively that the ruthenium hydride ($[\text{HRu}_3(\text{CO})_{11}]^-$) was indeed formed within the alumina sol-gel glass,²²³ however, we did not explore how solvent dynamics in nanoscopic pores might contribute to catalytic activity.

To address this question, infrared pump-probe and two-dimensional infrared (2D-IR) spectroscopy were performed on $\text{Ru}_3(\text{CO})_{12}$, its alumina sol-gel entrapped counterpart $[\text{HRu}_3(\text{CO})_{11}]^-$, and a synthesized version of the hydride $[\text{NEt}_4][\text{HRu}_3(\text{CO})_{11}]$. This series of samples allows me to determine if changes in the dynamics are due to the alumina sol-gel backbone or perturbation of the solvent shell upon formation of the hydride. I show that the vibrational lifetimes of the Ru-bound carbonyl modes are dramatically changed for the hydrides regardless of whether they are encapsulated by sol-gel or

surrounded by bulk THF. This suggests that the surrounding solvent, not the alumina backbone, is the main energy-acceptor during vibrational energy relaxation (VER).

2D-IR studies report on the structural dynamics of the solvation shell surrounding the carbonyl modes for the three samples. These studies also allowed me to quantify how intramolecular vibrational energy redistribution from carbonyl modes attached to the ruthenium centers change with sol-gel entrapment.

7.3 Experimental

7.3.1 Materials

$\text{Ru}_3(\text{CO})_{12}$, aluminum isopropoxide ($\text{Al}(\text{O-i-Pr})_3$), and tetrahydrofuran (THF) used for alumina sol-gel studies were purchased from Millipore-Sigma and used as received. Sodium borohydride (NaBH_4) used in the air- and moisture-sensitive synthesis of $[\text{NEt}_4][\text{HRu}_3(\text{CO})_{11}]$ was purchased from Millipore-Sigma and dried in vacuo prior to use. The solvents used in the synthesis of $[\text{NEt}_4][\text{HRu}_3(\text{CO})_{11}]$ (THF, pentane, dichloromethane and Et_2O) were dried through activated alumina on a Pure Process Technology solvent purification system.

7.3.2 Sol-Gel Formation

$\text{Ru}_3(\text{CO})_{12}$ alumina sol-gels were prepared according to a previous procedure.²¹⁸ Approximately 0.02 mmol of $\text{Ru}_3(\text{CO})_{12}$ were dissolved in 1 mL of tetrahydrofuran (THF) and stirred. Separately, approximately 6 mmol of $\text{Al}(\text{O-i-Pr})_3$ were dissolved in 4 mL of THF, which was then decanted into the stirring $\text{Ru}_3(\text{CO})_{12}$ solution. The mixture was stirred for 20 min. For the FTIR, pump-probe and 2D-IR measurements, the $\text{Ru}_3(\text{CO})_{12}/\text{Al}(\text{O-i-Pr})_3$ mixture was sandwiched between two calcium fluoride (CaF_2) windows with a 50

micron spacer that had two small strips cut out of the spacer (one on top and one at the bottom) to allow for the introduction of water. The sandwiched sol-gel sample was then placed in a homemade solvent cell built such that water surrounded the sample edges. This allowed water to diffuse into the $\text{Ru}_3(\text{CO})_{12}/\text{Al}(\text{O}-i\text{-Pr})_3$ mixture and catalyze the alumina sol-gel formation.

7.3.3 Synthesis of $[\text{NEt}_4][\text{HRu}_3(\text{CO})_{11}]$

In a glovebox, $\text{Ru}_3(\text{CO})_{12}$ (106 mg, 0.166 mmol), NaBH_4 (33 mg, 0.87 mmol), and 17 mL THF were added to a 20 mL scintillation vial along with a small stir bar. The reaction was then sealed with a Teflon screw cap and stirred for 40 min at room temperature. $[\text{Et}_4\text{N}]\text{Br}$ (42 mg, 0.20 mmol) was then added to the solution, and the reaction was stirred for another 1 h. The solution was filtered through a pipet plug and concentrated to 2 mL by vacuum. 15 mL pentane was added to the solution to form a precipitate. The resulting suspension was filtered and the precipitate was washed with 2 mL pentane. The precipitate was then dissolved in CH_2Cl_2 , and crystallization of $[\text{NEt}_4][\text{HRu}_3(\text{C})_{11}]$ was achieved by vapor diffusion of Et_2O into CH_2Cl_2 , yielding $[\text{NEt}_4][\text{HRu}_3(\text{C})_{11}]$ as reddish-brown crystals. Yield: 95 mg (0.13 mmol, 77%)

7.3.4 FTIR Measurements

All FTIR spectra were collected using a Nicolet 6700 FTIR spectrometer (Thermo Scientific). The resolution was 1 cm^{-1} at 16 scans. The spectrum of $\text{Ru}_3(\text{CO})_{12}$ in THF and $[\text{NEt}_4][\text{HRu}_3(\text{CO})_{11}]$ in THF were collected with THF as the background. The spectra of $\text{Ru}_3(\text{CO})_{12}$ entrapped in the alumina sol-gel were collected with a background of air.

7.3.5 2D-IR Measurements

The 2D-IR setup has been described previously.^{8,9} Briefly, a regeneratively amplified Ti:Sapphire laser (Spectra-Physics, 800 nm, 40 fs pulse duration FWHM, 30 nm bandwidth FWHM, 600 mW) pumped an optical parametric amplifier (OPA) (Spectra-Physics) with a repetition rate of 1 kHz. Near-IR signal and idler beams generated by the OPA's beta-barium borate (BBO, 3 mm thick) crystal were difference frequency mixed in a silver gallium sulfide crystal (AgGaS_2 , 0.5 mm thick), generating 3 μJ mid-IR pulses. The final output pulses had a spectrum that was centered at 2040 cm^{-1} (THF sample) or 2020 cm^{-1} (sol-gel sample). The bandwidth was approximately 200 cm^{-1} (FWHM). The mid-IR pulse train was split into three separate beams and focused onto the sample in the BOXCARS geometry.¹⁰ The generated vibrational echo was overlapped with a local oscillator and sent to a spectrometer with a spectral resolution of 4 cm^{-1} and detected with a liquid nitrogen cooled 64-pixel mercury cadmium telluride (MCT) linear array detector (Infrared Associates, Inc.). The entire mid-IR beam path was purged with dry air (-100°F dew point).

7.4 Results and Discussion

Prior work performed by our group showed that $\text{Ru}_3(\text{CO})_{12}$ reacts with $\text{Al}(\text{O}-i\text{-Pr})_3$ and water to form $[\text{HRu}_3(\text{CO})_{11}]^-$ entrapped in an alumina sol-gel.²²⁷ The ruthenium complex becomes catalytically active following encapsulation. Despite successfully identifying the products of the sol-gel reaction, the impact of confined solvent on catalytic activity remained unclear. FTIR, infrared pump probe, and 2D-IR spectroscopy were used to compare the behavior of bulk and confined THF as sensed by the carbonyl probes.

The FTIR spectrum of $\text{Ru}_3(\text{CO})_{12}$ in THF shows three distinct peaks at 2005 cm^{-1} , 2030

cm^{-1} and 2060 cm^{-1} Figure 7.1. These peaks have been assigned as the E' (radial), A_2' (axial) and E' (axial) carbonyl modes on the ruthenium molecule.²²⁴⁻²²⁶ Sol-gel formation results in a loss of one carbon monoxide ligand from the complex and drastic changes to the spectrum. The synthesized version of the hydride, $[\text{NEt}_4][\text{HRu}_3(\text{CO})_{11}]$, has an FTIR spectrum almost identical to that of the sol-gel Figure 7.1.

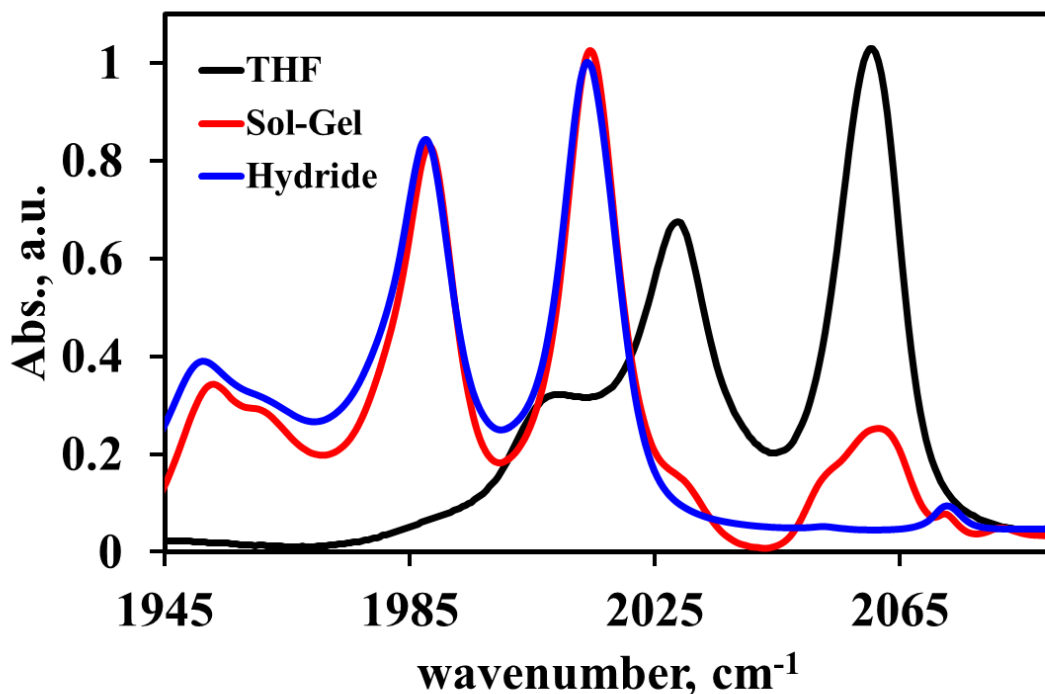


Figure 7.1. Normalized FTIR spectra of $\text{Ru}_3(\text{CO})_{12}$ In THF (black) and entrapped in the alumina sol-gel (red). Upon sol-gel formation, the modes in $\text{Ru}_3(\text{CO})_{12}$ undergo a dramatic red shift. The spectrum of the synthesized $[\text{NEt}_4][\text{HRu}_3(\text{CO})_{11}]$ dissolved in THF is also shown (blue).

To investigate the potential role of solvent environment in the increased catalysis of the encapsulated ruthenium, we performed pump-probe measurements aimed at identifying changes in vibrational coupling. We compare the dynamics of three different samples: $\text{Ru}_3(\text{CO})_{12}$ in THF, $[\text{HRu}_3(\text{CO})_{11}]^-$ formed in the alumina sol-gel, and synthesized

[NEt₄][HRu₃(CO)₁₁] in THF. The congested nature of the FTIR spectra lead to convoluted pump probe spectra for all three samples as shown in Figure 7.2.

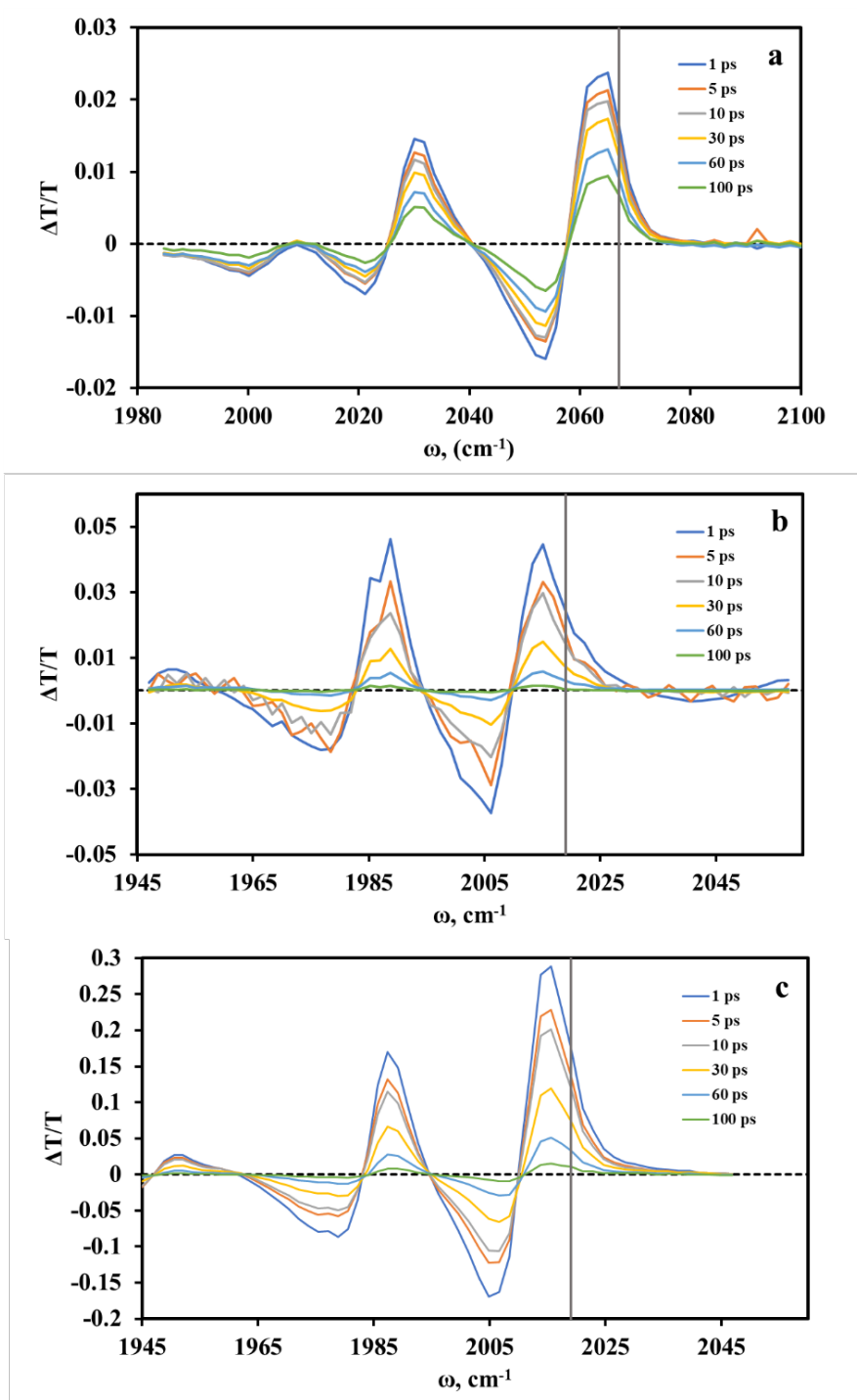


Figure 7.2. Pump-probe spectra of a) Ru₃(CO)₁₂ in THF, b) [HRu₃(CO)₁₁]⁻ entrapped in the alumina sol-gel, and c) [NEt₄][HRu₃(CO)₁₁] in THF.

Relaxation of a higher frequency peak into a lower energy mode contributes vibrational excitation that can artificially lengthen the vibrational lifetime. Therefore, the blue edge of the highest energy carbonyl modes (2065 or 2019 cm^{-1}) in the pump probe spectra was chosen for all lifetime analyses to avoid such artifacts. Population decays were fit to biexponential functions for all three samples. Figure 7.3 shows the population decay of the carbonyl stretch for $\text{Ru}_3(\text{CO})_{12}$ in THF, $[\text{HRu}_3(\text{CO})_{11}]^-$ in the alumina sol-gel, and the synthesized hydride.

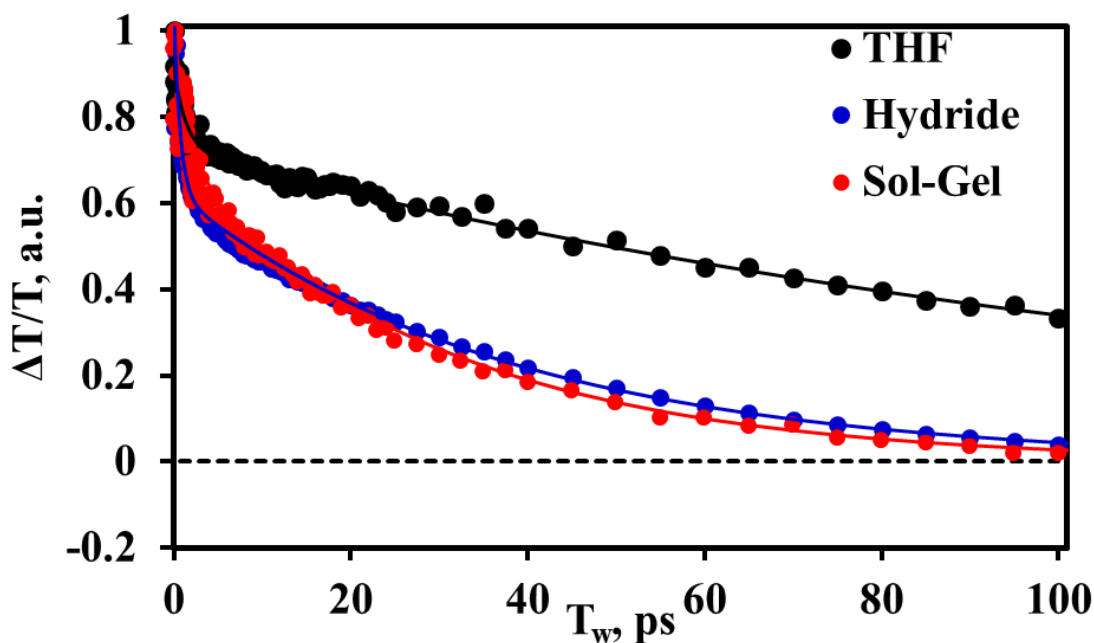


Figure 7.3. Pump probe population decay for the carbonyl stretch of $\text{Ru}_3(\text{CO})_{12}$ in THF (black), $[\text{HRu}_3(\text{CO})_{11}]^-$ in the alumina sol-gel (red), and $[\text{NEt}_4][\text{HRu}_3(\text{CO})_{11}]$ in THF (blue). Markers represent experimental data, solid lines show best biexponential fit.

The most salient dynamic difference between the three samples is the vibrational lifetime of the original $\text{Ru}_3(\text{CO})_{12}$ complex dissolved in THF ($T_1 = 130 \pm 15$ ps) compared to that of $[\text{HRu}_3(\text{CO})_{11}]^-$ in the sol-gel ($T_1 = 30 \pm 8$ ps) and the synthesized hydride dissolved in THF ($T_1 = 37 \pm 2$ ps). Both hydrides exhibit drastically faster lifetime decays compared to $\text{Ru}_3(\text{CO})_{12}$ regardless of whether encapsulated by alumina or solvated entirely by THF.

The vibrational lifetimes for the hydride in the sol-gel and THF being within error of one another suggest that the chemical environments are similar. This is not necessarily surprising as there is expected to be a significant amount of THF inside the alumina sol-gel pores. Ignoring the error, the carbonyl mode encapsulated by the sol-gel relaxes 9 ps quicker than the same mode in THF. This discrepancy could be explained by new routes of vibrational energy relaxation (VER) that become available as the sol-gel becomes increasingly crosslinked. Modified THF bath modes inside the sol-gel pores, newly formed low-lying energy-accepting modes among the alumina sol-gel matrix, or finite amounts of water in the pores could all provide alternate mechanisms of VER that expedite vibrational relaxation.

The synthetic route and its respective product $[\text{NEt}_4][\text{HRu}_3(\text{CO})_{11}]$ are water sensitive,²²⁷ necessitating the use of dry THF in the synthesized hydride ultrafast experiments. $\text{Ru}_3(\text{CO})_{12}$ was studied in a 1:5 solution of water and THF as an alternative system to determine whether water expedites VER. The ratio of solvents used replicates those of prior FTIR kinetic study measurements²²⁷ and the original synthetic process.²²⁸ Including water decreases the carbonyl vibrational lifetime from 130 to 110 ± 2 ps. However, this solvent mixture used does not necessarily capture the same molar ratio found in the confined environment of a sol-gel pore. The sol-gel sample cell was constructed to allow water to slowly diffuse into the aluminum / ruthenium mixture and catalyze gel formation. Forming crosslinks too quickly results in a sample that scatters significant light before an adequate number of T_{ws} have been collected. The similarity in T_1 values for the synthesized hydride in dry THF and sol-gel encapsulated hydride imply that the pores

contain predominantly THF. Subsequent 2D-IR experiments can better ascertain the origin of both dynamic similarities and differences between the two hydrides and the original ruthenium compounds.

Solvent dynamics of the three compounds were further studied via 2D-IR. We focus our analysis on the 2060 cm^{-1} and 2014 cm^{-1} modes in the THF and hydride vibrational spectra, respectively, since these avoid overlap with other spectral features. The dynamics were analyzed as a function of T_w via the center line slope (CLS) method.⁵⁴ A plot of the CLS values as a function of waiting time (T_w) is shown in Figure 7.4. Data beyond 10 ps was not obtainable for the sol-gel. The significantly shorter vibrational lifetime and solid-state nature of the sample leads to increasingly worse signal to noise as a function of T_w . For the $\text{Ru}_3\text{CO}_{12}$ and $[\text{NEt}_4][\text{HRu}_3(\text{CO})_{11}]$ samples in THF, CLS values were obtained out to 70 ps.

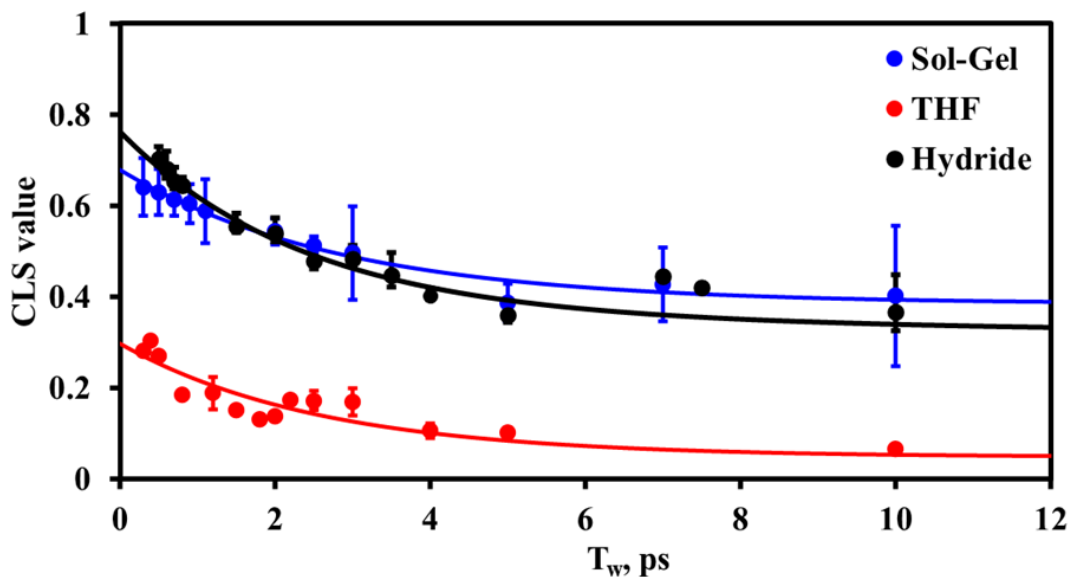


Figure 7.4. CLS decays for $\text{Ru}_3(\text{CO})_{12}$ in THF (black), $[\text{HRu}_3(\text{CO})_{11}]^-$ in the alumina sol-gel (red), and $[\text{NEt}_4][\text{HRu}_3(\text{CO})_{11}]$ in THF (blue).

Each CLS decay was fit to an exponential plus an offset. The time constants for the exponential decays are the same within error (Table 7.1). In THF the original Ru₃CO₁₂ compound has a $\tau_1 = 2.6 \pm 0.9$ ps. For the hydride in the alumina sol-gel, $\tau_1 = 3 \pm 1$ ps and in THF $\tau_1 = 2.4 \pm 1$ ps. This shows that the fast frequency fluctuations experienced by the CO ligands for the Ru₃CO₁₂ and hydride compounds occur on similar time scales. The alumina sol-gel matrix is unlikely to be the cause of these fluctuations, given the THF samples lack sol-gel and the alumina backbone itself is expected to be quite rigid. Therefore, these motions most likely stem from the surrounding THF molecules which are the major component of the ruthenium complex solvent shells. The three τ_1 values being within error of each other suggest that the shorter time scale motions in THF and the alumina sol-gel are the same.

The similarities in shorter time scale dynamics among the three samples can be rationalized by referring to previous studies conducted by Yamada et al., which examined the effects of nanoconfinement on solvent reorientational dynamics in nanoporous silicate sol-gel glasses.²²⁹ In these nanoconfined spaces, the fastest observable solvent motions occurred on time scales similar to bulk solvent motions. These motions were attributed to solvent molecules far enough away from the walls of the pore that they were essentially bulk-like. Conversely, slower solvent dynamics arose from solvent molecules interacting with the surfaces of the silica nanopore. Therefore the similarities in τ_1 among the three samples imply that the carbonyl groups are sensing solvent molecules that behave like the bulk and instead of something with restricted motion such as surface-adsorbed molecules, like those found near the walls of a nanopore.

In our own studies the slower motions of the surroundings, which include the solvent and the alumina backbone, manifest as varying degrees of offset in the CLS decay (Figure 7.4). Efficient vibrational energy relaxation in the three samples along with instrumental limitations limit the range of T_{ws} whose CLSs can be successfully measured. The magnitude of CLS offset can nonetheless be used to identify differences in slow dynamics sensed by the carbonyl ligands among the Ru_3CO_{12} , sol-gel, and synthesized hydride. For all T_{ws} past ~ 6 ps, the CLS offset is largest in the sol-gel, similarly large for the synthesized hydride in THF, and nearly zero for the original Ru_3CO_{12} compound. The sol-gel offset which exceeds that of the hydride implies that solvent molecules near the walls of an alumina nanopore and motions of the alumina walls contribute toward slower dynamics. However, the offset of the hydride dissolved in THF differs by less than 10% from the sol-gel, implying that bulk solvent motions are the primary source of the slower dynamics.

The CLS decays were used to quantify the homogeneous and inhomogeneous contributions to the FTIR linewidth via the frequency-frequency correlation function (FFCF).⁴⁸ The following correlation function was assumed for the fitting:

$$C(t) = \frac{\delta(t)}{T_2} + \Delta_1^2 e^{-\frac{t}{\tau_1}} + \Delta_0^2 \quad 7.1$$

Where T_2 is the pure dephasing time associated with the homogeneous linewidth, and Δ_1 and τ_1 are the inhomogeneous magnitude and time constants, respectively and Δ_0 is the contribution to the linewidth from long time scale dynamics. The results of the FFCF fitting analysis are shown in Figure 7.1. Upon entrapment in the sol-gel, the FTIR linewidth

decreases from 12 cm⁻¹ to ~10 cm⁻¹. For the hydride dissolved in THF, the linewidth narrows to ~11cm⁻¹.

In the THF case, the homogeneous dynamics (Γ) contribute about 25% of the total FTIR linewidth while in the sol-gel and synthesized hydride they contribute about 20%. Therefore, the relative homogeneous contributions to the FTIR linewidth decrease while the relative inhomogeneous contributions to the FTIR linewidth (summation of Δ_1 and Δ_0) increase upon replacing a carbonyl ligand with a hydride. This suggests the presence of slower overall solvent dynamics for both hydrides compared to Ru₃CO₁₂ in bulk THF. If the slowed dynamics were primarily due to alumina modes, the hydride dissolved in THF would not experience a relative increase in the inhomogeneous linewidth similar to that of the sol-gel.

Table 7.1. FFCF Fit Parameters of the Ruthenium Compounds

Sample	ω_{CO} (cm ⁻¹)	T ₁ (ps)	Γ (cm ⁻¹)	Δ_1 (cm ⁻¹)	τ_1 (ps)	Δ_0 (cm ⁻¹)
THF	2060.04(±0.08)	130(±15)	2.9(±0.2)	4.57(±0.03)	2.6(±0.9)	2.00(±0.05)
Sol-Gel	2014.20(±0.09)	30(±8)	1.9(±0.3)	2.74(±0.05)	3(±1)	3.14(±0.03)
Hydride	2013.90(±0.07)	37(±2)	2.1(±0.2)	3.7(±0.08)	2.4(±1)	2.96(±0.05)

For both hydrides, the measurable spectral diffusion (Δ_1) shrinks while the static inhomogeneous offset, Δ_0 , increases. Ru₃(CO)₁₂ is likely to be found near the walls/surfaces of a nanopore. Molecules near the pore wall will be more sensitive to the slower orientational motions exhibited by solvent molecules interacting with the pore wall along with the expected slower dynamics of the alumina itself. This will lead to an increase

in Δ_0 . Concomitantly, these molecules will be less sensitive to the bulk like motions of solvent molecules farther away from the pore wall leading to a decrease in Δ_1 . These processes most likely do contribute to some degree to the sol-gel inhomogeneous dynamics, as shown by the sol-gel hydride having a Δ_1 smaller than that of the hydride in the bulk THF, and a Δ_0 which exceeds that of the hydride in bulk THF. However, this rationale cannot explain the inhomogeneous dynamics of the hydride dissolved in THF that more closely resemble those of the sol-gel than the original $\text{Ru}_3\text{CO}_{12}$ molecule.

The similar FFCF parameters among the hydrides could be due to two possible scenarios: Either the carbonyl modes are significantly more sensitive to spectral diffusion induced by solvent motions rather than the alumina sol-gel backbone, or on average the sol-gel carbonyl probe is sufficiently close to the center of a nanopore that the solvent dynamics experienced resemble those of bulk solvent. XRD studies of water-catalyzed alumina sol gels like those used in this work indicate the structures are highly amorphous when the reaction takes place at room temperature, as evidenced by the lack of distinct diffraction peaks.²³⁰

The amorphous nature of the alumina sol-gel means the dynamics observed most likely probe a range of pore-sizes. This could allow measuring dynamics that are a combination of solvent motions near the walls and those in the middle of a pore. Additionally, the significant increase in Δ_0 that persists for the hydride in bulk THF could also mean that the solvent shell undergoes new patterns of long-range ordering that did not exist for the original $\text{Ru}_3\text{CO}_{12}$ molecule, and this new ordering dominates the inhomogeneous

dynamics. This would cause the inhomogeneous dynamics to slow regardless of whether the probe is confined in a nanopore or bulk solvent.

It is important to note that $[\text{HRu}_3(\text{CO})_{11}]^-$ is used to probe the sol-gel environment while $\text{Ru}_3(\text{CO})_{12}$ is used to probe the THF environment. $[\text{HRu}_3(\text{CO})_{11}]^-$ almost assuredly couples differently to the surrounding solvent environment as evidenced by expedited vibrational relaxation for both hydrides. We have previously shown that formation of the hydride places additional electron density on the Ru nuclei. The Ru nuclei then participate in π -backbonding and place additional electron density placed on the carbonyl ligands which shift their vibrational frequencies.²²⁷ A shift in vibrational frequency can allow for better energy-match between solvent and solute vibrational modes, which would expedite VER. However, it is unlikely that the molecule couples differently to short time scale modes compared to longer time scale modes given that THF motions appear to drive the majority of the observed dynamics. Differences in coupling strength for long versus short motions would be a possibility if fast motions were dominated by solvent and slow motions are driven by the alumina back-bone. The comparison of the hydride in bulk-THF and the sol-gel encapsulated hydride show this is not the case.

7.5 Conclusion

Due to the amorphous nature of the alumina sol-gel, the measured dynamics of the encapsulated hydride $[\text{HRu}_3(\text{CO})_{11}]^-$ most likely survey solvent dynamics across a range of pore sizes. Despite this, the inhomogeneous offset for the synthesized hydride $[\text{NEt}_4][\text{HRu}_3(\text{CO})_{11}]$ in bulk THF nearly matches that of the encapsulated hydride, meaning the main contributor to slow inhomogeneous dynamics is most likely a newly formed and

highly ordered solvent shell. $\text{Ru}_3(\text{CO})_{12}$ entrapped in a silica sol-gel was found to be catalytically inactive,² yet the entrapped hydride is catalytically active.

Subsequent studies of the synthesized hydride's catalytic activity in bulk THF versus an alumina sol-gel with a controlled pore size distribution could help determine the origin of the catalytic behavior. These studies also show a 2D-IR probe like the 2019 cm^{-1} CO stretch in each hydride is highly sensitive to both local and long-range surroundings, as evidenced by inhomogeneous offsets that had a small yet genuine difference in their magnitude upon introduction of the alumina matrix. Though more information is needed to ascertain the origins of catalytic activity for this system, 2D-IR nonetheless revealed new information about the nature of the THF solvent shell in these three samples.

7.6 Full Set of 2D-IR Data

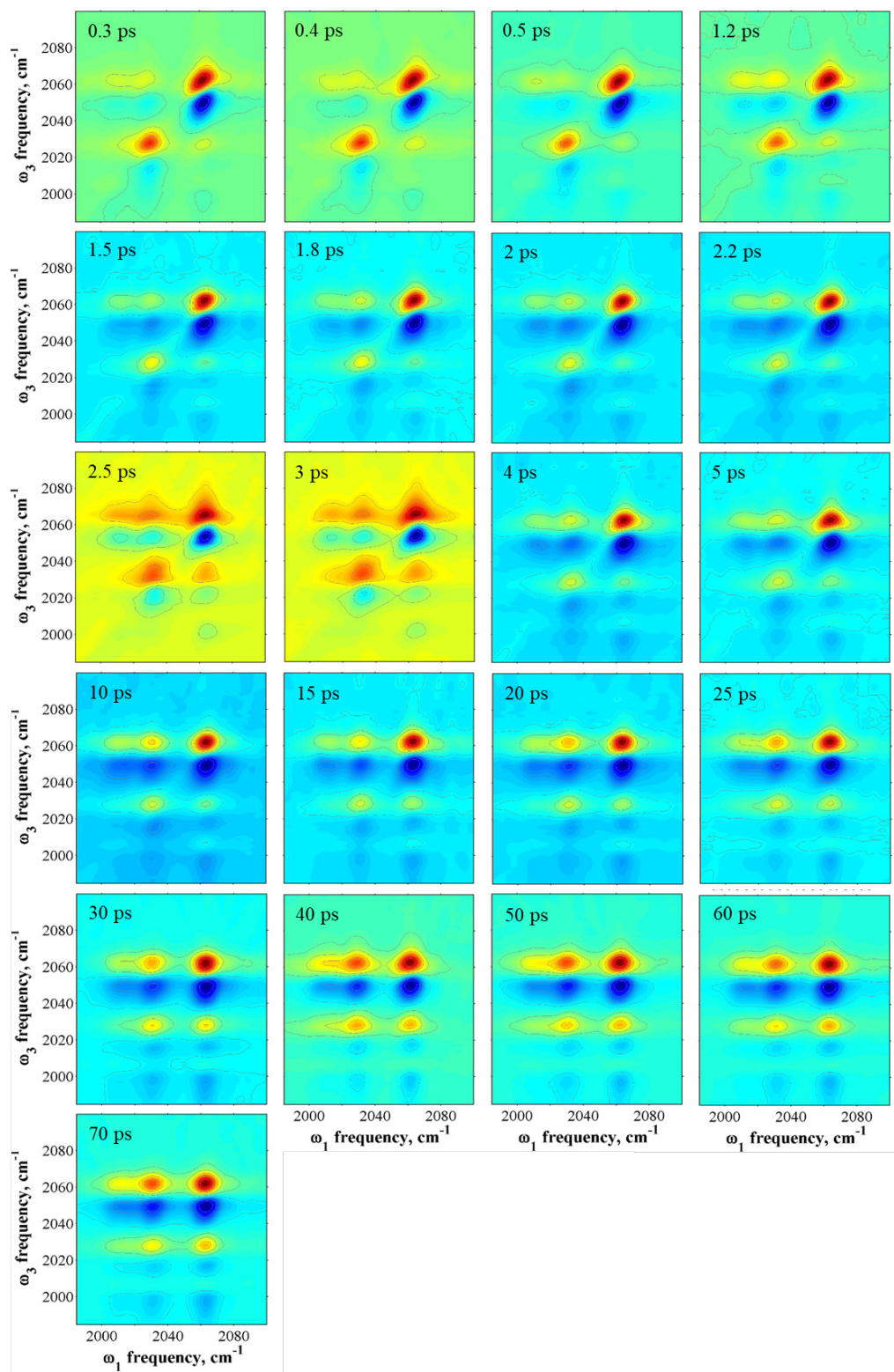


Figure 7.5. 2D-IR spectra of the carbonyl stretches of $\text{Ru}_3\text{CO}_{12}$ in THF at a range of T_{ws} .

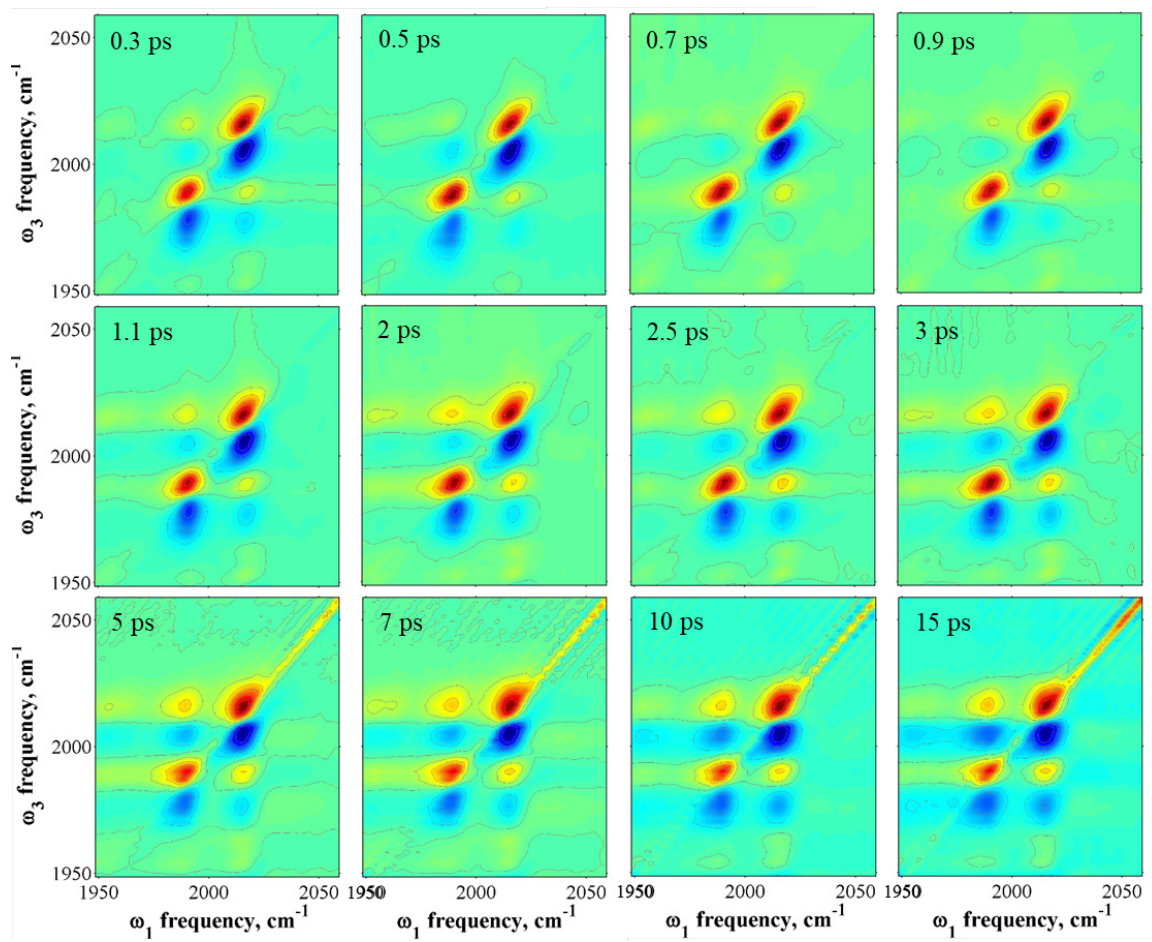


Figure 7.6. 2D-IR spectra of the carbonyl stretches of sol-gel encapsulated $[\text{HRu}_3(\text{CO})_{11}]^-$ at a range of T_w s.

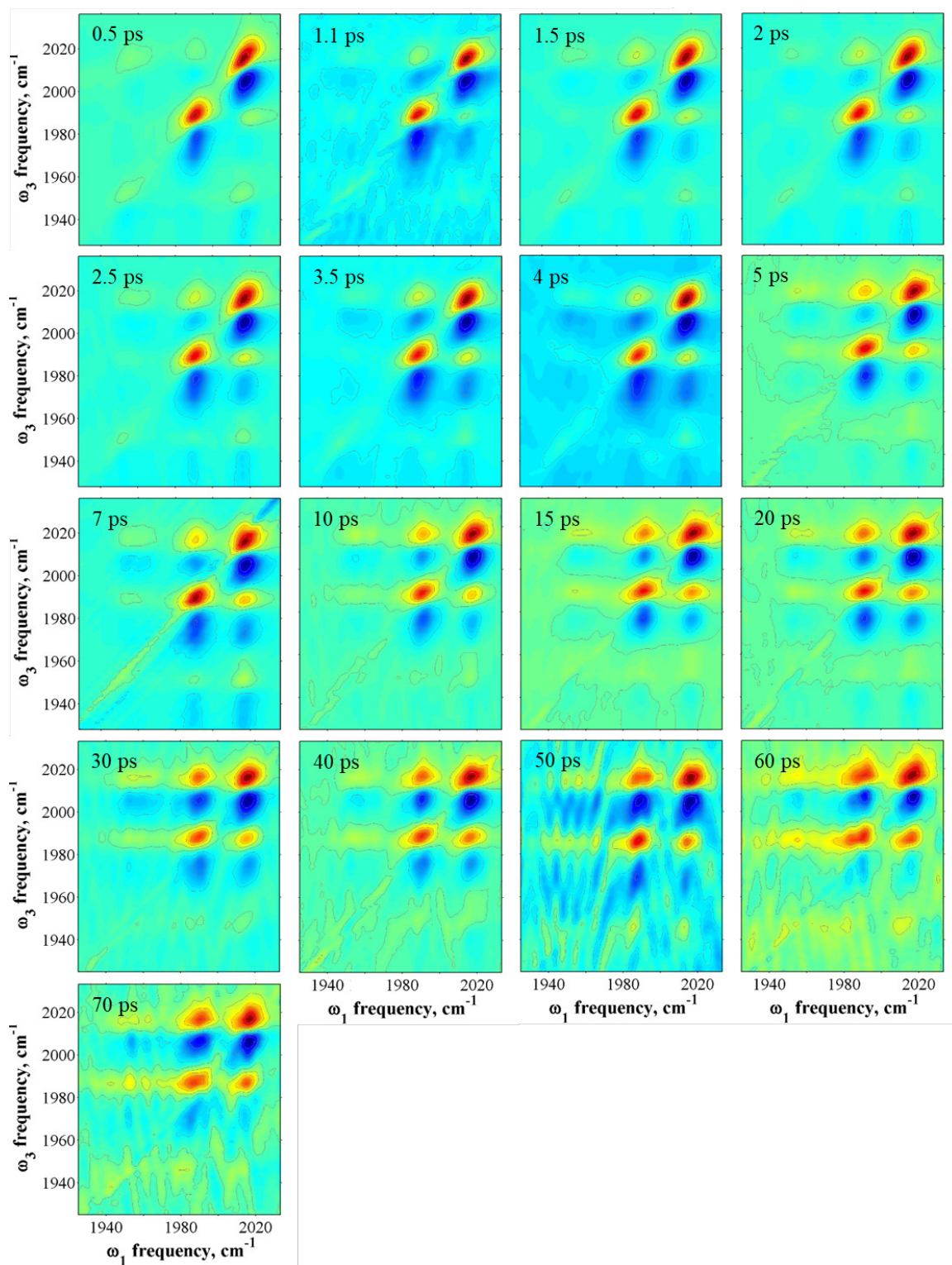


Figure 7.7. 2D-IR spectra of the carbonyl stretches of $[\text{NEt}_4][\text{HRu}_3(\text{CO})_{11}]$ in THF at a range of T_w s.

Bibliography

1. Kim, Y. S.; Liu, L.; Axelsen, P. H.; Hochstrasser, R. M., 2D IR provides evidence for mobile water molecules in β -amyloid fibrils. *Proceedings of the National Academy of Sciences* **2009**, *106* (42), 17751-17756.
2. Eigner, A. A.; Jones, B. H.; Koprucki, B. W.; Massari, A. M., Ground-State Structural Dynamics in Doped and Undoped Polyaniline Films Probed by Two-Dimensional Infrared Vibrational Echo Spectroscopy. *The Journal of Physical Chemistry B* **2011**, *115* (16), 4583-4591.
3. Hamm, P.; Zanni, M., *Concepts and Methods of 2D Infrared Spectroscopy*. Cambridge University Press: Cambridge, 2011.
4. Hamm, P.; Lim, M.; Hochstrasser, R. M., Structure of the Amide I Band of Peptides Measured by Femtosecond Nonlinear-Infrared Spectroscopy. *The Journal of Physical Chemistry B* **1998**, *102* (31), 6123-6138.
5. Giammanco, C. H.; Yamada, S. A.; Kramer, P. L.; Tamimi, A.; Fayer, M. D., Structural and Rotational Dynamics of Carbon Dioxide in 1-Alkyl-3-methylimidazolium Bis(trifluoromethylsulfonyl)imide Ionic Liquids: The Effect of Chain Length. *The Journal of Physical Chemistry B* **2016**, *120* (27), 6698-6711.
6. Huber, C. J.; Massari, A. M., Characterizing Solvent Dynamics in Nanoscopic Silica Sol-Gel Glass Pores by 2D-IR Spectroscopy of an Intrinsic Vibrational Probe. *The Journal of Physical Chemistry C* **2014**, *118* (44), 25567-25578.
7. Spector, I. C.; Schramke, K. S.; Kortshagen, U. R.; Massari, A. M., Measuring Dopant-Modulated Vibrational Energy Transfer over the Surface of Silicon Nanoparticles by 2D-IR Spectroscopy. *The Journal of Physical Chemistry C* **2018**, *122* (15), 8693-8698.
8. Chalk, S.; McEwen, L., The IUPAC Gold Book. *Chemistry International* **2017**, 39.
9. Reichardt, C., *Solvents and solvent effects in organic chemistry*. 4th, updated and enl. / Christian Reichardt and Thomas Welton.. ed.; Weinheim : Wiley-VCH: Weinheim, 2010.
10. Faeder, J.; Ladanyi, B. M., Molecular Dynamics Simulations of the Interior of Aqueous Reverse Micelles. *The Journal of Physical Chemistry B* **2000**, *104* (5), 1033-1046.
11. Stark, J., Observation of the Separation of Spectral Lines by an Electric Field. *Nature* **1913**, *92* (2301), 401-401.
12. Andrews, S. S.; Boxer, S. G., Vibrational Stark Effects of Nitriles I. Methods and Experimental Results. *The Journal of Physical Chemistry A* **2000**, *104* (51), 11853-11863.
13. Andrews, S. S.; Boxer, S. G., Vibrational Stark Effects of Nitriles II. Physical Origins of Stark Effects from Experiment and Perturbation Models. *The Journal of Physical Chemistry A* **2002**, *106* (3), 469-477.

14. Fried, S. D.; Boxer, S. G., Measuring Electric Fields and Noncovalent Interactions Using the Vibrational Stark Effect. *Accounts of Chemical Research* **2015**, *48* (4), 998-1006.
15. Verma, N.; Tao, Y.; Zou, W.; Chen, X.; Chen, X.; Freindorf, M.; Kraka, E., A Critical Evaluation of Vibrational Stark Effect (VSE) Probes with the Local Vibrational Mode Theory. *Sensors (Basel, Switzerland)* **2020**, *20* (8), 2358.
16. Hiemenz, P. C.; Lodge, T. P., *Polymer Chemistry*. Taylor & Francis Group: Baton Rouge, UNITED STATES, 2007.
17. Balani, K., *Biosurfaces : a materials science and engineering perspective*. ACerS-Wiley: Hoboken, New Jersey, 2014.
18. Smith, G. D.; Bedrov, D., Relationship between the α - and β -relaxation processes in amorphous polymers: Insight from atomistic molecular dynamics simulations of 1,4-polybutadiene melts and blends. *Journal of Polymer Science Part B: Polymer Physics* **2007**, *45* (6), 627-643.
19. Ashby, M. F., *Engineering materials 1 : an introduction to properties, applications, and design*. 4th ed.. ed.; Boston, Mass. : Butterworth-Heinemann: Boston, Mass., 2012.
20. White, R. P.; Lipson, J. E. G., Polymer Free Volume and Its Connection to the Glass Transition. *Macromolecules* **2016**, *49* (11), 3987-4007.
21. Cohen, M. H.; Turnbull, D., Molecular transport in liquids and glasses. *The Journal of chemical physics* **1959**, *31* (5), 1164-1169.
22. Ramesh, N.; Davis, P. K.; Zielinski, J. M.; Danner, R. P.; Duda, J. L., Application of free-volume theory to self diffusion of solvents in polymers below the glass transition temperature: A review. *Journal of Polymer Science Part B: Polymer Physics* **2011**, *49* (23), 1629-1644.
23. Takeuchi, H.; Okazaki, K., Molecular dynamics simulation of diffusion of simple gas molecules in a short chain polymer. *The Journal of Chemical Physics* **1990**, *92* (9), 5643-5652.
24. Charati, S. G.; Stern, S. A., Diffusion of Gases in Silicone Polymers: Molecular Dynamics Simulations. *Macromolecules* **1998**, *31* (16), 5529-5535.
25. Lima, M.; Candelaresi, M.; Foggi, P., 2D-IR spectroscopy: an additional dimension to investigate ultrafast structural dynamics. *Journal of Raman Spectroscopy* **2013**, *44* (10), 1470-1477.
26. Lim, S. Y.; Tsotsis, T. T.; Sahimi, M., Molecular simulation of diffusion and sorption of gases in an amorphous polymer. *The Journal of Chemical Physics* **2003**, *119* (1), 496-504.
27. DiBenedetto, A. T.; Paul, D. R., An interpretation of gaseous diffusion through polymers using fluctuation theory. *Journal of polymer science. Part A. General papers* **1964**, *2* (2), 1001-1015.
28. Tan, H.-S.; Piletic, I. R.; Fayer, M. D., Orientational dynamics of water confined on a nanometer length scale in reverse micelles. *The Journal of Chemical Physics* **2005**, *122* (17), 174501.
29. Shears, M. F.; Williams, G., Molecular dynamics of the supercooled liquid state. Low frequency dielectric relaxation of benzophenone, cyclohexanone and fenchone in o-

- terphenyl. *Journal of the Chemical Society, Faraday Transactions 2: Molecular and Chemical Physics* **1973**, 69 (0), 1050-1059.
30. Warchol, M. P.; Vaughan, W. E., Dielectric relaxation by restricted rotational diffusion. *Advances in Molecular Relaxation and Interaction Processes* **1978**, 13 (4), 317-330.
31. Wang, C. C.; Pecora, R., Time-correlation functions for restricted rotational diffusion. *The Journal of Chemical Physics* **1980**, 72 (10), 5333-5340.
32. Kinoshita, K.; Kawato, S.; Ikegami, A., A theory of fluorescence polarization decay in membranes. *Biophysical journal* **1977**, 20 (3), 289-305.
33. Lipari, G.; Szabo, A., Effect of librational motion on fluorescence depolarization and nuclear magnetic resonance relaxation in macromolecules and membranes. *Biophysical journal* **1980**, 30 (3), 489-506.
34. Giammanco, C. H.; Kramer, P. L.; Yamada, S. A.; Nishida, J.; Tamimi, A.; Fayer, M. D., Carbon dioxide in an ionic liquid: Structural and rotational dynamics. *The Journal of Chemical Physics* **2016**, 144 (10), 104506.
35. Shin, J. Y.; Yamada, S. A.; Fayer, M. D., Carbon Dioxide in a Supported Ionic Liquid Membrane: Structural and Rotational Dynamics Measured with 2D IR and Pump-Probe Experiments. *Journal of the American Chemical Society* **2017**, 139 (32), 11222-11232.
36. Tan, H.-S.; Piletic, I. R.; Fayer, M. D., Polarization selective spectroscopy experiments: methodology and pitfalls. *J. Opt. Soc. Am. B* **2005**, 22 (9), 2009-2017.
37. Tan, H. S.; Piletic, I. R.; Fayer, M. D., Orientational dynamics of water confined on a nanometer length scale in reverse micelles. *J. Chem. Phys.* **2005**, 122 (17), 057405.
38. Kramer, P. L.; Giammanco, C. H.; Fayer, M. D., Dynamics of water, methanol, and ethanol in a room temperature ionic liquid. *The Journal of chemical physics* **2015**, 142 (21), 212408-212408.
39. Moilanen, D. E.; Fenn, E. E.; Wong, D.; Fayer, M. D., Water dynamics in large and small reverse micelles: From two ensembles to collective behavior. *The Journal of chemical physics* **2009**, 131 (1), 014704-014704-9.
40. Sánchez-Bajo, F.; Cumbreira, F. L., The Use of the Pseudo-Voigt Function in the Variance Method of X-ray Line-Broadening Analysis. *Journal of Applied Crystallography* **1997**, 30 (4), 427-430.
41. Stancik, A. L.; Brauns, E. B., A simple asymmetric lineshape for fitting infrared absorption spectra. *Vibrational Spectroscopy* **2008**, 47 (1), 66-69.
42. Ma, Y.; Li, H.; Gu, Z.; Ubachs, W. M. G.; Yu, Y.; Huang, J.; Zhou, B.; Wang, Y.; Liang, K., Analysis of Rayleigh-Brillouin spectral profiles and Brillouin shifts in nitrogen gas and air. *Opt. Express* **2014**, 22 (2), 2092-2104.
43. Yariv, A.; Yeh, P., *Photonics: Optical Electronics in Modern Communications (The Oxford Series in Electrical and Computer Engineering)*. Oxford University Press, Inc.: 2006.
44. Kenkre, V. M.; Tokmakoff, A.; Fayer, M. D., Theory of vibrational relaxation of polyatomic molecules in liquids. *The Journal of Chemical Physics* **1994**, 101 (12), 10618-10629.

45. Wynne, K.; Hochstrasser, R. M., The theory of ultrafast vibrational spectroscopy. *Chemical Physics* **1995**, *193* (3), 211-236.
46. Olson, C. M.; Grofe, A.; Huber, C. J.; Spector, I. C.; Gao, J.; Massari, A. M., Enhanced vibrational solvatochromism and spectral diffusion by electron rich substituents on small molecule silanes. *The Journal of Chemical Physics* **2017**, *147* (12), 124302.
47. Fayer, M. D., *Elements of Quantum Mechanics*. Oxford University Press: 2001.
48. Kwak, K.; Park, S.; Finkelstein, I. J.; Fayer, M. D., Frequency-frequency correlation functions and apodization in two-dimensional infrared vibrational echo spectroscopy: A new approach. *The Journal of Chemical Physics* **2007**, *127* (12), 124503.
49. Eigner, A. A.; Anglin, T. C.; Massari, A. M., 2D-IR Studies of Annealing-Induced Changes to Structural Dynamics in Organic Semiconductor Thin Films. *The Journal of Physical Chemistry C* **2010**, *114* (28), 12308-12315.
50. Maine, P.; Strickland, D.; Bado, P.; Pessot, M.; Mourou, G., Generation of ultrahigh peak power pulses by chirped pulse amplification. *IEEE Journal of Quantum Electronics* **1988**, *24* (2), 398-403.
51. Anglin, T. C.; O'Brien, D. B.; Massari, A. M., Monitoring the Charge Accumulation Process in Polymeric Field-Effect Transistors via in Situ Sum Frequency Generation. *The Journal of Physical Chemistry C* **2010**, *114* (41), 17629-17637.
52. Jones, B. H.; Huber, C. J.; Massari, A. M., Solvation Dynamics of Vaska's Complex by 2D-IR Spectroscopy. *The Journal of Physical Chemistry C* **2011**, *115* (50), 24813-24822.
53. Eckbreth, A. C., BOXCARS: Crossed-beam phase-matched CARS generation in gases. *Applied Physics Letters* **1978**, *32* (7), 421-423.
54. Fenn, E. E.; Fayer, M. D., Extracting 2D IR frequency-frequency correlation functions from two component systems. *The Journal of Chemical Physics* **2011**, *135* (7), 074502.
55. Kwak, K.; Rosenfeld, D. E.; Fayer, M. D., Taking apart the two-dimensional infrared vibrational echo spectra: More information and elimination of distortions. *The Journal of Chemical Physics* **2008**, *128* (20), 204505.
56. Mukamel, S., *Principles of nonlinear optical spectroscopy*. Oxford University Press: Oxford, 1999.
57. Nesbitt, D. J.; Field, R. W., Vibrational Energy Flow in Highly Excited Molecules: Role of Intramolecular Vibrational Redistribution. *The Journal of Physical Chemistry* **1996**, *100* (31), 12735-12756.
58. Zare, R. N., Laser Control of Chemical Reactions. *Science* **1998**, *279* (5358), 1875-1879.
59. Sinha, A.; Hsiao, M. C.; Crim, F. F., Controlling bimolecular reactions: Mode and bond selected reaction of water with hydrogen atoms. *The Journal of Chemical Physics* **1991**, *94* (7), 4928-4935.
60. Sinha, A.; Hsiao, M. C.; Crim, F. F., Bond-selected bimolecular chemistry: $\text{H}+\text{HOD}(4\nu\text{OH})\rightarrow\text{OD}+\text{H}_2$. *The Journal of Chemical Physics* **1990**, *92* (10), 6333-6335.

61. Crim, F. F., Bond-Selected Chemistry: Vibrational State Control of Photodissociation and Bimolecular Reaction. *The Journal of Physical Chemistry* **1996**, *100* (31), 12725-12734.
62. Powers, D. E.; Hopkins, J. B.; Smalley, R. E., Vibrational relaxation in jet-cooled phenylalkynes. *The Journal of Chemical Physics* **1981**, *74* (11), 5971-5976.
63. Swamy, K. N.; Hase, W. L., The heavy-atom effect in intramolecular vibrational energy transfer. *The Journal of Chemical Physics* **1985**, *82* (1), 123-133.
64. Uzer, T.; Hynes, J. T., Intramolecular energy transfer in simple model organometallics. *The Journal of Physical Chemistry* **1986**, *90* (16), 3524-3527.
65. Dlott, D. D.; Fayer, M. D.; Hill, J. R.; Rella, C. W.; Suslick, K. S.; Ziegler, C. J., Vibrational relaxation in metalloporphyrin CO complexes. *Journal of the American Chemical Society* **1996**, *118* (33), 7853-7854.
66. Elsaesser, T.; Kaiser, W., Vibrational and Vibronic Relaxation of Large Polyatomic Molecules in Liquids. *Annual Review of Physical Chemistry* **1991**, *42* (1), 83-107.
67. Tokmakoff, A.; Sauter, B.; Fayer, M. D., Temperature-dependent vibrational relaxation in polyatomic liquids: Picosecond infrared pump-probe experiments. *The Journal of Chemical Physics* **1994**, *100* (12), 9035-9043.
68. Rubtsov, I. V., Relaxation-Assisted Two-Dimensional Infrared (RA 2DIR) Method: Accessing Distances over 10 Å and Measuring Bond Connectivity Patterns. *Accounts of Chemical Research* **2009**, *42* (9), 1385-1394.
69. Lyding, J. W.; Hess, K.; Kizilyalli, I. C., Reduction of hot electron degradation in metal oxide semiconductor transistors by deuterium processing. *Applied Physics Letters* **1996**, *68* (18), 2526-2528.
70. Rogers, P. M.; Derek C.; Frank, J.P.; Tyler, S.C.; Rowland, S.F.; Non-RRKM Decomposition in A Chemical Activation System: Thermal Atomic Fluorine Plus Tetraallyl Tin. *Chem. Phys. Lett.* **1982**, *89* (1), 9-12.
71. Arrivo, S. M.; Heilweil, E. J., Conservation of Vibrational Excitation During Hydrogen-Bonding Reactions. *The Journal of Physical Chemistry* **1996**, *100* (29), 11975-11983.
72. McGlynn, S. P.; Sunseri, R.; Christodouleas, N., External Heavy-Atom Spin-Orbital Coupling Effect. I. The Nature of the Interaction. *The Journal of Chemical Physics* **1962**, *37* (8), 1818-1824.
73. Bian, H.; Li, J.; Wen, X.; Zheng, J., Mode-specific intermolecular vibrational energy transfer. I. Phenyl selenocyanate and deuterated chloroform mixture. *The Journal of Chemical Physics* **2010**, *132* (18), 184505.
74. Bian, H.; Wen, X.; Li, J.; Zheng, J., Mode-specific intermolecular vibrational energy transfer. II. Deuterated water and potassium selenocyanate mixture. *The Journal of Chemical Physics* **2010**, *133* (3), 034505.
75. Lenchenkov, V.; She, C.; Lian, T., Vibrational Relaxation of CN Stretch of Pseudo-Halide Anions (OCN-, SCN-, and SeCN-) in Polar Solvents. *The Journal of Physical Chemistry B* **2006**, *110* (40), 19990-19997.
76. Levin, D. E.; Schmitz, A. J.; Hines, S. M.; Hines, K. J.; Tucker, M. J.; Brewer, S. H.; Fenlon, E. E., Synthesis and evaluation of the sensitivity and vibrational lifetimes

- of thiocyanate and selenocyanate infrared reporters. *RSC Advances* **2016**, *6* (43), 36231-36237.
77. Park, K.-H.; Jeon, J.; Park, Y.; Lee, S.; Kwon, H.-J.; Joo, C.; Park, S.; Han, H.; Cho, M., Infrared Probes Based on Nitrile-Derivatized Prolines: Thermal Insulation Effect and Enhanced Dynamic Range. *The Journal of Physical Chemistry Letters* **2013**, *4* (13), 2105-2110.
78. Sokolowsky, K. P.; Fayer, M. D., Dynamics in the Isotropic Phase of Nematogens Using 2D IR Vibrational Echo Measurements on Natural-Abundance ^{13}C N and Extended Lifetime Probes. *The Journal of Physical Chemistry B* **2013**, *117* (48), 15060-15071.
79. Lopez, V.; Marcus, R. A., Heavy mass barrier to intramolecular energy transfer. *Chemical Physics Letters* **1982**, *93* (3), 232-234.
80. Wrigley, S. P.; Oswald, D. A.; Rabinovitch, B. S., On the question of heavy-atom blocking of intramolecular vibrational energy transfer. *Chemical Physics Letters* **1984**, *104* (6), 521-525.
81. Wrigley, S. P. R., B.S, On Heavy-Atom Blocking of Intramolecular Vibrational Energy Transfer in The 4-(Trimethyl Tin)Butyl-2 Radical *Chem. Phys. Lett.* **1983**, *98* (4), 386-392.
82. Stuchebrukhov, A. A.; Marcus, R. A., Theoretical study of intramolecular vibrational relaxation of acetylenic CH vibration for $v=1$ and 2 in large polyatomic molecules $(\text{CX}_3)_3\text{YCCH}$, where $\text{X}=\text{H}$ or D and $\text{Y}=\text{C}$ or Si . *The Journal of Chemical Physics* **1993**, *98* (8), 6044-6061.
83. Uzer, T.; Hynes, J. T., Dissociation of remote bonds by overtone excitation: A model study of heavy-atom blocking. *Chemical Physics* **1989**, *139* (1), 163-170.
84. Leich, V.; Spaniol, T. P.; Okuda, J., Potassium-Catalyzed Hydrosilylation of Activated Olefins: Evidence for a Silyl Migration Mechanism. *Organometallics* **2016**, *35* (9), 1179-1182.
85. Jones, B. H.; Huber, C. J.; Massari, A. M., Solvent-Mediated Vibrational Energy Relaxation from Vaska's Complex Adducts in Binary Solvent Mixtures. *The Journal of Physical Chemistry A* **2013**, *117* (29), 6150-6157.
86. Frisch, M. J.; Trucks, G. W.; Schlegel, H. B.; Scuseria, G. E.; Robb, M. A.; Cheeseman, J. R.; Scalmani, G.; Barone, V.; Petersson, G. A.; Nakatsuji, H.; Li, X.; Caricato, M.; Marenich, A. V.; Bloino, J.; Janesko, B. G.; Gomperts, R.; Mennucci, B.; Hratchian, H. P.; Ortiz, J. V.; Izmaylov, A. F.; Sonnenberg, J. L.; Williams; Ding, F.; Lipparini, F.; Egidi, F.; Goings, J.; Peng, B.; Petrone, A.; Henderson, T.; Ranasinghe, D.; Zakrzewski, V. G.; Gao, J.; Rega, N.; Zheng, G.; Liang, W.; Hada, M.; Ehara, M.; Toyota, K.; Fukuda, R.; Hasegawa, J.; Ishida, M.; Nakajima, T.; Honda, Y.; Kitao, O.; Nakai, H.; Vreven, T.; Throssell, K.; Montgomery Jr., J. A.; Peralta, J. E.; Ogliaro, F.; Bearpark, M. J.; Heyd, J. J.; Brothers, E. N.; Kudin, K. N.; Staroverov, V. N.; Keith, T. A.; Kobayashi, R.; Normand, J.; Raghavachari, K.; Rendell, A. P.; Burant, J. C.; Iyengar, S. S.; Tomasi, J.; Cossi, M.; Millam, J. M.; Klene, M.; Adamo, C.; Cammi, R.; Ochterski, J. W.; Martin, R. L.; Morokuma, K.; Farkas, O.; Foresman, J. B.; Fox, D. J. *Gaussian 09 Rev. A.02*, Wallingford, CT, 2009.

87. Lederman, S. M.; López, V.; Fairén, V.; Voth, G. A.; Marcus, R. A., Vibrational energy redistribution across a heavy atom. *Chemical Physics* **1989**, *139* (1), 171-184.
88. King, J. T. Anna, J.M.; Kubarych, K.J, Solvent-hindered Intramolecular Vibrational Redistribution. *Phys. Chem. Chem. Phys.* **2011**, *13*, 5579-5583.
89. Zhang, X. P.; Zhang, X. C.; Dong, H. F.; Zhao, Z. J.; Zhang, S. J.; Huang, Y., Carbon capture with ionic liquids: overview and progress. *Energy & Environmental Science* **2012**, *5* (5), 6668-6681.
90. Roy, S. C.; Varghese, O. K.; Paulose, M.; Grimes, C. A., Toward Solar Fuels: Photocatalytic Conversion of Carbon Dioxide to Hydrocarbons. *Acs Nano* **2010**, *4* (3), 1259-1278.
91. Munkejord, S. T.; Hammer, M.; Lovseth, S. W., CO₂ transport: Data and models - A review. *Applied Energy* **2016**, *169*, 499-523.
92. Mikkelsen, M.; Jorgensen, M.; Krebs, F. C., The teraton challenge. A review of fixation and transformation of carbon dioxide. *Energy & Environmental Science* **2010**, *3* (1), 43-81.
93. Habisreutinger, S. N.; Schmidt-Mende, L.; Stolarczyk, J. K., Photocatalytic Reduction of CO₂ on TiO₂ and Other Semiconductors. *Angewandte Chemie-International Edition* **2013**, *52* (29), 7372-7408.
94. Konno, T.; Ozaki, Y., Infrared spectroscopy of ((CO₂)-C-12-O-18)(2) and isotope effect on the vibrationally averaged structure of (CO₂)(2). *Chem. Phys. Lett.* **2004**, *394* (1-3), 198-202.
95. O'Neill, J. A.; Wang, C. X.; Cai, J. Y.; Flynn, G. W.; Weston, R. E., ROTATIONALLY RESOLVED HOT ATOM COLLISIONAL EXCITATION OF CO₂ 0001 AND 0002 STRETCHING VIBRATIONS BY TIME-RESOLVED DIODE-LASER SPECTROSCOPY. *J. Chem. Phys.* **1988**, *88* (10), 6240-6254.
96. Walsh, M. A.; England, T. H.; Dyke, T. R.; Howard, B. J., PULSED MOLECULAR-BEAM INFRARED-ABSORPTION SPECTROSCOPY OF CO₂ DIMER. *Chem. Phys. Lett.* **1987**, *142* (3-4), 265-270.
97. Morgen, M.; Price, W.; Hunziker, L.; Ludowise, P.; Blackwell, M.; Chen, Y., FEMTOSECOND RAMAN-INDUCED POLARIZATION SPECTROSCOPY STUDIES OF ROTATIONAL COHERENCE IN O₂, N₂ AND CO₂. *Chem. Phys. Lett.* **1993**, *209* (1-2), 1-9.
98. *Spectroscopy: Volume 2*. Chapman and Hall: London, 1976; Vol. 2.
99. Mandal, A.; Pack, G. N.; Shah, P. P.; Erramilli, S.; Ziegler, L. D., Ultrafast Two-Dimensional Infrared Spectroscopy of a Quasifree Rotor: J Scrambling and Perfectly Anticorrelated Cross Peaks. *Phys. Rev. Lett.* **2018**, *120* (10), 6.
100. Ng Pack, G.; Rotondaro, M. C.; Shah, P. P.; Mandal, A.; Erramilli, S.; Ziegler, L. D., Two-dimensional infrared spectroscopy from the gas to liquid phase: density dependent J-scrambling, vibrational relaxation, and the onset of liquid character. *Physical Chemistry Chemical Physics* **2019**, *21* (38), 21249-21261.
101. Wakatsuki, K.; Fuss, S. P.; Hamins, A.; Nyden, M. R., A technique for extrapolating absorption coefficient measurements to high temperatures. *Proceedings of the Combustion Institute* **2005**, *30* (1), 1565-1573.

102. Jones, B. H.; Huber, C. J.; Massari, A. M., Solvent-Mediated Vibrational Energy Relaxation from Vaska's Complex Adducts in Binary Solvent Mixtures. *J. Phys. Chem. A* **2013**, *117* (29), 6150-6157.
103. Jones, B. H.; Huber, C. J.; Massari, A. M., Solvation Dynamics of Vaska's Complex by 2D-IR Spectroscopy. *J. Phys. Chem. C* **2011**, *115* (50), 24813-24822.
104. Eckbreth, A. C., Boxcars - Crossed-Beam Phase-Matched Cars Generation in Gases. *Appl. Phys. Lett.* **1978**, *32* (7), 421-423.
105. IUPAC, *Tables of wavenumbers for the calibration of infra-red spectrometers*. Butterworths: Washington, 1961; p 163.
106. Brinzer, T.; Berquist, E. J.; Ren, Z.; Dutta, S.; Johnson, C. A.; Krisher, C. S.; Lambrecht, D. S.; Garrett-Roe, S., Ultrafast vibrational spectroscopy (2D-IR) of CO₂ in ionic liquids: Carbon capture from carbon dioxide's point of view. *The Journal of Chemical Physics* **2015**, *142* (21), 212425.
107. Hamm, P.; Zanni, M. T., *Concepts and Methods of 2D Infrared Spectroscopy*. Cambridge University Press: Cambridge, 2011.
108. Kwon, Y.; Lee, C.; Park, S., Effect of ion-molecule interaction on fermi-resonance in acetonitrile studied by ultrafast vibrational spectroscopy. *Chem. Phys.* **2014**, *445*, 38-45.
109. Ogren, P. J., Using the asymmetric stretch band of atmospheric CO₂ to obtain the C=O bond length. *J. Chem. Educ.* **2002**, *79* (1), 117-119.
110. Herzberg, G., *Molecular Spectra and Molecular Structure III. Electronic Spectra and Electronic Structure of Polyatomic Molecules*. Van Nostrand: New York, 1966.
111. Buback, M.; Schweer, J.; Tups, H., Near Infrared Absorption of Pure Carbon Dioxide up to 3100 bar and 500 K. II. Wavenumber Range 5600 cm⁻¹ to 7400 cm⁻¹. *Zeitschrift für Naturforschung A* **1986**, *41* (3), 512-518.
112. Realmonte, G.; Drouet, L.; Gambhir, A.; Glynn, J.; Hawkes, A.; Köberle, A. C.; Tavoni, M., An inter-model assessment of the role of direct air capture in deep mitigation pathways. *Nature Communications* **2019**, *10* (1), 3277.
113. Strefler, J. B., N.; Kriegler, E.; Popp, A.; Giannousakis, A.; Edenhofer, O.; , Between Scylla and Charybdis: Delayed mitigation narrows the passage between large-scale CDR and high costs. *Environ. Res. Lett.* **2018**, *13* (4).
114. Hussain, M.; Koenig, A., Mixed-Matrix Membrane for Gas Separation: Polydimethylsiloxane Filled with Zeolite. *Chemical Engineering & Technology* **2012**, *35*.
115. Liu, M.; Nothling, M. D.; Webley, P. A.; Fu, Q.; Qiao, G. G., Postcombustion Carbon Capture Using Thin-Film Composite Membranes. *Accounts of Chemical Research* **2019**, *52* (7), 1905-1914.
116. Charati, S. G.; Stern, S. A., Diffusion of Gases in Silicone Polymers: Molecular Dynamics Simulations. *Macromolecules* **1998**, *31* (16), 5529-5535.
117. Freeman, B. D., Basis of Permeability/Selectivity Tradeoff Relations in Polymeric Gas Separation Membranes. *Macromolecules* **1999**, *32* (2), 375-380.
118. Kanaya, T.; Tsukushi, I.; Kaji, K.; Sakaguchi, T.; Kwak, G.; Masuda, T., Role of Local Dynamics in the Gas Permeability of Glassy Substituted Polyacetylenes. A Quasielastic Neutron Scattering Study. *Macromolecules* **2002**, *35* (14), 5559-5564.

119. Sonnenburg, J.; Gao, J.; Weiner, J. H., Molecular dynamics simulations of gas diffusion through polymer networks. *Macromolecules* **1990**, *23* (21), 4653-4657.
120. Tamai, Y.; Tanaka, H.; Nakanishi, K., Molecular Simulation of Permeation of Small Penetrants through Membranes. 1. Diffusion Coefficients. *Macromolecules* **1994**, *27* (16), 4498-4508.
121. Frisch, H. L.; Stern, S. A., DIFFUSION OF SMALL MOLECULES IN POLYMERS. *Crc Critical Reviews in Solid State and Materials Sciences* **1983**, *11* (2), 123-187.
122. Stern, S. A., POLYMERS FOR GAS SEPARATIONS - THE NEXT DECADE. *Journal of Membrane Science* **1994**, *94*, 1-65.
123. Stern, S. A.; Trohalaki, S., FUNDAMENTALS OF GAS-DIFFUSION IN RUBBERY AND GLASSY-POLYMERS. *ACS Symp. Ser.* **1990**, *423*, 22-59.
124. Hiemenz, P. C., *Polymer chemistry*. Second edition.. ed.; Boca Raton, FL : CRC Press: Boca Raton, FL, 2007.
125. Yamaguchi, T.; Wang, B. G.; Matsuda, E.; Suzuki, S.; Nakao, S. I., Prediction and estimation of solvent diffusivities in polyacrylate and polymethacrylates. *J. Polym. Sci. Pt. B-Polym. Phys.* **2003**, *41* (12), 1393-1400.
126. Higuchi, A.; Nakajima, T.; Morisato, A.; Ando, M.; Nagai, K.; Nakagawa, T., Estimation of diffusion and permeability coefficients of CO₂ in polymeric membranes by FTIR method. *J. Polym. Sci. Pt. B-Polym. Phys.* **1996**, *34* (13), 2153-2160.
127. Mogri, Z.; Paul, D. R., Gas sorption and transport in poly(alkyl (meth)acrylate)s. II. Sorption and diffusion properties. *Polymer* **2001**, *42* (18), 7781-7789.
128. Kazarian, S. G.; Vincent, M. F.; Bright, F. V.; Liotta, C. L.; Eckert, C. A., Specific Intermolecular Interaction of Carbon Dioxide with Polymers. *Journal of the American Chemical Society* **1996**, *118* (7), 1729-1736.
129. Shieh, Y.-T.; Liu, K.-H., Solubility of CO₂ in Glassy PMMA and PS over a Wide Pressure Range: The Effect of Carbonyl Groups. *Journal of Polymer Research* **2002**, *9* (2), 107-113.
130. Flichy, N. M. B.; Kazarian, S. G.; Lawrence, C. J.; Briscoe, B. J., An ATR-IR Study of Poly (Dimethylsiloxane) under High-Pressure Carbon Dioxide: Simultaneous Measurement of Sorption and Swelling. *The Journal of Physical Chemistry B* **2002**, *106* (4), 754-759.
131. Goodman, A. L., A Comparison Study of Carbon Dioxide Adsorption on Polydimethylsiloxane, Silica Gel, and Illinois No. 6 Coal Using in Situ Infrared Spectroscopy. *Energy & Fuels* **2009**, *23* (2), 1101-1106.
132. Kwak, K.; Park, S.; Finkelstein, I. J.; Fayer, M. D., Frequency-frequency correlation functions and apodization in two-dimensional infrared vibrational echo spectroscopy: A new approach. *J. Chem. Phys.* **2007**, *127* (12), 124503.
133. Kwak, K.; Rosenfeld, D. E.; Fayer, M. D., Taking apart the two-dimensional infrared vibrational echo spectra: More information and elimination of distortions. *J. Chem. Phys.* **2008**, *128* (20), 204505.
134. Tan, H. S.; Piletic, I. R.; Fayer, M. D., Polarization selective spectroscopy experiments: methodology and pitfalls. *J. Opt. Soc. Am. B* **2005**, *22* (9), 2009-2017.

135. Giammanco, C. H.; Kramer, P. L.; Yamada, S. A.; Nishida, J.; Tamimi, A.; Fayer, M. D., Coupling of Carbon Dioxide Stretch and Bend Vibrations Reveals Thermal Population Dynamics in an Ionic Liquid. *The Journal of Physical Chemistry B* **2016**, *120* (3), 549-556.
136. Fayer, M. D.; Moilanen, D. E.; Wong, D.; Rosenfeld, D. E.; Fenn, E. E.; Park, S., Water Dynamics in Salt Solutions Studied with Ultrafast Two-Dimensional Infrared (2D IR) Vibrational Echo Spectroscopy. *Acc. Chem. Res.* **2009**, *42* (9), 1210-1219.
137. Oxtoby, D. W., Vibrational-Relaxation in Liquids. *Annu. Rev. Phys. Chem.* **1981**, *32*, 77-101.
138. Kenkre, V. M.; Tokmakoff, A.; Fayer, M. D., Theory of Vibrational-Relaxation of Polyatomic-Molecules in Liquids. *J. Chem. Phys.* **1994**, *101* (12), 10618-10629.
139. Lipari, G.; Szabo, A., EFFECT OF LIBRATIONAL MOTION ON FLUORESCENCE DEPOLARIZATION AND NUCLEAR MAGNETIC-RESONANCE RELAXATION IN MACROMOLECULES AND MEMBRANES. *Biophys. J.* **1980**, *30* (3), 489-506.
140. Wang, C. C.; Pecora, R., TIME-CORRELATION FUNCTIONS FOR RESTRICTED ROTATIONAL DIFFUSION. *J. Chem. Phys.* **1980**, *72* (10), 5333-5340.
141. Baiz, C. R.; McRobbie, P. L.; Anna, J. M.; Geva, E.; Kubarych, K. J., Two-Dimensional Infrared Spectroscopy of Metal Carbonyls. *Acc. Chem. Res.* **2009**, *42* (9), 1395-1404.
142. Fayer, M. D., Dynamics of Liquids, Molecules, and Proteins Measured with Ultrafast 2D IR Vibrational Echo Chemical Exchange Spectroscopy. *Annu. Rev. Phys. Chem.* **2009**, *60*, 21-38.
143. Hamm, P.; Lim, M. H.; Hochstrasser, R. M., Structure of the amide I band of peptides measured by femtosecond nonlinear-infrared spectroscopy. *J. Phys. Chem. B* **1998**, *102* (31), 6123-6138.
144. Jones, B. H.; Massari, A. M., Origins of Spectral Broadening in Iodated Vaska's Complex in Binary Solvent Mixtures. *J. Phys. Chem. B* **2013**, *117* (49), 15741-15749.
145. Khalil, M.; Demirdoven, N.; Tokmakoff, A., Coherent 2D IR spectroscopy: Molecular structure and dynamics in solution. *J. Phys. Chem. A* **2003**, *107* (27), 5258-5279.
146. Gangu, K. K.; Maddila, S.; Mukkamala, S. B.; Jonnalagadda, S. B., A review on contemporary Metal–Organic Framework materials. *Inorganica Chimica Acta* **2016**, *446* (Supplement C), 61-74.
147. Choudary, B. M.; Chakrapani, L.; Ramani, T.; Kumar, K. V.; Kantam, M. L., Direct asymmetric aldol reaction catalyzed by nanocrystalline magnesium oxide. *Tetrahedron* **2006**, *62* (41), 9571-9576.
148. Hartmann, M.; Fischer, M., Amino-functionalized basic catalysts with MIL-101 structure. *Microporous and Mesoporous Materials* **2012**, *164* (Supplement C), 38-43.
149. Luan, Y.; Qi, Y.; Gao, H.; Andriamitantsoa, R. S.; Zheng, N.; Wang, G., A general post-synthetic modification approach of amino-tagged metal-organic frameworks to access efficient catalysts for the Knoevenagel condensation reaction. *Journal of Materials Chemistry A* **2015**, *3* (33), 17320-17331.

150. Lin, J.-M.; He, C.-T.; Liu, Y.; Liao, P.-Q.; Zhou, D.-D.; Zhang, J.-P.; Chen, X.-M., A Metal–Organic Framework with a Pore Size/Shape Suitable for Strong Binding and Close Packing of Methane. *Angewandte Chemie International Edition* **2016**, *55* (15), 4674-4678.
151. Luo, F.; Yan, C.; Dang, L.; Krishna, R.; Zhou, W.; Wu, H.; Dong, X.; Han, Y.; Hu, T.-L.; O’Keeffe, M.; Wang, L.; Luo, M.; Lin, R.-B.; Chen, B., UTSA-74: A MOF-74 Isomer with Two Accessible Binding Sites per Metal Center for Highly Selective Gas Separation. *Journal of the American Chemical Society* **2016**, *138* (17), 5678-5684.
152. Mason, J. A.; Veenstra, M.; Long, J. R., Evaluating metal-organic frameworks for natural gas storage. *Chemical Science* **2014**, *5* (1), 32-51.
153. Mihaylov, M.; Chakarova, K.; Andonova, S.; Drenchev, N.; Ivanova, E.; Pidko, E. A.; Sabetghadam, A.; Seoane, B.; Gascon, J.; Kapteijn, F.; Hadjiivanov, K., Adsorption of CO₂ on MIL-53(Al): FTIR evidence of the formation of dimeric CO₂ species. *Chemical Communications* **2016**, *52* (7), 1494-1497.
154. Plonka, A. M.; Banerjee, D.; Woerner, W. R.; Zhang, Z.; Nijem, N.; Chabal, Y. J.; Li, J.; Parise, J. B., Mechanism of Carbon Dioxide Adsorption in a Highly Selective Coordination Network Supported by Direct Structural Evidence. *Angewandte Chemie International Edition* **2013**, *52* (6), 1692-1695.
155. Gao, M.-L.; Cao, X.-M.; Zhang, Y.-Y.; Qi, M.-H.; Wang, S.-M.; Liu, L.; Han, Z.-B., A bifunctional luminescent europium-organic framework for highly selective sensing of nitrobenzene and 4-aminophenol. *RSC Advances* **2017**, *7* (71), 45029-45033.
156. Pramanik, S.; Hu, Z.; Zhang, X.; Zheng, C.; Kelly, S.; Li, J., A Systematic Study of Fluorescence-Based Detection of Nitroexplosives and Other Aromatics in the Vapor Phase by Microporous Metal–Organic Frameworks. *Chemistry – A European Journal* **2013**, *19* (47), 15964-15971.
157. Wang, K.-M.; Du, L.; Ma, Y.-L.; Zhao, J.-S.; Wang, Q.; Yan, T.; Zhao, Q.-H., Multifunctional chemical sensors and luminescent thermometers based on lanthanide metal-organic framework materials. *CrystEngComm* **2016**, *18* (15), 2690-2700.
158. Wu, J.-J.; Ye, Y.-X.; Qiu, Y.-Y.; Qiao, Z.-P.; Cao, M.-L.; Ye, B.-H., Solvent-Mediated Crystal-to-Crystal Interconversion between Discrete Lanthanide Complexes and One-Dimensional Coordination Polymers and Selective Sensing for Small Molecules. *Inorganic Chemistry* **2013**, *52* (11), 6450-6456.
159. Horcajada, P.; Serre, C.; Maurin, G.; Ramsahye, N. A.; Balas, F.; Vallet-Regí, M.; Sebban, M.; Taulelle, F.; Férey, G., Flexible Porous Metal-Organic Frameworks for a Controlled Drug Delivery. *Journal of the American Chemical Society* **2008**, *130* (21), 6774-6780.
160. Orellana-Tavra, C.; Marshall, R. J.; Baxter, E. F.; Lazaro, I. A.; Tao, A.; Cheetham, A. K.; Forgan, R. S.; Fairen-Jimenez, D., Drug delivery and controlled release from biocompatible metal-organic frameworks using mechanical amorphization. *Journal of Materials Chemistry B* **2016**, *4* (47), 7697-7707.
161. Wu, M.-X.; Yang, Y.-W., Metal–Organic Framework (MOF)-Based Drug/Cargo Delivery and Cancer Therapy. *Advanced Materials* **2017**, *29* (23), 1606134-n/a.

162. Howarth, A. J.; Liu, Y.; Hupp, J. T.; Farha, O. K., Metal-organic frameworks for applications in remediation of oxyanion/cation-contaminated water. *CrystEngComm* **2015**, *17* (38), 7245-7253.
163. Bauer, C. A.; Timofeeva, T. V.; Settersten, T. B.; Patterson, B. D.; Liu, V. H.; Simmons, B. A.; Allendorf, M. D., Influence of Connectivity and Porosity on Ligand-Based Luminescence in Zinc Metal–Organic Frameworks. *Journal of the American Chemical Society* **2007**, *129* (22), 7136-7144.
164. Qiu, Y.; Li, Y.; Peng, G.; Cai, J.; Jin, L.; Ma, L.; Deng, H.; Zeller, M.; Batten, S. R., Cadmium Metal-Directed Three-Dimensional Coordination Polymers: In Situ Tetrazole Ligand Synthesis, Structures, and Luminescent Properties. *Crystal Growth & Design* **2010**, *10* (3), 1332-1340.
165. Rouquerol, J.; Avnir, D.; Fairbridge, C. W.; Everett, D. H., Recommendations for the characterization of porous solids (Technical Report). *Pure & Appl. Chem.* **1994**, *66* (8), 1739-1758.
166. He, Y.; Shang, J.; Gu, Q.; Li, G.; Li, J.; Singh, R.; Xiao, P.; Webley, P. A., Converting 3D rigid metal-organic frameworks (MOFs) to 2D flexible networks via ligand exchange for enhanced CO₂/N₂ and CH₄/N₂ separation. *Chemical Communications* **2015**, *51* (79), 14716-14719.
167. Schneemann, A.; Bon, V.; Schwedler, I.; Senkovska, I.; Kaskel, S.; Fischer, R. A., Flexible metal-organic frameworks. *Chemical Society Reviews* **2014**, *43* (16), 6062-6096.
168. Mulder, F. M.; Assfour, B.; Huot, J.; Dingemans, T. J.; Wagemaker, M.; Ramirez-Cuesta, A. J., Hydrogen in the Metal–Organic Framework Cr MIL-53. *The Journal of Physical Chemistry C* **2010**, *114* (23), 10648-10655.
169. Cockayne, E., Thermodynamics of the Flexible Metal–Organic Framework Material MIL-53(Cr) From First-Principles. *The Journal of Physical Chemistry C* **2017**, *121* (8), 4312-4317.
170. Zhang, Y.; Gao, Q.; Lin, Z.; Zhang, T.; Xu, J.; Tan, Y.; Tian, W.; Jiang, L., Constructing Free Standing Metal Organic Framework MIL-53 Membrane Based on Anodized Aluminum Oxide Precursor. **2014**, *4*, 4947.
171. Chizallet, C.; Lazare, S.; Bazer-Bachi, D.; Bonnier, F.; Lecocq, V.; Soyer, E.; Quoineaud, A.-A.; Bats, N., Catalysis of Transesterification by a Nonfunctionalized Metal–Organic Framework: Acido-Basicity at the External Surface of ZIF-8 Probed by FTIR and ab Initio Calculations. *Journal of the American Chemical Society* **2010**, *132* (35), 12365-12377.
172. Volponi, A.; Filho, S. G. D. S. In *Carbon dioxide sensing at near infrared using zeolitic imidazolate framework-8 (ZIF-8) absorbers*, 2015 30th Symposium on Microelectronics Technology and Devices (SBMicro), 31 Aug.-4 Sept. 2015; 2015; pp 1-4.
173. Brinzer, T.; Daly, C. A.; Allison, C.; Garrett-Roe, S.; Corcelli, S. A., Modeling Carbon Dioxide Vibrational Frequencies in Ionic Liquids: III. Dynamics and Spectroscopy. *The Journal of Physical Chemistry B* **2018**, *122* (38), 8931-8942.

174. Pyles, C. G.; Gretz, G. M.; Spector, I. C.; Massari, A. M., Ultrafast Dynamics Experienced by Carbon Dioxide Diffusing through Polymer Matrices. *The Journal of Physical Chemistry B* **2021**.
175. Mohlenhoff, B.; Romeo, M.; Diem, M.; Wood, B. R., Mie-Type Scattering and Non-Beer-Lambert Absorption Behavior of Human Cells in Infrared Microspectroscopy. *Biophysical Journal* **2005**, *88* (5), 3635-3640.
176. Taheri, A.; Babakhani, E. G.; Towfighi, J., Study of synthesis parameters of MIL-53(Al) using experimental design methodology for CO₂/CH₄ separation. *Adsorption Science & Technology* **2017**, *36* (1-2), 247-269.
177. Embrechts, H.; Kriesten, M.; Ermer, M.; Peukert, W.; Hartmann, M.; Distaso, M., Role of Prenucleation Building Units in Determining Metal–Organic Framework MIL-53(Al) Morphology. *Crystal Growth & Design* **2020**, *20* (6), 3641-3649.
178. Han, C.; Zhang, C.; Tyminska, N.; Schmidt, J. R.; Sholl, D. S., Insights into the Stability of Zeolitic Imidazolate Frameworks in Humid Acidic Environments from First-Principles Calculations. *The Journal of Physical Chemistry C* **2018**, *122* (8), 4339-4348.
179. Zhang, C.; Lively, R. P.; Zhang, K.; Johnson, J. R.; Karvan, O.; Koros, W. J., Unexpected Molecular Sieving Properties of Zeolitic Imidazolate Framework-8. *The Journal of Physical Chemistry Letters* **2012**, *3* (16), 2130-2134.
180. Dombrovsky, L.; Lallich, S.; Enguehard, F.; Baillis, D., An effect of “scattering by absorption” observed in near-infrared properties of nanoporous silica. *Journal of Applied Physics* **2010**, *107* (8), 083106.
181. Spector, I. C.; Olson, C. M.; Huber, C. J.; Massari, A. M., Simple fully reflective method of scatter reduction in 2D-IR spectroscopy. *Opt. Lett.* **2015**, *40* (8), 1850-1852.
182. Seol, J. G.; Kwon, H.; Jin, G. Y.; Moon, J.; Yi, C.; Kim, Y. S., Scattering Elimination of Heterodyne-Detected Two-Dimensional Infrared Spectra Using Choppers and Shutters. *The Journal of Physical Chemistry A* **2019**, *123* (50), 10837-10843.
183. Shim, S.-H.; Zanni, M. T., How to turn your pump-probe instrument into a multidimensional spectrometer: 2D IR and Vis spectroscopies via pulse shaping. *Physical Chemistry Chemical Physics* **2009**, *11* (5), 748-761.
184. Weiner, A. M., Ultrafast optical pulse shaping: A tutorial review. *Optics Communications* **2011**, *284* (15), 3669-3692.
185. Kramer, P. L.; Giammanco, C. H.; Tamimi, A.; Hoffman, D. J.; Sokolowsky, K. P.; Fayer, M. D., Quasi-rotating frame: accurate line shape determination with increased efficiency in noncollinear 2D optical spectroscopy. *J. Opt. Soc. Am. B* **2016**, *33* (6), 1143-1156.
186. Bloem, R.; Garrett-Roe, S.; Strzalka, H.; Hamm, P.; Donaldson, P., Enhancing signal detection and completely eliminating scattering using quasi-phase-cycling in 2D IR experiments. *Opt. Express* **2010**, *18* (26), 27067-27078.
187. Nishida, J.; Tamimi, A.; Fei, H.; Pullen, S.; Ott, S.; Cohen, S. M.; Fayer, M. D., Structural dynamics inside a functionalized metal–organic framework probed by ultrafast 2D IR spectroscopy. *Proceedings of the National Academy of Sciences* **2014**, *111* (52), 18442.

188. Nishida, J.; Fayer, M. D., Guest Hydrogen Bond Dynamics and Interactions in the Metal–Organic Framework MIL-53(Al) Measured with Ultrafast Infrared Spectroscopy. *The Journal of Physical Chemistry C* **2017**, *121* (21), 11880-11890.
189. Hack, J. H.; Dombrowski, J. P.; Ma, X.; Chen, Y.; Lewis, N. H. C.; Carpenter, W. B.; Li, C.; Voth, G. A.; Kung, H. H.; Tokmakoff, A., Structural Characterization of Protonated Water Clusters Confined in HZSM-5 Zeolites. *Journal of the American Chemical Society* **2021**, *143* (27), 10203-10213.
190. Yue, Y.; Mehio, N.; Binder, A. J.; Dai, S., Synthesis of metal-organic framework particles and thin films via nanoscopic metal oxide precursors. *CrystEngComm* **2015**, *17* (8), 1728-1735.
191. Barbara, P. F.; Meyer, T. J.; Ratner, M. A., Contemporary issues in electron transfer research. *J. Phys. Chem.* **1996**, *100* (31), 13148-13168.
192. Kwon, O. H.; Yoo, T. H.; Othona, C. M.; Van Deventer, J. A.; Tirrell, D. A.; Zewail, A. H., Hydration dynamics at fluorinated protein surfaces. *Proc. Natl. Acad. Sci. U.S.A.* **2010**, *107* (40), 17101-17106.
193. Stratt, R. M.; Maroncelli, M., Nonreactive dynamics in solution: The emerging molecular view of solvation dynamics and vibrational relaxation. *J. Phys. Chem.* **1996**, *100* (31), 12981-12996.
194. Tuckerman, M. E.; Marx, D.; Parrinello, M., The nature and transport mechanism of hydrated hydroxide ions in aqueous solution. *Nature* **2002**, *417* (6892), 925-929.
195. Casey, C. P.; Beetner, S. E.; Johnson, J. B., Spectroscopic determination of hydrogenation rates and intermediates during carbonyl hydrogenation catalyzed by Shvo's hydroxycyclopentadienyl diruthenium hydride agrees with kinetic modeling based on independently measured rates of elementary reactions. *J. Am. Chem. Soc.* **2008**, *130* (7), 2285-2295.
196. Chock, P. B.; Halpern, J., Kinetics of the Addition of Hydrogen, Oxygen, and Methyl Iodide to Some Square-Planar Iridium (I) Complexes. *J. Am. Chem. Soc.* **1966**, *88* (15), 3511-3514.
197. Ugo, R.; Pasini, A.; Fusi, A.; Cenini, S., Kinetic investigation of some electronic and steric factors in oxidative addition reactions to Vaska's compound. *J. Am. Chem. Soc.* **1972**, *94* (21), 7364-7370.
198. Cainelli, G.; Galletti, P.; Giacomini, D., Solvent effects on stereoselectivity: more than just an environment. *Chem. Soc. Rev.* **2009**, *38* (4), 990-1001.
199. Gao, J. L., Hybrid quantum and molecular mechanical simulations: An alternative avenue to solvent effects in organic chemistry. *Acc. Chem. Res.* **1996**, *29* (6), 298-305.
200. Farina, V.; Krishnan, B.; Marshall, D. R.; Roth, G. P., PALLADIUM-CATALYZED COUPLING OF ARYLSTANNANES WITH ORGANIC SULFONATES - A COMPREHENSIVE STUDY. *J. Org. Chem.* **1993**, *58* (20), 5434-5444.
201. Fitzpatrick, P. A.; Klivanov, A. M., HOW CAN THE SOLVENT AFFECT ENZYME ENANTIOSELECTIVITY. *J. Am. Chem. Soc.* **1991**, *113* (8), 3166-3171.
202. Riva, R.; Schmeits, S.; Jerome, C.; Jerome, R.; Lecomte, P., Combination of ring-opening polymerization and "click chemistry": Toward functionalization and grafting of poly(epsilon-caprolactone). *Macromolecules* **2007**, *40* (4), 796-803.

203. Schutt, T. C.; Bharadwaj, V. S.; Hegde, G. A.; Johns, A. J.; Maupin, C. M., In silico insights into the solvation characteristics of the ionic liquid 1-methyltriethoxy-3-ethylimidazolium acetate for cellulosic biomass. *Phys. Chem. Chem. Phys.* **2016**, *18* (34), 23715-23726.
204. Brunori, M.; Cutruzzola, F.; Savino, C.; Travaglini-Allocatelli, C.; Vallone, B.; Gibson, Q. H., Does picosecond protein dynamics have survival value? *Trends in Biochemical Sciences* **1999**, *24* (7), 253-255.
205. Jackson, T. A.; Lim, M.; Anfirud, P. A., COMPLEX NONEXPONENTIAL RELAXATION IN MYOGLOBIN AFTER PHOTODISSOCIATION OF MBCO - MEASUREMENT AND ANALYSIS FROM 2-PS TO 56-MU-S. *Chem. Phys.* **1994**, *180* (2-3), 131-140.
206. Merchant, K. A.; Noid, W. G.; Akiyama, R.; Finkelstein, I. J.; Goun, A.; McClain, B. L.; Loring, R. F.; Fayer, M. D., Myoglobin-CO substate structures and dynamics: Multidimensional vibrational echoes and molecular dynamics simulations. *J. Am. Chem. Soc.* **2003**, *125* (45), 13804-13818.
207. Ostermann, A.; Waschipky, R.; Parak, F. G.; Nienhaus, G. U., Ligand binding and conformational motions in myoglobin. *Nature* **2000**, *404* (6774), 205-208.
208. Pu, J. Z.; Gao, J. L.; Truhlar, D. G., Multidimensional tunneling, recrossing, and the transmission coefficient for enzymatic reactions. *Chem. Rev.* **2006**, *106* (8), 3140-3169.
209. Karplus, M., Aspects of protein reaction dynamics: Deviations from simple behavior. *J. Phys. Chem. B* **2000**, *104* (1), 11-27.
210. Jones, B. H.; Huber, C. J.; Spector, I. C.; Tabet, A. M.; Butler, R. L.; Hang, Y.; Massari, A. M., Correlating solvent dynamics and chemical reaction rates using binary solvent mixtures and two-dimensional infrared spectroscopy. *J. Chem. Phys.* **2015**, *142* (21), 212441.
211. Kiefer, L. M.; Kubarych, K. J., Solvent-Dependent Dynamics of a Series of Rhenium Photoactivated Catalysts Measured with Ultrafast 2DIR. *J. Phys. Chem. A* **2015**, *119* (6), 959-965.
212. Ciriminna, R.; Pandarus, V.; Delisi, R.; Scurria, A.; Casaletto, M. P.; Giordano, F.; Béland, F.; Pagliaro, M., Sol-gel encapsulation of Au nanoparticles in hybrid silica improves gold oxidation catalysis. *Chemistry Central Journal* **2016**, *10* (1), 61.
213. Smith, K.; Silvernail, N. J.; Rodgers, K. R.; Elgren, T. E.; Castro, M.; Parker, R. M., Sol-Gel Encapsulated Horseradish Peroxidase: A Catalytic Material for Peroxidation. *Journal of the American Chemical Society* **2002**, *124* (16), 4247-4252.
214. Zhang, Z.; Xiao, Q.; Gu, J., Effective synthesis of zeolite-encapsulated Ni nanoparticles with excellent catalytic performance for hydrogenation of CO₂ to CH₄. *Dalton Transactions* **2020**, *49* (42), 14771-14775.
215. Cho, H. J.; Kim, D.; Xu, B., Pore Size Engineering Enabled Selectivity Control in Tandem Catalytic Upgrading of Cyclopentanone on Zeolite-Encapsulated Pt Nanoparticles. *ACS Catalysis* **2020**, *10* (15), 8850-8859.

216. Cho, H. J.; Kim, D.; Li, J.; Su, D.; Xu, B., Zeolite-Encapsulated Pt Nanoparticles for Tandem Catalysis. *Journal of the American Chemical Society* **2018**, *140* (41), 13514-13520.
217. Blum, J.; Avnir, D., *Handbook of Sol-Gel Science and Technology. Processing Characterization and Application. Volume III: Applications of Sol-Gel Technology*. Kluwer Academic Publishers: Norwell, 2005; p 507-550.
218. Eliaou, N.; Avnir, D.; Eisen, M. S.; Blum, J., Activation of metal-carbonyl clusters by their encapsulation within alumina sol-gel matrices. *J. Sol-Gel Sci. Techn.* **2005**, *35*, 159-167.
219. Marr, A. C.; Marr, P. C., Entrapping homogeneous catalysts by sol-gel methods: The bottom-up synthesis of catalysts that recycle and cascade. *Dalton Trans.* **2011**, *40*, 20-26.
220. Crabtree, R. H., *The Organometallic Chemistry of the Transition Metals*. 5 ed.; John Wiley & Sons: 2009.
221. Lau, C. P.; Ng, S. M.; Jia, G.; Lin, Z., Some ruthenium hydride, dihydrogen, and dihydrogen-bonded complexes in catalytic reactions. *Coord. Chem. Rev.* **2007**, *251*, 2223-2237.
222. Nagashima, H., Facile hydrogenation of acenaphthylenes and azulenes on the face of a triruthenium carbonyl moiety: Discovery of specific reactions on the cluster framework providing unique insight for cluster catalysis. *Monatsh. Chem.* **2000**, *131*, 1225-1239.
223. Patrow, J. G.; Cheng, Y. K.; Pyles, C. G.; Luo, B.; Tonks, I. A.; Massari, A. M., Spectroscopic Study of Sol-Gel Entrapped Triruthenium Dodecacarbonyl Catalyst Reveals Hydride Formation. *J. Phys. Chem. Lett.* **2020**, *11* (17), 7394-7399.
224. Dong, X.; Yang, F.; Zhao, J.; Wang, J., Efficient Intramolecular Vibrational Excitonic Energy Transfer in Ru₃(CO)₁₂ Cluster Revealed by Two-Dimensional Infrared Spectroscopy. *The Journal of Physical Chemistry B* **2018**, *122* (3), 1296-1305.
225. Battiston, G. A.; Bor, G.; Dietler, U. K.; Kettle, S. F. A.; Rossetti, R.; Sbrignadello, G.; Stanghellini, P. L., Comparative infrared and Raman spectroscopic .nu.(carbon monoxide) study of dodecacarbonyltriruthenium, dodecacarbonyltriosmium, their mixed crystals, and the mixed triangulo cluster carbonyls dodecacarbonylsmiumdiruthenium and dodecacarbonyldiosmiumruthenium. *Inorganic Chemistry* **1980**, *19* (7), 1961-1973.
226. Battiston, G. A.; Sbrignadello, G.; Bor, G., Infrared spectroscopic studies on metal carbonyl compounds. 23. A simple quantitative treatment of the infrared band intensity and the induced metal-metal dipole contribution to it in polynuclear metal carbonyls. An application to the spectrum of dodecacarbonyltriruthenium and dodecacarbonyltriosmium in the carbon-oxygen stretching region. *Inorganic Chemistry* **1980**, *19* (7), 1973-1977.
227. Patrow, J. G.; Cheng, Y.; Pyles, C. G.; Luo, B.; Tonks, I. A.; Massari, A. M., Spectroscopic Study of Sol-Gel Entrapped Triruthenium Dodecacarbonyl Catalyst Reveals Hydride Formation. *The Journal of Physical Chemistry Letters* **2020**, *11* (17), 7394-7399.

228. Eliau, N.; Avnir, D.; Eisen, M. S.; Blum, J., Activation of Metal-Carbonyl Clusters by their Encapsulation Within Alumina Sol-Gel Matrices. *Journal of Sol-Gel Science and Technology* **2005**, *35* (2), 159-167.
229. Yamada, S. A.; Shin, J. Y.; Thompson, W. H.; Fayer, M. D., Water Dynamics in Nanoporous Silica: Ultrafast Vibrational Spectroscopy and Molecular Dynamics Simulations. *The Journal of Physical Chemistry C* **2019**, *123* (9), 5790-5803.
230. Oréface, R. L.; Vasconcelos, W. L., Sol-Gel transition and structural evolution on multicomponent gels derived from the alumina-silica system. *Journal of Sol-Gel Science and Technology* **1997**, *9* (3), 239.